

Dissertation

submitted to the

Combined Faculties of the Natural Sciences and Mathematics
of the Ruperto-Carola-University of Heidelberg, Germany

for the degree of

Doctor of Natural Sciences

Put forward by

Master.-Natur-Sci. Yinpeng Zhong

born in: YongChang/GanSu/China

Oral examination: 2012/12/20

Ultrafast Dynamics in Polar and Magnetic Semiconductors:
Optical and Free-Electron Laser Investigations

Referees: Prof. Dr. Ilme Schlichting
Priv.-Doz. Dr. Robert Moshhammer

Abstract

Die vorliegende Arbeit befasst sich mit ultraschnellen Prozessen in polaren und in ferromagnetischen Halbleitern. Die Experimente wurden sowohl bei optischen Wellenlängen eines Titanium Saphir Lasers als auch mit Röntgenstrahlung des Freie-Elektronen Lasers "Linac Coherent Light Source" (LCLS) durchgeführt. Bei dem polaren Halbleiter Cadmiumtellurid, dotiert mit Lithium, zeigte die zeitaufgelöste Pump-Probe Messung der Reflektivität eine Wechselwirkung zwischen Ladungsträgern und Kristallgitter des Halbleiters: sowohl Coulomb-Abschirmung als auch Phonon-Plasmon Kopplung wurde festgestellt. Bei Dotierung mit magnetischen Elementen treten zusätzlich magnetische Wechselwirkungen auf. Beispielhaft wurde der ferromagnetische Halbleiter $\text{Ga}_{1-x}\text{Mn}_x\text{As}$, Mangan dotiertes Galliumarsenid, mit zeitaufgelöster Röntgendiffraktion an LCLS untersucht. Eine Korrelation zwischen laser-angeregten Ladungsträgern, akustischen Phononen und der Spinordnung wurde beobachtet. Darüber hinaus konnte eine Veränderung des quasi Fermi-Levels der Elektronenlöcher in Abhängigkeit von Zeit und Temperatur durch resonante Röntgenemissionsspektroskopie gezeigt werden.

The ultrafast carrier and lattice dynamics in polar and ferromagnetic semiconductors were investigated using optical and X-ray free-electron laser. In polar semiconductor Li-doped CdTe, the influence of Coulomb screening and phonon-plasmon coupling in carrier and lattice dynamics was observed by means of a time resolved pump-probe reflectivity technique. When doping polar semiconductors with magnetic atoms, magnetic interactions are introduced, e.g., in ferromagnetic semiconductor $\text{Ga}_{1-x}\text{Mn}_x\text{As}$, the Mn doped GaAs. By applying the novel X-ray free-electron laser radiation, delivered by the Linac Coherent Light Source (LCLS), the time resolved X-ray diffraction was measured, which directly reveals the interplay between the laser excited carriers, acoustic phonon modes and spin order. Simultaneously, the evolution of hole quasi Fermi-level as a function of time and temperature was measured by the resonant X-ray emission spectroscopy.

Contents

List of Figures	ix
List of Tables	xiii
1 Introduction	1
2 Theoretical Background: Ultrafast Dynamics of Solids under Intense Laser Excitation	5
2.1 Introduction	5
2.2 Photonexcitation, Relaxation, Recombination and Diffusion	11
2.3 Modeling Carrier and Lattice Dynamics	26
3 Ultrafast Dynamics in Highly Excited CdTe: The Time-Resolved Reflectivity Measurement	35
3.1 Introduction	35
3.2 Optical Pump-Probe Experimental Setup	37
3.3 Calculating the Optical Properties of the Laser-Excited CdTe	39
3.3.1 Optical Properties of a Hot Electron-Hole Plasma	39
3.4 Time-Resolved Reflectivity Measurement and Discussion	47
3.4.1 Longitudinal-Optical Phonon-Plasmon Coupled Modes	47
3.4.2 CdTe under High Laser Excitation	51
3.5 Conclusion	60
4 Ultrafast Dynamics in Laser-Excited Diluted Magnetic Semiconductors	61
4.1 Introudction	61
4.2 The Free Electron Laser	62
4.3 General Considerations: Mechanisms, Dynamics and Probe	64

CONTENTS

4.3.1	Ferromagnetism in DMSs	64
4.3.2	Probe Lattice Dynamics: X-ray diffraction	66
4.3.2.1	Lattice Dynamics: Strain Generation	66
4.3.2.2	Takagi-Taupin equations	67
4.3.3	Probe Hole's Nonequilibrium Distribution: Resonant X-ray Emission	69
4.4	The X-ray Diffraction and Emission Spectroscopy Experimental Setup	72
4.5	Results of Time Resolved X-ray Diffraction	78
4.6	Results of Time-Resolved Resonant X-ray Emission Measurements	87
4.7	Summary	89
5	Summary and Outlook	91
	Appendix	95
	References	103

List of Figures

2.1	Band structure and the density-of-states ($g_{DOS}(E)$) of CdTe.	8
2.2	Phonon dispersion relation for CdTe at 300 K.	10
2.3	Dependence of the reflectivity on the angle of incidence for CdTe.	12
2.4	Interband transitions in a semiconductor with a direct band gap.	14
2.5	Schematic illustration of the multi-photon absorption process.	15
2.6	Intraband absorption and phonon-emission in the conduction band.	16
2.7	Schematic illustration of the photonexcitation of electron and holes and their redistributions.	17
2.8	Schematic illustration of the intravalley scattering processes.	18
2.9	A comparison of acoustic scattering, polar optical scattering and intervalley scattering in CdTe at room temperature.	20
2.10	Schematic illustration of the intervalley scattering process.	22
2.11	Illustrate the Radiative and Auger recombination.	24
2.12	Radiative recombination in GaAs.	25
2.13	Auger recombination in GaAs.	25
2.14	Carrier diffusion.	25
2.15	The Stanton-Bailey four-state model.	27
2.16	A simulation based on the Stanton-Bailey model.	28
2.17	Band diagram of a p-doped semiconductor.	30
2.18	The optical phonon generation mechanism in a polar semiconductor.	30
2.19	Phonon-plasmon coupled-modes in CdTe.	32
2.20	Time evolutions of the electric field in the space charge region in CdTe.	33
3.1	Lattice structure of cadmium telluride (CdTe).	36
3.2	Band structure of CdTe.	36
3.3	Optical pump-probe setup	38
3.4	The operation principle of the Lock-in amplifier with a optical chopper	38

LIST OF FIGURES

3.5	The enhancement of P-polarized light probing near the Brewster's angle θ_{br}	39
3.6	Scheme of the applied theoretical approach.	40
3.7	The quasi-Fermi level of CdTe in the Γ valley.	41
3.8	Band-gap renormalization in CdTe (Γ valley).	43
3.9	The dielectric function of CdTe.	46
3.10	The comparison between the simulation and the parameterized function.	46
3.11	A typical low pump fluence PPR curve.	48
3.12	The comparison of the coherent oscillations at fluence $0.064 \text{ mJ}\cdot\text{cm}^{-2}$ and at $0.57 \text{ mJ}\cdot\text{cm}^{-2}$. In order to avoid the coherent artifact [1] near to time zero, oscillations are extracted after that.	49
3.13	The wavelet transforms of the oscillations measured at the pump fluences of 0.064 and $0.57 \text{ mJ}\cdot\text{cm}^{-2}$	49
3.14	Compariation of experiment and theory in terms of wavelet transform spectra.	50
3.15	Comparison of carrier density distribution at low and high fluence.	51
3.16	The time-resolved reflectivity measurement of the lithium-doped CdTe.	52
3.17	Interplay between BF and BGR affecting the probe beam reflectivity.	53
3.18	The excitation and carrier dynamics in CdTe.	54
3.19	The effective cooling time and recombination coefficient versus fluence.	58
3.20	Comparison of the high fluence measurements with the simulations.	58
3.21	Comparison of the experimentally measured data and simulations.	59
3.22	The effective TPA coefficient.	59
4.1	The operation principle of an FEL.	63
4.2	The strain generation mechanism.	67
4.3	Comparison of the standard Thomsen model with the modified one.	68
4.4	The rocking curve and the phonon dispersion relation.	70
4.5	The FEL resonant X-ray emission probe principle.	71
4.6	The experimental geometry	73
4.7	Explosion view of the set up.	74
4.8	View of the auxiliary chamber.	75
4.9	Cut-view of the beryllium window flange.	76
4.10	Isometric view of the pnCCD assembly.	76
4.11	Calibriation of pnCCDs.	77
4.12	The sample cooling system.	77
4.13	The $\Delta\theta$ defined from the unperturbed rocking curve.	78

LIST OF FIGURES

4.14	The XRD intensity modified by the acoustic-phonons at the pump fluence $4 \text{ mJ}\cdot\text{cm}^{-2}$	79
4.15	The XRD intensity modified by the acoustic-phonons at the pump fluence $6.5 \text{ mJ}\cdot\text{cm}^{-2}$	80
4.16	The measured phonon-dispersion relation.	80
4.17	The rocking curve at room temperature.	82
4.18	The simulations of the XRDs at fluence of $4 \text{ mJ}\cdot\text{cm}^{-2}$ and $6.5 \text{ mJ}\cdot\text{cm}^{-2}$	83
4.19	Comparison of the XRDs measured at 300 K and 140 K.	85
4.20	The magnetization-temperature curve of $\text{Ga}_{0.91}\text{Mn}_{0.09}\text{As}$ and its derivation.	85
4.21	XRDs measured at two fluences of $4 \text{ mJ}\cdot\text{cm}^{-2}$ and $6.5 \text{ mJ}\cdot\text{cm}^{-2}$	86
4.22	The measured Ga K-edge fluorescence spectrum.	87
4.23	Integrated RXE intensity from $\text{Ga}_{1-x}\text{Mn}_x\text{As}$ (unperturbed) at different temperatures.	88
4.24	Schematic illustration of the Mn impurity band and the host GaAs valence band.	89
4.25	Time dependent resonant X-ray emission intensity at various temperatures.	90
1	X-ray absorption mechanism.	95
2	X-ray fluorescence generation.	96
3	X-ray Auger decay.	96
4	Principle of the inelastic scattering (Compton scattering).	97
5	Diffraction: Bragg and Laue.	98

LIST OF FIGURES

List of Tables

3.1	Model parameters	45
3.2	Simulation parameters	51
3.3	Model parameters	57
4.1	LCLS FEL parameters	64
4.2	Simulation parameters	82

LIST OF TABLES

Chapter 1

Introduction

Integrated circuits (ICs) used for data processing operate by controlling the flow of carriers through semiconductors [2]. The key parameter here is the charge: electrons in the conduction band and holes in the valence band. However, phonons (lattice vibrations) play also a very important role, since their interaction with the charge carriers strongly influences the charge mobility, which provides a measure of how fast a semiconductor device will operate and what the power requirements are.

The characteristics of the semiconductor devices (e.g. ICs) include high speed signal processing and excellent reliability, but the memory elements are volatile (the stored information is lost when the power is switched-off, as data is stored as charge in capacitors) [2]. A key advantage of magnetic recording using the spin of electrons in ferromagnetic materials is its non-volatile memory since these materials by nature have remanence [2, 3]. It is quite natural to ask whether one can manipulate both charge and spins to further enhance the performance of devices. One then is able to use the capability of mass storage and processing information at the same time. Such materials which combine semiconductor transport and magnetic properties are the so-called Diluted Magnetic Semiconductors (DMSs) where cations are substituted by randomly distributed magnetic atoms. Although the Curie temperature in technologically important DMSs (e.g. $\text{Ga}_{1-x}\text{Mn}_x\text{As}$) is below room temperature, $T_C \sim 190$ K [4], they are still under active investigation as unique model materials to integrate the magnetic and charge degrees of freedom onto a single chip [5, 6, 7]. The development of small-scale and high speed semiconductor-based devices requires a clear understanding of the various dynamical properties of carriers as well as phonons on ultrashort time scale. The processes that govern such dynamics are best investigated by first generating these quasi-particles in a nonequilibrium state with a short light pulse, and then observing

1. INTRODUCTION

their subsequent relaxation. When a semiconductor crystal is excited with photons of an energy larger than the band gap, electrons and holes with finite excess energy are created within the optical absorption depth which typically ranges between 0.1 to 1 μm . These photoexcited carriers (i.e. electrons and holes) lose their excess energy and relax to the band minimum by interacting among themselves, with the atoms composing the crystal and with spins of magnetic atoms.

In this thesis, the ultrafast carrier and lattice dynamics in polar and magnetic semiconductors is investigated using optical and free-electron lasers. In Chapter 3, the ultrafast dynamics of cadmium telluride (CdTe) was investigated by means of the time resolved optical reflectivity technique. CdTe is a polar semiconductor with a wide range of applications such as optoelectronics, solar cells, infrared, X-ray and γ -ray detectors [8, 9, 10]. In particular, due to the high atomic weight of Cd and Te atoms, CdTe is an optimal material for fabricating solar cells for space applications, especially at high altitudes where cosmic radiation readily degrades the existing silicon cells. Coulomb coupling between the ionic-atoms and electrons will influence strongly the dynamics of both, carriers and the lattice: the phonon and plasmon character will be mixed and new coupled phonon-plasmon modes will be formed. One objective on this part of this thesis is to study the effect of these hybrid phonon-plasmon modes on the carrier cooling and relaxation. Although CdTe is an important material with a wide range of applications, the experimental work on the ultrafast dynamics is rare [11, 12, 13], especially, if one compares it with the very well studied polar semiconductor GaAs [14, 15, 16, 17, 18, 19, 20]. So far, the only well know papers on the ultrafast dynamics of CdTe are those of Ishioka et al. [12] and Leitenstorfer et al. [13]. Ishioka et al., reported the time-resolved reectivity on bulk CdTe. The authors measured coherent longitudinal optical phonons, however due to the low excitation fluence used, they couldn't observe clearly the coupled phonon-plasmon dynamics. Leitenstorfer et al., on the other hand, observed faster relaxation of hot carrier due to the stronger electron-phonon coupling compared to the weakly coupled GaAs. These investigations, however, were also limited to low carrier densities (below $10^{17} \cdot \text{cm}^{-3}$). In this work, the coupling of carriers and the lattice was investigated for excitation fluences spanning about three orders of magnitude (or, in terms of the photoexcited carrier density, they cover the range from 10^{17} to $10^{19} \cdot \text{cm}^{-3}$), covering a range from weak to strong Coulomb screening.

In Chapter 4 of the thesis, the interplay between carriers, spins and the lattice in the ferromagnetic $\text{Ga}_{1-x}\text{Mn}_x\text{As}$ semiconductor was investigated using the X-ray free-electron laser at the Linac Coherent Light Source (LCLS). By referencing the LCLS

probe beam to the Ga K-edge it was possible to employ simultaneously the time resolved X-ray diffraction and fluorescence spectroscopy in laser excited manganese-doped gallium arsenide ($\text{Ga}_{1-x}\text{Mn}_x\text{As}$). This material took centre stage in 1996, when H. Ohno's group demonstrated ferromagnetic order in this compound with a T_C of 110 K [21, 22]. With improvements of the material's quality, the temperature has subsequently risen to 190 K [4]. Soon afterwards, room temperature T_C was predicted by T. Dietl [3], which attracted widespread attentions. In $\text{Ga}_{1-x}\text{Mn}_x\text{As}$, the ferromagnetic properties originate from a mutual polarization of isolated Mn spins by the holes and vice versa. Based on this, it is not surprising that exploring hole's dynamics was the goal of ultrafast investigations [23, 24, 25, 26]. Apart from holes, the interplay between coherent phonons and spins were shown to have a fundamental role on the modification of the ferromagnetic properties, e.g., phonon driven spin waves [27]. The objective on this part of the thesis was to investigate the effects of the ferromagnetic exchange interaction on the lattice heating time and coherent motion of atoms as a function of temperature. In $\text{Ga}_{1-x}\text{Mn}_x\text{As}$, the p-d hybridization between the orbitals of the magnetic atoms (Mn) and those of the host (GaAs) affects the energy bands and, since the carrier excess energy and relaxation depend strongly on the details of the band structure, it will profoundly influence the generation and evolution of the coherent motion of the lattice. Time-domain information about magnetic properties of DMSs have, typically, employed time-resolved magneto-optical spectroscopy. This method has provided essential contributions to understanding of exchange interactions, spin relaxation, spin coherent effects and dephasing phenomena [23, 24, 25, 26, 28, 29]. X-ray diffraction, on the other hand, can directly observe the small shifts in interatomic distance associated with coherent phonons [30, 31, 32, 33, 34, 35, 36]. Complemented with the resonant X-ray emission spectroscopy which is capable of probing the dynamics of holes in the valence band, it provides vital information about the correlation of lattice, spins and charge.

The thesis is structured as follows:

Chapter 2 provides an overview of the carrier and structural dynamics in semiconductors following the excitation with a short laser pulse; it introduces the concepts, processes and the quantities which characterize ultrafast dynamics in semiconductors.

Chapter 3 presents the pump-probe time resolved reflectivity measurements in a doped CdTe crystal at various fluences, covering a range from weak to strong Coulomb screening. It will be shown that the phonon-plasmon coupling has great influence on the carrier cooling time.

Chapter 4 investigates the time resolved X-ray diffraction and resonant X-ray emis-

1. INTRODUCTION

sion from the laser excited $\text{Ga}_{1-x}\text{Mn}_x\text{As}$. It presents the influence of ferromagnetic exchange and carrier-lattice coupling on the coherent acoustic phonons. In addition, it also presents the evolution of hole Fermi level as a function of time and temperature measured by resonant X-ray emission.

Chapter 2

Theoretical Background: Ultrafast Dynamics of Solids under Intense Laser Excitation

2.1 Introduction

This chapter presents an overview of the carrier and structural dynamics in semiconductors following the excitation with a short laser pulse; it introduces the concepts, processes and the quantities which characterize ultrafast dynamics in semiconductors. The theoretical foundations presented here are intended to support understanding and interpretation of the experimental results described in the following chapters.

Electronic States

A solid is composed of a large number of atoms $N \sim 10^{22} \text{ atoms} \cdot \text{cm}^{-3}$. If these atoms would be at relatively large distances, each of them would be independent of all the others and would have atomic energy levels as if isolated. However, when the N-atom ensemble condenses into a solid phase, the atoms come into the interaction range of one another and the “isolated-atom” energy levels will change. What was a single level for an isolated atom, in a solid broadens out into N closely spaced levels to form what is called the electron energy band. Mathematically, the electron energy bands are provided by the solution of the Schrödinger equation appropriate for a crystal. The electrons in the outermost shells of the isolated atoms are the ones that interact strongly with the similar electrons in the neighboring atoms; these are called valence electrons. The remaining electrons of the atom are mostly localized around the nuclei (their wave

2. THEORETICAL BACKGROUND: ULTRAFAST DYNAMICS OF SOLIDS UNDER INTENSE LASER EXCITATION

functions do not extend far from the position of the nucleus) and are very little affected by the neighboring atoms; together with nuclei, these electrons constitute the so-called ion core. The way in which the valence electrons interact between each other, with the nuclei of the atoms composing the solid and with external perturbations determining all properties of solids (mechanical, optical, electric and magnetic properties). Valence electrons that move in a crystal feel a background periodic potential U due to ion cores and all other electrons:

$$U(\mathbf{r}) = U(\mathbf{r} + \mathbf{R}) \quad (2.1)$$

where \mathbf{r} is the position vector of an electron inside a crystal and \mathbf{R} is the translational lattice vector which runs over all ion cores. Therefore, the probability of finding electrons in the crystal $|\varphi(\mathbf{r})|^2$ has the same periodicity as the potential $U(\mathbf{r})$, such that, the wave function has to be of special form described by the Bloch theorem:

$$\varphi_k(\mathbf{r}) = e^{i\mathbf{k}\mathbf{r}} u_k(\mathbf{r}) \quad (2.2)$$

where $u_k(\mathbf{r})$ is a wave function (closely related to the free atom wave functions) with the same periodicity as the potential $U(\mathbf{r})$ and k is the electron wave vector which, when multiplied with the reduced Planck constant \hbar , is called the crystal momentum and contains the effect of the periodic potential in the motion of the electron.

The Bloch theorem represents two attributes of the valence electrons: (i) the atomic character described by the wave function $u_k(\mathbf{r})$ and (ii) the free particle character described by the plane wave term $e^{i\mathbf{k}\mathbf{r}}$. The states φ_k are referred to as Bloch states. The allowed values of k are equal to the number of primitive cells in real space; in reciprocal space this number is contained in the so-called first Brillouin zone. For example, cadmium telluride (CdTe) with a mass density of $5.86 \text{ g}\cdot\text{cm}^{-3}$ has $\sim 1.47 \times 10^{22}$ primitive unit cells in one cubic centimeter. In order to discuss the motion of electrons, it is necessary to form a localized wavepacket by linear superposition of Bloch states of various wave vectors so that the electron can be assigned a particular coordinate at a particular time. Hereafter, when discussing carrier dynamics, a carrier is always assigned to a wave vector k which represents the peak of its wavepacket.

The conventional representation of the electron energy bands is shown in figure 2.1. Here, the energy of the electrons in different bands of CdTe is plotted against the electron wave vector k which is restricted in the first Brillouin zone. The number of states in a particular energy band is equal to the number of allowed k values. In the Brillouin zone center where $k=(000)$ is the Γ point. The zone edges along the (100) and (111) directions are called X and L points. The three lowest dispersion

relations represent the valence band which at $T=0$ K is always fully occupied. The uppermost curve, unoccupied at 0 K, represents the conduction band. These two bands are separated by the energy band gap (E_g at the Γ -point) which represents the energy range where no electron state can exist. The energy valleys in the conduction band containing Γ , L and X points are called Γ , L and X-valleys.

Another quantity which plays an important role in describing the dynamics in photonexcited semiconductors is the density-of-states, $g_{DOS}(E)$. This quantity is defined so that the number of states per unit volume in an energy interval between E and $E + \Delta E$ is $g_{DOS}(E)\Delta E$. Mathematically, the density-of-states at a given energy E is given by the following relation.

$$g_{DOS}(E) = \frac{1}{V} \sum_k 2 \times \delta(E - E_k) \quad (2.3)$$

where V is the volume of the crystal. The $g_{DOS}(E)$ for the conduction band and the valence bands of CdTe is shown in the right side of figure 2.1. If several bands overlap, the density-of-states need to be summed up.

Various processes in photonexcited semiconductors such as, for example, carrier scattering rates, relay on the number of occupied electronic states. The probability that a given electronic state is occupied is given by the distribution function $f(E)$. In thermal equilibrium $f(E)$ is given by the Fermi-Dirac distribution function:

$$f(E) = \frac{1}{e^{(E-\mu)/k_B T} + 1} \quad (2.4)$$

where μ is the chemical potential which separates the occupied from unoccupied levels at the absolute temperature $T=0$ K, and k_B is the Boltzmann constant. The product of the density of states (equation 2.3) and the probability distribution function 2.4 is the number of occupied states per unit volume at a given energy for a system in thermal equilibrium. Semiconductors are insulators in the ground state (at 300 K), which means that the conduction band is empty whereas the valence band is completely full. They start conducting when electrons are excited from the valence band to the conduction band. The conductivity is mediated both by the negatively charged electrons excited to the conduction band and by the positive holes left behind in the valence band by the excited electrons. The conducting electrons and holes are often referred to as free carriers, or simply carriers.

2. THEORETICAL BACKGROUND: ULTRAFAST DYNAMICS OF SOLIDS UNDER INTENSE LASER EXCITATION

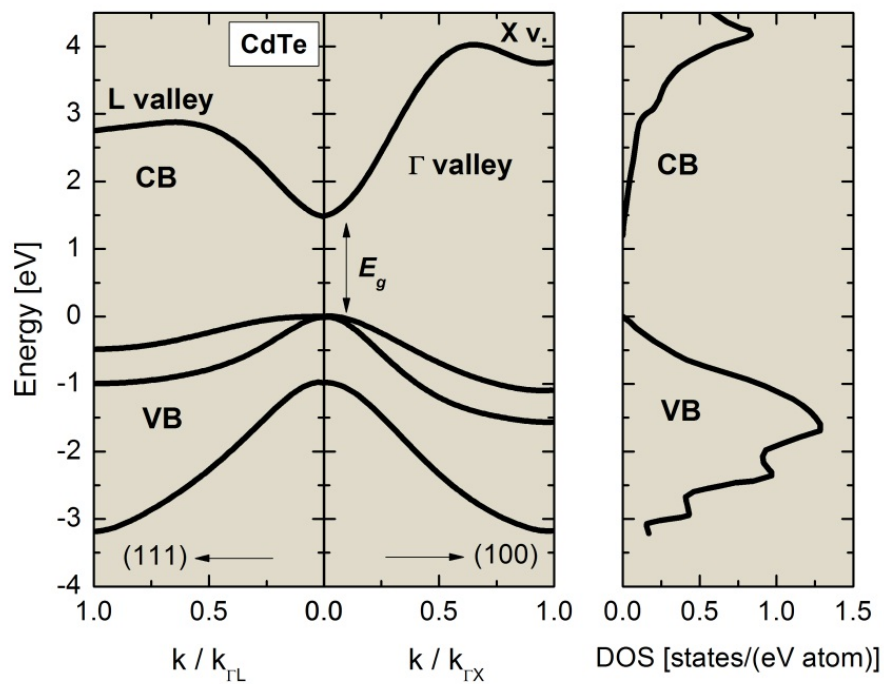


Figure 2.1: Band structure and the density-of-states ($g_{DOS}(E)$) of CdTe. - The dispersion of the bands is shown for two directions of the Brillouin zone: Γ -L and Γ -X. The valence band is composed of three bands characterized by different effective masses: heavy hole (hh), light hole (lh) and split-off hole (soh) bands. The density-of-states is a sum over all partial contributions.

Lattice Vibrations and Electron-Phonon Interaction

As discussed in the previous section, a solid is composed of large number of valence electrons and ionic cores in mutual interactions. Obviously, the many-particle Schrödinger equation describing the state of the system can not be solved without simplifications. To a good approximation, however, one can separate electronic motion from that of the ion-cores. Since the mass of an ion is at least a factor of 1.8×10^3 greater than that of an electron, for comparable energies and perturbations ions therefore move some 100 times slower than electrons, and the latter can be regarded as instantaneously adjusting their motion to that of the ions, or in other words, to the electrons the ions are essentially stationary. Within this approximation, the so called Born-Oppenheimer approximation, the many-particle Hamiltonian can be expressed as a sum of three terms [37, 38]:

$$H(\{r_i\}, \{R_j\}) = H_e(\{r_i\}, \{R_{j,0}\}) + H_{ion}(\{R_j\}) + H_{e-ion}(\{r_i\}, \{\delta R_j\}) \quad (2.5)$$

whereas the wave function is:

$$\Psi(\{r_i\}, \{R_j\}) = \psi(\{r_i\}, \{R_{j,0}\})\varphi(\{R_j\}) \quad (2.6)$$

with the curly brackets $\{r_i\}$ and $\{R_j\}$ represent the sets of electron and ion coordinates, respectively, $\psi(\{r_i\}, \{R_{j,0}\})$ is the wave function of all the electrons and $\varphi(\{R_j\})$ is the wave function of all the ions. The first term in equation 2.5 describes the electron system with the ion cores fixed in a given configuration $\{R_{j,0}\}$. When it operates on ψ it yields the electron energy bands $E_k(\{R_{j,0}\})$ which have been discussed in the previous section.

The second term describes the dynamics of the ion cores. When it operates on the ion wave function $\varphi(\{R_j\})$ it yields the allowed values of the vibration frequency or the so-called phonon dispersion relation. One uses the term phonon to describe the lattice vibrations which can be understood as a quanta of the ionic displacement field (in analogy with photons which are quanta of the radiation field) [39]. The displacement of an ion core from its equilibrium position is:

$$u(R, t) = \phi e^{i(qR - \omega_q t)} \quad (2.7)$$

This equation represents a phonon mode. ϕ is a vector indicating the amplitude and the direction of the phonon mode (frequently called polarization vector of the normal mode), ω_q is an allowed phonon frequency, and q represents the phonon wave vector which, similar as the crystal momentum k , can take N distinct values. If p is the

2. THEORETICAL BACKGROUND: ULTRAFAST DYNAMICS OF SOLIDS UNDER INTENSE LASER EXCITATION

number of ionic cores in the basis (e.g. $p = 2$ for CdTe and GaAs), the dispersion relation $\omega(q)$ has $3 \times p$ phonon branches where 3 of them describe the propagation displacement of the lattice in a speed of sound thus be called acoustic modes and the other $3p - 3$ branches are optic mode due to their often optically active characters (see the figure 2.2).

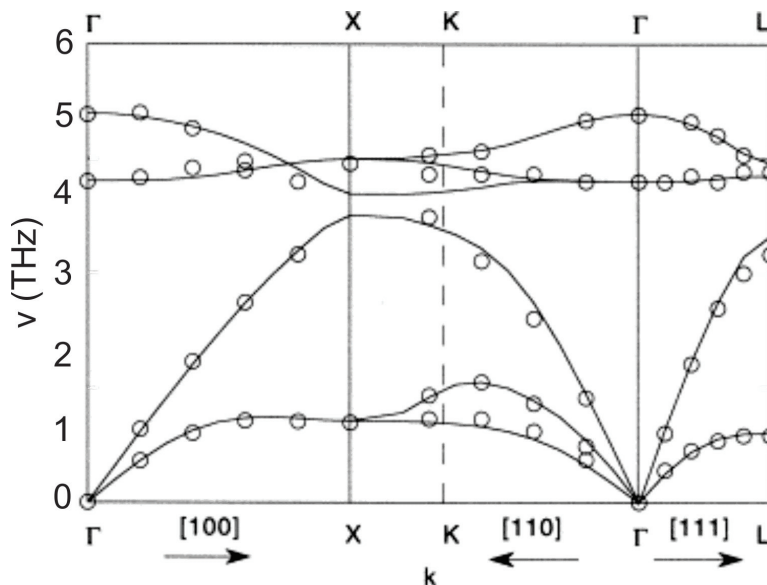


Figure 2.2: Phonon dispersion relation for CdTe at 300 K. - Since CdTe has a two-atom basis, the dispersion relation has six branches: three acoustic branches (one Longitudinal Acoustic abbr. LA and two Transverse Acoustic abbr. TA) and three optical branches (one Longitudinal Optical abbr. LO and two Transverse Optical abbr. TO). Some branches, depending on the direction in the reciprocal space, are degenerate (picture from [38]).

The third term in equation 2.5 describes the interaction between the electrons and the motion of the ionic cores. This term represents the so-called electron-phonon interaction and is responsible to a large extent for the redistribution of carriers in their bands. This term acts on the electrons always when the displacement from the equilibrium position is larger than zero (i.e. $u(R) - u(R_0) > 0$). Within the spirit of the Born-Oppenheimer approximation this term can be expressed as a Taylor series expansion of the electronic Hamiltonian $H_e(r, R_0)$:

$$H_{e-ion}(r_i, u_j) \approx \sum_j \left. \frac{\partial H_e}{\partial R_j} \right|_{R_{j0}} u_j \quad (2.8)$$

Usually the electronic Hamiltonian $H_e(r_i, R_{j,0})$ is not known. Therefore approxi-

mations are needed in order to calculate the electron-phonon interaction [38].

2.2 Photonexcitation, Relaxation, Recombination and Diffusion

The optical properties of semiconductors (and of matter, in general) are associated with absorption, dispersion and scattering. All these processes result from the perturbation of the material by the electromagnetic field. During the excitation process within a light pulses, photons interact mainly with carriers (electrons and holes) and transfer their energy to them since the energy exchange between photons and atoms is dominated mainly by the strong electron-photon interaction due to the fact that electrons are much lighter than the ions. Therefore, optical properties depend mainly on the electronic structure (band structure) of a material.

When a light pulse impinges on a semiconductor crystal, part of it is reflected from the front surface while the rest enters the medium and propagates through it until, depending on the crystal thickness, it gets absorbed. The reflection of the beam at the surface is described by the coefficient of reflection or reflectivity and can be calculated using the Fresnel's formula [40].

$$R_p = \left| \frac{\frac{n_i}{\mu_i} \cos \theta_i - \frac{n_t}{\mu_t} \cos \theta_t}{\frac{n_i}{\mu_i} \cos \theta_i + \frac{n_t}{\mu_t} \cos \theta_t} \right|^2 \quad (2.9)$$

$$R_s = \left| \frac{2 \frac{n_i}{\mu_i} \cos \theta_i}{\frac{n_i}{\mu_i} \cos \theta_i + \frac{n_t}{\mu_t} \cos \theta_t} \right|^2 \quad (2.10)$$

where n , μ are the real part and imaginary part of the refractive index, θ is the angle of incidence relative to the surface and, the subscripts p and s stand for p - and s -polarized light. Figure 2.3 shows the reflectivity curves for crystalline CdTe at $\hbar\omega = 1.55$ eV. The shapes of the curves are common to most materials. While the s -reflectivity monotonically decreases with the angle, the p -reflectivity shows a minimum at the so-called Brewster angle $\theta_{Br} = \frac{\pi}{2} - \tan^{-1}n$. Thus, if one uses p -polarized light to excite a solid at θ_{Br} most of the energy will be absorbed.

The real part of the index n gives the factor by which the phase velocity is reduced in the medium, and the imaginary part μ is proportional to the rate of energy loss (absorption). Absorption of the light occurs basically through two mechanisms: (i) interband absorption where photons excite electrons from a valence band to the

2. THEORETICAL BACKGROUND: ULTRAFAST DYNAMICS OF SOLIDS UNDER INTENSE LASER EXCITATION

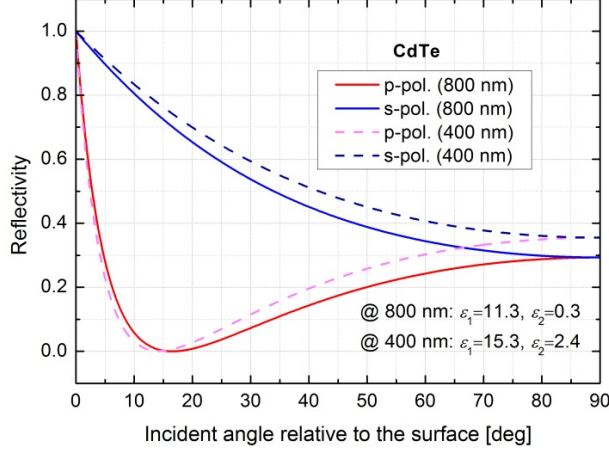


Figure 2.3: Dependence of the reflectivity on the angle of incidence for CdTe.

- The inset lists the real and imaginary parts of the dielectric constant $\varepsilon = \varepsilon_1 + i\varepsilon_2$, which related with the index of refraction $\varepsilon_1^2 = n^2 - \mu^2$ and $\varepsilon_2^2 = 2n\mu$.

conduction band and (ii) intraband absorption where photons excite free carriers to a higher energy state within a band. In both cases, the optical excitation process is governed by the conservation of energy, conservation of the momentum and the Pauli exclusion principle.

i. Interband absorption

This mechanism involves excitation of an electron from the valence band to the conduction band by absorption of N light photons. $N = 1, 2$ and m represent single photon absorption (SPA), two-photon absorption (TPA) and, in general, multi-photon absorption MPA. In all these processes the excitation of the electron to a state in the conduction band with energy E_c leaves the initial state at energy E_v unoccupied. Thus, a hole is created in the initial state. Interband SPA is the most important excitation mechanism in semiconductors when the photon energy is larger than the band gap. Conservation of energy demands that:

$$E_c - E_v = \hbar\omega \quad (2.11)$$

$$K_c - K_v = K_{\text{photon}} \quad (2.12)$$

2.2 Photonexcitation, Relaxation, Recombination and Diffusion

where K_v and K_c are the wave vectors of the electron in the initial and final states, respectively, and K_{photon} is the wave vector of the light photon. At optical wavelengths (from 400 nm to 800 nm) $K_{photon} = 2\pi/\lambda_{photon}$ is on the order of 10^7 m^{-1} . The wave vector of the electron, on the other hand, is related to the size of the Brillouin zone ($\sim \pi/a$, where a is the lattice constant) and can be as large as $\sim 10^{10} \text{ m}^{-1}$. Therefore, since wave vectors of the electrons have much larger magnitudes than that of a photon, K_{photon} in equation 2.12 can be neglected and the conservation of the momentum can be written as:

$$K_c = K_v \quad (2.13)$$

Equation 2.13 implies that optical transitions lead to negligible changes in the wave vector of the electron and, thus, are represented by vertical arrows in the $E - K$ dispersion relation, see figure 2.4. A monochromatic laser pulse excites electron-hole pairs at specific points in the band structure determined by the conservation of energy (equation 2.11) and momentum (equation 2.13). The big difference in the curvatures of the conduction band and valence band (i.e. figure 2.1) implies that most of the excess energies $\Delta E_{e,h}$, reside initially in the electrons rather than in the holes, see the figure 2.3. In the case of parabolic band approximation (i.e. the energy band valleys are approximated by parabolas) one can calculate:

$$\Delta E_e = \frac{\hbar\omega - E_g}{1 + m_e/m_h} \quad (2.14)$$

$$\Delta E_h = -\frac{m_e}{m_h} \Delta E_e \quad (2.15)$$

where m_e and m_h are the effective masses of electrons and holes, respectively. For example, CdTe ($E_g \sim 1.5 \text{ eV}$) near the Γ point has $m_e = 0.08m_0$ and $m_h = 0.84m_0$, where m_0 is the electron rest mass; when excited with laser pulses of photon energy $\hbar\omega = 1.55 \text{ eV}$, then $E_e = 457 \text{ meV}$ and $E_h = -43 \text{ meV}$. Thus, carriers acquire so much energy that their average kinetic energy becomes higher than that of the lattice (i.e. LO phonon energy $\sim 26 \text{ meV}$). Such energetic electrons are known as hot electrons.

Single photon absorption is quantified by the linear absorption coefficient α which, in the case of photoexcited semiconductors, can be written as:

$$\alpha = \alpha_0[1 - f_e(K) - f_h(K)] \quad (2.16)$$

2. THEORETICAL BACKGROUND: ULTRAFAST DYNAMICS OF SOLIDS UNDER INTENSE LASER EXCITATION

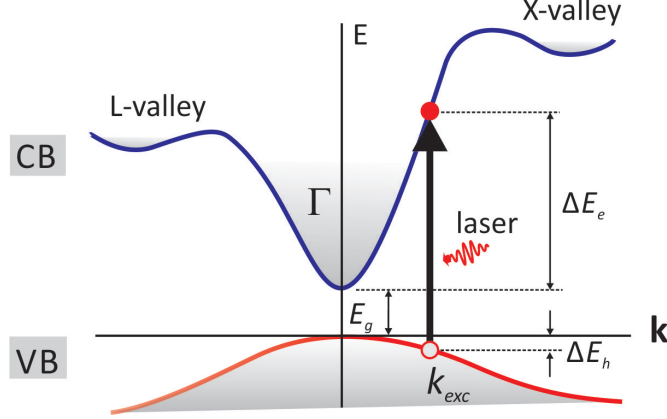


Figure 2.4: Interband transitions in a semiconductor with a direct band gap. - Conservation of the momentum implies that optical transitions lead to negligible changes in the wave vector of the electron and, thus, are represented by vertical arrows in the $E - K$ dispersion relation. A monochromatic laser pulse excites electron-hole pairs at specific points in the band structure with excess energies ΔE_e and ΔE_h .

where α_0 represents the absorption coefficient in the absence of photon excitation and, $f_e(K)$ and $f_h(K)$ are the distribution function of electrons and holes which in the equilibrium case can be represented by the Fermi-Dirac distributions with appropriate chemical potentials. The distribution functions $f_e(K)$ and $f_h(K)$ ensure the fulfillment of the Pauli exclusion principle, for example, the transition $VB \rightarrow CB$ can happen only if there is an electron in the initial state $E_v(k)$ ($1 - f_h(K) = 1$) and the upper state $E_c(k)$ is empty ($f_e(K) = 0$). In highly excited semiconductors the distribution functions $f_{e,h}$ evolves with time between 1 and 0 and this property can be used to probe the dynamics of the carriers in their respective bands. For a laser pulse with fluence (energy per unit area) F , the maximal carrier density generated by the SPA is given by:

$$n_{max}^{SPA} = \frac{(1 - R)\alpha F \sigma(t, \tau)}{\hbar\omega_{photon}} \quad (2.17)$$

where the $\sigma(t, \tau)$ is the laser pulse profile function, τ is the FWHM of the laser pulse.

For example, in the case of CdTe with typical experimental parameters $\alpha = 7.143 \times 10^5 \text{ m}^{-1}$, $R = 0.1$, $\hbar\omega_{photon} = 1.55 \text{ eV}$, $\tau = 60 \text{ fs}$ and $F = 0.1 \text{ mJ} \cdot \text{cm}^{-2}$, one obtains $n_{max}^{SPA} = 1.26 \times 10^{18} \text{ cm}^{-3}$. For excitation energies used in the experiments and, typically for fluences below the damage threshold of most semiconductors, the dominant

2.2 Photonexcitation, Relaxation, Recombination and Diffusion

multi-photon absorption mechanism is the TPA. In this case two laser photons excite an electron from a particular state $E_v(k)$ in the valence band to a state $E_c(k) = E_v(k) + 2\hbar\omega$ in the conduction band subject to the momentum conservation (equation 2.13). Two-photon absorption is quantified by the absorption coefficient β (generally, calculated using the second-order perturbation theory) whose largest value is when $\hbar\omega_{photon} < E_g$. However, even if $\hbar\omega_{photon} > E_g$, TPA can be large, and when the SPA is saturated due to the band filling, it becomes the dominant absorption mechanism, see figure 2.5.

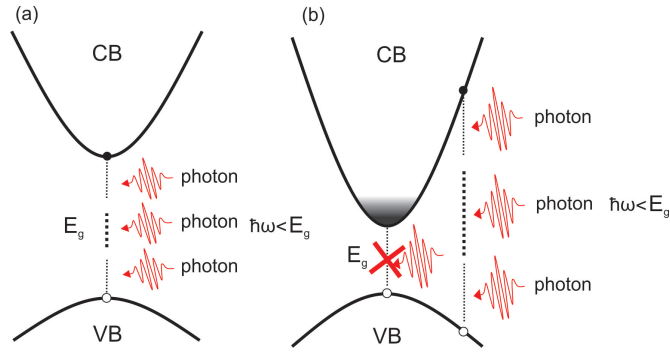


Figure 2.5: Schematic illustration of the multi-photon absorption process. - (a) the photon energy is smaller than the band gap (in this case the single photon absorption can not happen), and (b) the photon energy is greater than the band gap but the single photon absorption is saturated.

The maximal density of carriers generated by the TPA increases with the laser fluence as $[F\sigma(t, \tau)]^2$ and is given by:

$$n_{max}^{TPA} = \frac{(1 - R)\beta}{2\hbar\omega_{photon}} [F\sigma(t, \tau)]^2 \quad (2.18)$$

In laser excited GaAs, $\beta = 26 \text{ cm} \cdot \text{GW}^{-1}$, $R = 0.1$, $\hbar\omega_{photon} = 1.55 \text{ eV}$, $\tau = 60 \text{ fs}$ and $F = 5 \text{ mJ} \cdot \text{cm}^{-2}$, one obtains $n_{max}^{TPA} = 1.14 \times 10^{19} \cdot \text{cm}^{-3}$.

ii. Intraband absorption

The intraband absorption excites free carriers to a higher energy state within a band therefore does not increase the number of excited carriers, see the figure 2.6. The situation of intraband absorption is complex due to the intensive interactions between carriers which depends on the carrier concentrations. In semiconductors it's usually below 10^{21} cm^{-3} as compared to the order of 10^{23} cm^{-3} in metal, the absorption coefficient of free carriers can be expressed as:

2. THEORETICAL BACKGROUND: ULTRAFAST DYNAMICS OF SOLIDS UNDER INTENSE LASER EXCITATION

$$\alpha_{free} = \frac{\omega_p^2 \tau}{c(1 + \omega^2 \tau^2)} \quad (2.19)$$

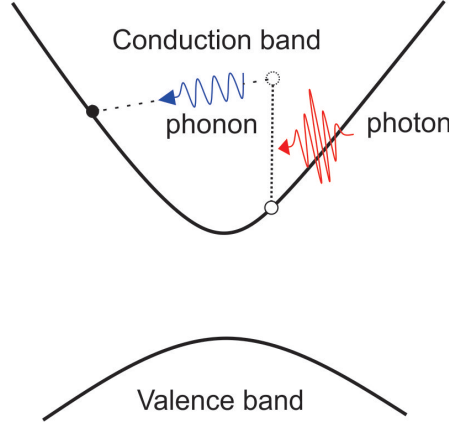


Figure 2.6: Intraband absorption and phonon-emission in the conduction band.

- One free electron is excited by the incident photon to higher energy position in the conduction band, accompanied with a phonon emission which is necessary to fulfill the momentum conservation between the initial and the final state of the free electron.

Carrier Thermalization

As a result of photonexcitation process carriers are generated with excess energies $\Delta E_{e,h}$, see the figure 2.4 and equation 2.15. During photonexcitation and immediately after, the distribution of carriers follows the spectral shape of the laser pulse [41]. Carrier-carrier (electron-electron, electron-hole and hole-hole) scattering redistributes them throughout the band (i.e. it alters the energy and the momentum of the carriers), as shown schematically in figure 2.7 and, depending on the density, within few tens of femtosecond the electron and hole populations approach the Fermi-Dirac distributions at elevated temperatures T_e and T_h , respectively, relative to the lattice temperature T_L . [20, 42, 43]. Carrier-carrier scattering is mediated by the Coulomb potential and the scattering rate W , in general, depends on the kinetic energy of carriers and on the carrier density. For example, for electron-electron scattering $W_{e-e} \propto n/\Delta E_e^{3/2}$ [37]. However, as the electron density increases, so do the occupation factors f_e , f_h and the screening of the Coulombic potential. Thus, carrier-carrier scattering does not increase by following a simple density dependence but rather a complicated one which after some critical electron density should decrease.

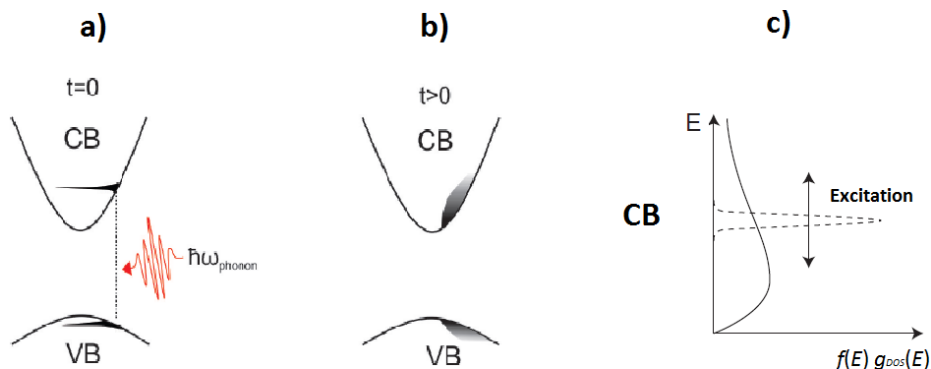


Figure 2.7: Schematic illustration of the photonexcitation of electron and holes and their redistributions. - (a) During the photonexcitation and immediately after, the distribution of carriers follows the spectral shape of the laser pulse. (b) Carrier-carrier scattering redistributes hot carriers throughout their respective bands and causes the initial nonthermal distribution to take on a Fermi-Dirac distribution (c).

Carrier-Phonon Scattering

In semiconductors atoms vibrate about their rigid lattice sites. The origin of these vibrations can be (i) thermal (population of phonon modes increases with the lattice temperature) and (ii) due to the photon excitation. As one might suspect, since the electronic band structure is determined by the periodic potential which depends on the rigid position of the atoms, under the presence of atom vibrations, electrons will experience slightly a different potential relative to the case when they traverse a crystal whose atoms are completely frozen in space. When atomic vibrations perturb the potential for a short period of time, they may induce a transition of an electron from an initial state with a crystal momentum $\hbar K$ to a different final state with a crystal momentum $\hbar K'$, in other words, the electron is scattered by a phonon, see the figure 2.8 [37, 44].

Carrier-lattice scattering is the main mechanism which transfers the energy from the hot-carrier system to the lattice, in other words, carriers cool down and the lattice gets heated. In general, vibrations of the ions about their equilibrium positions introduce a time-dependent term, the electron-phonon coupling $H_{e\text{-phonon}}$, in the Schrödinger equation of the electrons [37, 38]. This interaction term is usually weak enough to be regarded as a small perturbation which induces transitions between the unperturbed states. Then, the carrier-phonon scattering rate (number of scattering events per unit

2. THEORETICAL BACKGROUND: ULTRAFAST DYNAMICS OF SOLIDS UNDER INTENSE LASER EXCITATION

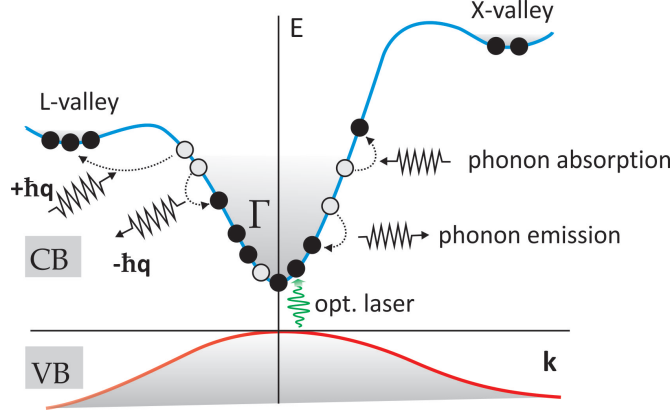


Figure 2.8: Schematic illustration of the intravalley scattering processes. - Transition of a carrier from an initial state with a crystal momentum $\hbar K$ to a different final state with a crystal momentum $\hbar K'$ is governed by the conversion of energy, conversion of the momentum and the Pauli exclusion principle.

time) is given by the Fermi's Golden rule as:

$$W_{fermi} = \frac{2\pi}{\hbar} |\langle \phi_k | H_{e-phonon} | \phi_{k'} \rangle|^2 \delta(E_k - E_{k'} - \hbar\omega_q) \quad (2.20)$$

where $\hbar\omega$ is the phonon energy exchanged during the scattering event. Conservation of energy and momentum implies that:

$$E_k - E_{k'} = \hbar\omega_q \quad (2.21)$$

$$K' = K \pm q \quad (2.22)$$

where q is the phonon wave vector. The signs “+” and “-” stand for phonon absorption and emission, respectively.

The main scattering mechanism in semiconductors subject to high excitation fluences are deformation potential scattering (DPS) and polar optical scattering (POPS). While the deformation potential scattering occurs in all solids, polar optical scattering is present only in polar semiconductors.

Deformation Potential Intravalley Scattering

Deformation potential scattering arises, as the name suggests, from the deformation of the lattice by phonons or by the motion of the carriers (since both phonons and carriers are coupled). This scattering mechanism can arise from both acoustic phonons (acoustic scattering) and optical phonons (nonpolar optical scattering) and conservation of energy and momentum restricts it to small \mathbf{q} -modes ($\mathbf{q} \approx 0$). In the case of acoustic

2.2 Photonexcitation, Relaxation, Recombination and Diffusion

scattering, when phonons perturb the lattice by Δa , where a is the lattice constant, the carrier energy will change by $\Delta\epsilon_c$. For small Δa (on the order of 10^{-12} m or less) one can assume that $\Delta\epsilon_c$ is linearly proportional to Δa :

$$\Delta\epsilon_c = D_c \frac{\Delta a}{a} \quad (2.23)$$

The proportionality factor D_c is called the deformation potential. Deformation potentials for the conduction and valence bands can be deduced from the experiments and are tabulated in the literature, e.g., [45]. Since acoustic phonons displace the neighboring atoms in the same direction, changes in the lattice spacing are produced by the strain ∇u . Motivated by equation 2.23 the electron-phonon coupling term for acoustic deformation potential scattering is written as:

$$H_{e-phonon} = D_c \nabla u \quad (2.24)$$

take equations 2.20 and 2.24, and assuming parabolic energy bands, the scattering rate for acoustic phonon scattering is:

$$W_{ADPS}(E) = \frac{2\pi D k_B T}{\hbar \rho v_s^2} g_{DOS}(E) \quad (2.25)$$

where D is the deformation potential, ρ is the mass density, v_s is the speed of sound, T is the lattice temperature and E is the carrier energy. Thus, the acoustic phonon scattering is proportional to the lattice temperature and the $g_{DOS}(E)$ for the carriers. In figure 2.9 shows a plot of the scattering time as a function of electron energy for CdTe, and one can see the scattering times are of the order of ps^{-1} . This scattering mechanism is usually dominant at low carrier energies (lower than the optical phonon energy).

The treatment of the nonpolar optical scattering proceeds much like the acoustic scattering with the exception that here, since the atoms vibrate against each other and the phonons are more energetic, the energy levels are affected directly by the displacement u (and not by the strain ∇u as in the case of acoustic phonons) and the interaction Hamiltonian can be written as:

$$H_{e-phonon} = D_o u \quad (2.26)$$

with D_o being the optical deformation potential and u the relative displacement of two atoms in the basis. The scattering rate is:

$$W_{ODPS} = \frac{\pi D_o^2}{\rho \omega_0} \{n(\omega_0) g_{DOS}(E + \hbar\omega_0) + [n(\omega_0) + 1] g_{DOS}(\hbar\omega_0)\} \quad (2.27)$$

2. THEORETICAL BACKGROUND: ULTRAFAST DYNAMICS OF SOLIDS UNDER INTENSE LASER EXCITATION

where ω_o is the phonon energy and $n(\omega_o)$ is the phonon occupation number given by:

$$n(\omega_o) = \frac{1}{e^{\hbar\omega_o/k_B T} - 1} \quad (2.28)$$

This scattering mechanism is faster than the acoustic scattering (on the order of hundreds of femtosecond) however it is restricted by the crystal symmetry (i.e. it is not allowed for all directions of the Brillouin zone). For example, selection rules forbid optical scattering in zinc blende semiconductors (CdTe and GaAs) at Γ valley and along $\Gamma - X$ direction.

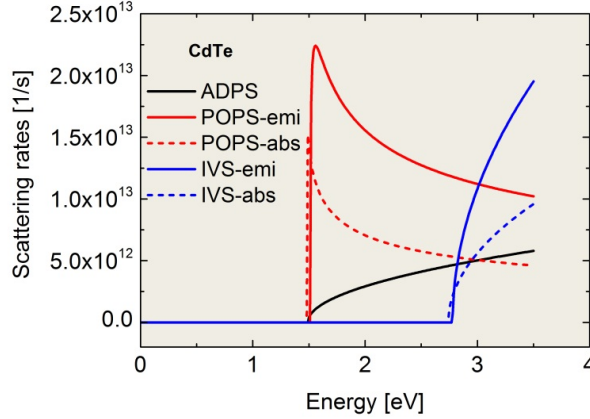


Figure 2.9: A comparison of acoustic scattering, polar optical scattering and intervalley scattering in CdTe at room temperature. - The scattering rates are computed using equations 2.25, 2.29 to 2.31, respectively.

Polar Optical-Phonon Scattering

Compound semiconductors such as CdTe and GaAs have a polar character; the two atoms in the unit cell possess an effective charge e^* (e.g. for CdTe $e^*/e = 2.35$). When the cation ($+e^*$) and anion ($-e^*$) vibrate against each other in a longitudinal optical phonon mode with a relative displacement u , the dipole moment of the cation-anion pair is perturbed by an amount $\delta p = e^*u$ which then changes the electric field experienced by the charged carriers and, consequently, their potential energy which mediates the transition probability. This scattering mechanism depends linearly on the effective charge and favors optical phonons near the center of the Brillouin since the interaction potential is of the form $H_{e-phonon} \propto \frac{e^*}{|q|}$. In the framework of parabolic band approxi-

2.2 Photonexcitation, Relaxation, Recombination and Diffusion

mation the scattering rate for the polar optical-phonon scattering (POP) scattering is given by [37].

$$W_{POPS} = W_{POPS}^{emission} + W_{POPS}^{absorption} \quad (2.29)$$

$$W_{POPS}^{emission} = const.(e^*)^2 [n(\omega_o) + 1] \sinh^{-1}(E/\hbar\omega_o - 1)^{1/2} \quad (2.30)$$

$$W_{POPS}^{absorption} = const.(e^*)^2 n(\omega_o) \sinh^{-1}(E/\hbar\omega_o)^{1/2} \quad (2.31)$$

Figure 2.9 shows the POPS rates for electrons in CdTe at room temperature. It is evident that this scattering mechanism is very frequent with scattering rates up to $\sim 2 \times 10^{13} s^{-1}$ and the phonon emission rate is larger than the phonon absorption rate which means that the carriers lose their excess energies primarily by emitting LO phonons (i.e. they heat the lattice). Polar optical phonon scattering is the dominant scattering mechanism in compound semiconductors at room temperature. Polar scattering involving acoustic phonons is dominant only for excess energies smaller than the LO phonon energy $\hbar\omega_o$.

Intervalley Scattering

Semiconductor band structures are usually characterized with multiple valleys (see the figure 2.1). Assisted by phonons of a relatively large wave vector q , electrons can scatter from one valley to another. Since these valleys have different effective masses (i.e. different curvatures in the $E - K$ relationship), intervalley scattering plays a very important role in the charge transport [37, 38]. The mathematical treatment of intervalley scattering is dealt on the same footing as the nonpolar deformation potential scattering by simply postulating a deformation potential like interaction of the form:

$$H_{e-phonon} = D_{if}u \quad (2.32)$$

where D_{if} is the intervalley potential and characterizes the strength of the scattering from the initial valley i to the final valley f . Energy conservation ensures that an electron can not scatter from, for example, the Γ valley to the L valley unless the electron energy is equal to $\Delta E_{\Gamma L}$ or at least $\Delta E_{\Gamma L} - \hbar\omega_{\Gamma L}$ in the case the electron absorbs one phonon of energy $\hbar\omega_{\Gamma L}$, see the figure 2.10.

2. THEORETICAL BACKGROUND: ULTRAFAST DYNAMICS OF SOLIDS UNDER INTENSE LASER EXCITATION

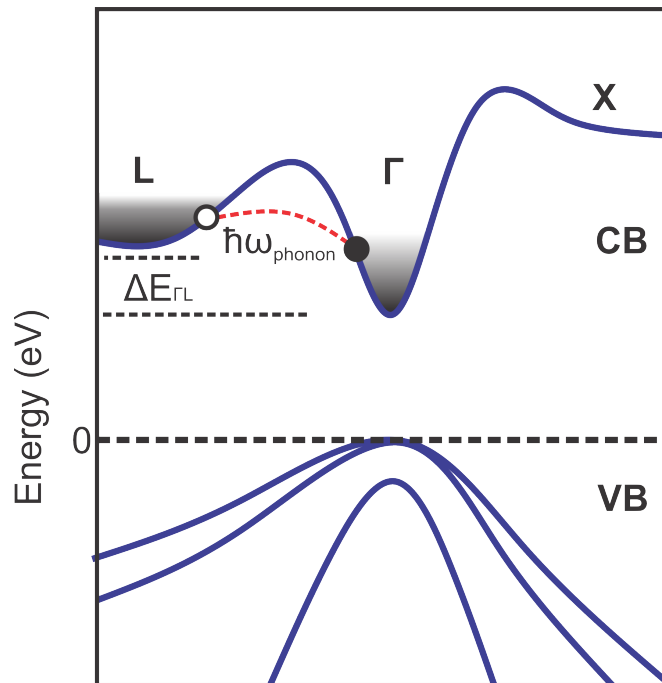


Figure 2.10: Schematic illustration of the intervalley scattering process. - Electrons in the Γ valley can scatter into the L valley and vice versa by absorbing or emitting an appropriate phonon. Energy conservation ensures that an electron can not scatter from the Γ to the L valley unless the electron energy is equal to $\Delta E_{\Gamma L}$ or at least $\Delta E_{\Gamma L} - \hbar\omega_{\Gamma L}$ in which case the electron absorbs one phonon of energy $\hbar\omega_{\Gamma L}$. This scattering process is important at high electric fields and leads to the negative differential resistance in semiconductors.

2.2 Photonexcitation, Relaxation, Recombination and Diffusion

Using equation 2.32 and 2.20, the intervalley scattering rate can be written as:

$$W_{IVS} = W_{IVS}^{emission} + W_{IVS}^{absorption} \quad (2.33)$$

$$W_{IVS}^{absorption} = \frac{\pi D_{if}^2 Z_f}{\rho \omega_{if}} n(\omega_{if}) g_{DOS}(E + \hbar \omega_{if} - \Delta E_{if}) \quad (2.34)$$

$$W_{IVS}^{emission} = \frac{\pi D_{if}^2 Z_f}{\rho \omega_{if}} n(\omega_{if} + 1) g_{DOS}(E - \hbar \omega_{if} - \Delta E_{if}) \quad (2.35)$$

where Z_f is the number of equivalent valleys available for scattering and $g_{DOS}(E)$ is the density state of the final valley. For example, in the case of L-valleys in CdTe, Z_f is 4. Typical results for intervalley scattering $\Gamma - L$ in CdTe are shown in figure 2.9. This scattering mechanism, significant for dense electron-hole plasmas and high carrier energies, may further influence the thermalization time scale by reheating the carriers and reducing the cooling rate [46, 47]. Also, it plays an important role during the photonexcitation by clearing the phase space for further transitions (i.e. it opposes the band filling).

Carrier Recombination

The final step for the equilibration of carriers is the recombination process, where the electrons in the conduction band recombine with the holes in the valence band. This process is divided into multiple types, the two most important mechanisms in semiconductors are the radiative recombination and the Auger recombination, as shown at the figure 2.11(a). The radiative recombination describes the process that electrons in the conduction band directly recombine with the holes in the valence band. During this process a fluorescence photon with the energy equal to the energy gap of the semiconductor is emitted. In Auger recombination no photon is emitted, but energy is transferred to a third carrier, exciting this carrier to a higher energy position in the same band, see the figure 2.11(b). These relaxation processes are the major mechanisms which reduce the number of excited carriers.

Radiative recombination is a two-body process thus, it is proportional to the square of the density of carriers (N^2). The recombination rate equation can be written as:

$$\frac{\partial N(t)}{\partial t} = -R_{Rad} N(t)^2 \quad (2.36)$$

Where R_{Rad} is the radiative recombination coefficient.

2. THEORETICAL BACKGROUND: ULTRAFAST DYNAMICS OF SOLIDS UNDER INTENSE LASER EXCITATION

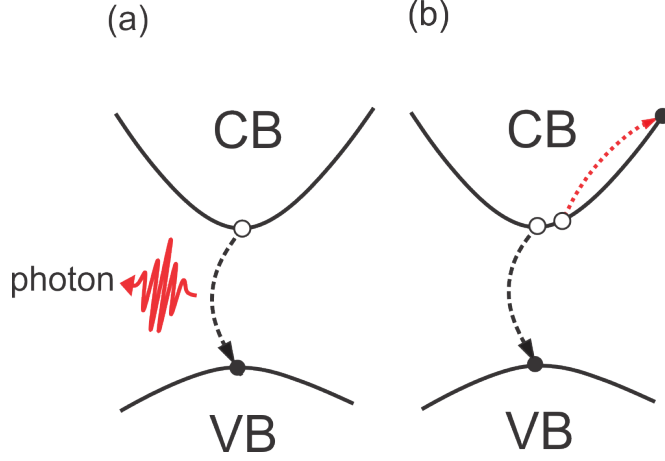


Figure 2.11: Illustrate the Radiative and Auger recombination. - (a) Radiative recombination: electrons in the conduction band directly recombine with holes in the valence band accompanied with a fluorescence photon whose energy is equal to the energy gap of the semiconductor, (b) Auger recombination: the electron in conduction band relaxes by transferring its energy to another electron.

In Auger recombination, however, three particles are involved. The corresponding recombination rate equation is given as:

$$\frac{\partial N(t)}{\partial t} = -R_{Aug}N(t)^3 \quad (2.37)$$

R_{Rad} in GaAs is about $7.2 \times 10^{-10} \text{ cm}^3 \cdot \text{s}^{-1}$ at 300 K, with an initial laser excited carrier density of $N_0 = 10^{19} \text{ cm}^{-3}$, the density of carriers changes as illustrated in figure 2.12, and R_{Aug} has a typical value of about $10^{-30} \text{ cm}^6 \cdot \text{s}^{-1}$, which is shown in figure 2.13.

The radiative recombination is the dominating mechanism at low carrier concentration. On the other hand, the Auger recombination is recognized to be the main mechanism at high carrier concentration, which enhances the cross section of carrier scattering.

Radiative and Auger recombination processes typically compete in a wide range of carrier concentrations.

Carrier Diffusion

Apart from recombination, carriers can move away from excited areas by diffusion. This process does not reduce the overall number of carriers, but rather changes the

2.2 Photonexcitation, Relaxation, Recombination and Diffusion

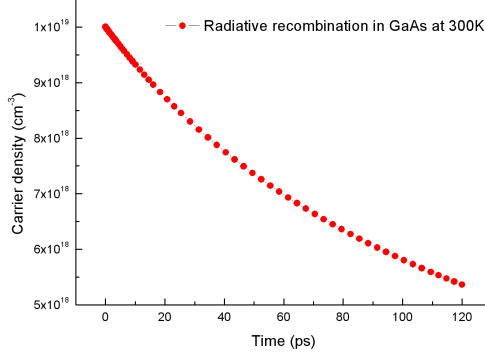


Figure 2.12: After 100 ps the carrier density has reduced to half the amount.

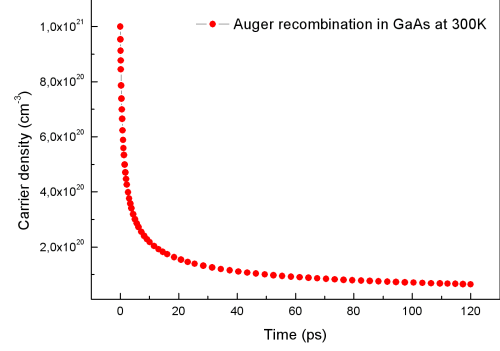


Figure 2.13: Within few ps, Auger recombination reduces the carrier density by an order of magnitude.

carrier density distribution from surface to bulk, or in general, carriers diffuse from higher concentrated areas to the lower concentrated area, see the figure 2.2.

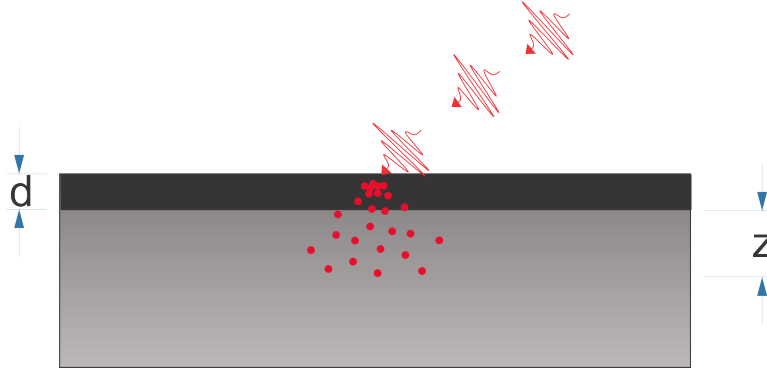


Figure 2.14: Carrier diffusion. - d is the laser penetration depth, z is the diffusion distance from the laser excited area.

The temporal change of carrier density due to diffusion is described as follows:

$$\frac{\partial N(z, t)}{\partial t} = -D_{diff} \frac{\partial^2 N(z, t)}{\partial z^2} \quad (2.38)$$

Where D_{diff} is the diffusion constant.

2. THEORETICAL BACKGROUND: ULTRAFAST DYNAMICS OF SOLIDS UNDER INTENSE LASER EXCITATION

2.3 Modeling Carrier and Lattice Dynamics

Carrier Dynamics in Photonexcited Semiconductors: The Stanton-Bailey model

Carrier dynamics in photoexcited semiconductors is characterized by the evolution of the distribution function f which gives the probability that a particular state in the energy band of semiconductor is occupied. In general, the distribution function $f(E,t)$ changes as the carriers are generated, undergo scattering with themselves and the lattice, are recombined and diffuse from the probed region. The main tool to model the evolution of f and thus describe the ultrafast dynamics in photonexcited semiconductors is the time-dependent Boltzmann transport equation [44]. In the case where the carrier diffusion is much slower than carrier-carrier and carrier-lattice scattering times, this equation can be stated as:

$$\frac{df}{dt} = \left. \frac{df}{dt} \right|_{scattering} + G - R \quad (2.39)$$

where the first term in the right side of equation 2.39 represents the change of f due to the scattering processes (carrier-carrier and carrier-lattice), G is a source term that stands for the generation of the carriers (its related to the single- and multi-photon absorption rates) and R stands for the recombination (in the case of highly excited semiconductors, Auger recombination). The scattering term can be written as:

$$\left. \frac{df}{dt} \right|_{scattering} = \sum_{k'} W(k', k) f(k', t) [1 - f(k, t)] - W(k, k') f(k, t) [1 - f(k', t)] \quad (2.40)$$

where W stands for the scattering rates of various processes (carrier-carrier and carrier-lattice scatterings). The first term represents the out-scattering processes where the carriers are scattered from the state k to a state k' , whereas the second term describes the in-scattering processes where the carriers are scattered to the state k .

From equation 2.39 and 2.40 one can see that an exact mathematical treatment would involve integro-differential equations and the solution of equation 2.39 would be very challenging. A valuable model which provides insight into the qualitative and quantitative carrier dynamics, isolating characteristics that are often lost in a more detailed calculation is the four-state model proposed by Stanton and Bailey [48]. This model has been successfully applied to explain femtosecond mobility and time-resolved luminescence experiments. Here, the conduction band of a semiconductor is divided into four energy states (see the figure 2.15). All Γ -valley electrons with enough energy to transfer into the L valleys are in the Γ_+ state; Γ valley electrons with energy less

than the minimum of the L-valley are in the Γ_- state. Electrons in the L valley can scatter back to Γ_+ through intervalley scattering. The fourth state Γ_0 was introduced to account for the electrons at the bottom of the conduction band which contribute on the photoluminescence signal. The Γ_- state represents all the electrons with energies ranging from one optical phonon energy above the band edge to energies just below the threshold for scattering into the L valley. Population of the Γ_- state is changed through the POP scattering: it is populated by the electrons in the Γ_+ states and depopulated when the electrons relax towards the Γ_0 state.

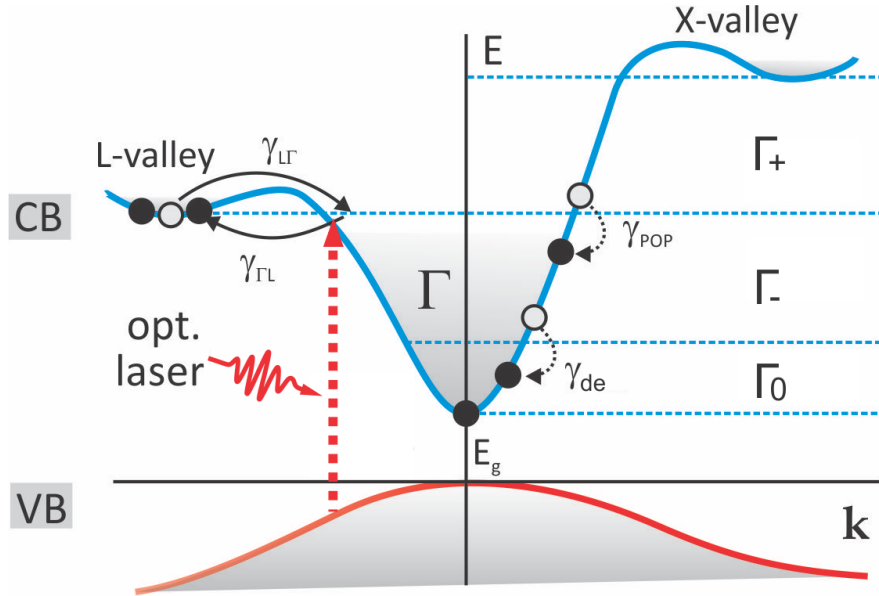


Figure 2.15: The Stanton-Bailey four-state model. - Γ -valley electron with enough energy to transfer into the L valleys are in the Γ_+ state; they scatter into the L valley via intervalley scattering with a rate $\gamma_{\Gamma L}$. Electrons in the L valley scatter back to the Γ_+ level with an intervalley scattering rate $\gamma_{L\Gamma}$. All Γ valley electrons with energy less than the minimum of the L-valley are in the Γ_- state. Electrons in the Γ_+ level relax towards the Γ_- level by emitting LO phonons via POP scattering with a rate γ_{POP} . Similarly, electrons in the Γ_- level relax towards the band edge by emitting LO phonons with a rate γ_{de} .

Mathematically, the Stanton-Bailey model can be expressed by four coupled differ-

2. THEORETICAL BACKGROUND: ULTRAFAST DYNAMICS OF SOLIDS UNDER INTENSE LASER EXCITATION

ential equations:

$$\frac{dN_{\Gamma_+}}{dt} = -\gamma_{\Gamma L}N_{\Gamma_+} + \gamma_{L\Gamma}N_{\Gamma_+} - \gamma_{pop}N_{\Gamma_+} \quad (2.41)$$

$$\frac{dN_L}{dt} = \gamma_{\Gamma L}N_{\Gamma_+} - \gamma_{L\Gamma}N_L \quad (2.42)$$

$$\frac{dN_{\Gamma_-}}{dt} = \gamma_{pop}N_{\Gamma_+} - \gamma_{de}N_{\Gamma_-} \quad (2.43)$$

$$\frac{dN_{\Gamma_0}}{dt} = \gamma_{de}N_{\Gamma_-} \quad (2.44)$$

These equations describe population and depopulation of the various levels in the conduction band; in other words, they describe the dynamics of the electrons as they scatter and relax towards the band edge. Here, γ_{POP} is the POP scattering rate for the relaxation Γ_+ to Γ_- , $\gamma_{\Gamma L}$ is the intervalley scattering rate for the transitions Γ_+ to L valley, $\gamma_{L\Gamma}$ is the intervalley scattering rate for the transitions from L valley to Γ_+ , and γ_{de} is the scattering rate for the relaxation Γ_- to Γ_0 . In figure 2.16, the electron density for the four levels evolving with time is shown (assuming certain scattering and relaxation rate for CdTe).

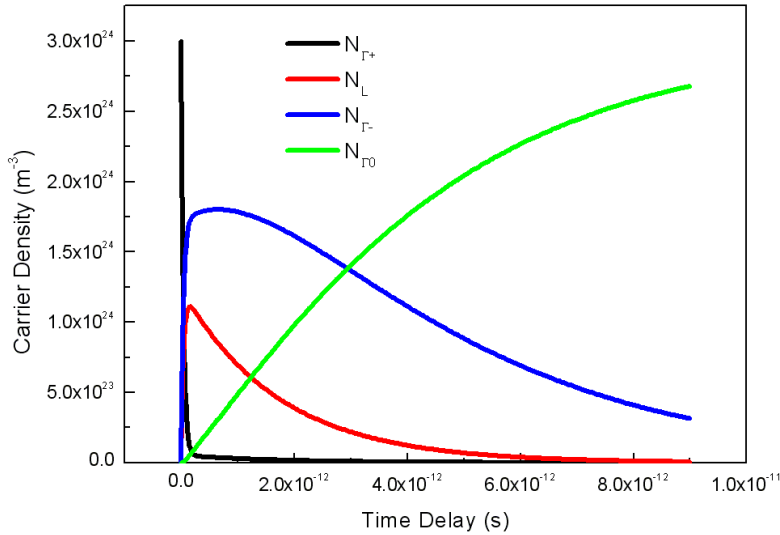


Figure 2.16: A simulation based on the Stanton-Bailey model. - Assume an initial photoexcited electron at Γ_+ is $3 \times 10^{18} \cdot cm^{-3}$ and certain scattering and relaxation rate in CdTe.

Phonon-Plasmon Coupled Modes

In highly excited semiconductors where the carrier density is above the Mott density [49] (normally, $n_{e,h} > 10^{18} \cdot \text{cm}^{-3}$), the excited carriers (electrons and holes) form a new state of matter, the electron-hole plasma, whose natural behavior is characterized by the plasma frequency $f_e = \sqrt{e^2 n_e / (\epsilon_\infty m_{eh})}$, where m_{eh} is the reduced electron-hole mass. The electron-hole plasma can be coupled via Coulomb interactions with the motions of the charged lattice-ions, mixing thus the phonon and plasmon character to a new form of collective oscillations called LO phonon-plasmon coupled modes (LOPC modes) [37].

In polar semiconductors such as CdTe and GaAs, LOPC modes can be coherently excited by illuminating the sample with ultrashort laser pulses whose time duration is shorter than the LO phonon wavelength. A widely accepted generation mechanism is the so-called ultrafast screening of the surface space charge region [12, 15, 50].

In general, the termination of the periodic structure of a semiconductor at its free surface typically forms surface states (SS) which are localized within the band gap [51], see the figure 2.17. The appearance of such surface-localized states induces charge transfer between the bulk and the surface in order to establish thermal equilibrium between the two, leading to the bending of the conduction and valence band. This charge transfer results in a non-neutral region with a finite electric field (in CdTe, 48-460 kV/cm for doping densities between $1 \times 10^{16} \cdot \text{cm}^{-3}$ to $1 \times 10^{18} \cdot \text{cm}^{-3}$) near the surface, usually referred to as the surface space charge region (SCR), which may extend quite deeply into the bulk (in CdTe, 26-270 nm for doping densities between $1 \times 10^{18} \cdot \text{cm}^{-3}$ to $1 \times 10^{16} \cdot \text{cm}^{-3}$).

The built-in surface electric field F_{SCR} introduces a finite displacement of ions, see the figure 2.18. When an ultrafast laser pulse illuminates the crystal surface with photon energies greater than the band gap, the photoexcited carriers will screen the built-in electric field. When the screening of the surface field is very fast, atoms will overshoot their equilibrium position at $F_{SCR} = 0$ thus launching coherent longitudinal phonons. Both, coherent phonons and surface space-charge are intimately related to the details of the band structure. When the built-in electric field changes and lattice vibrations move atoms, photoexcited carriers encounter perturbations -they are knocked from a state with energy $E(k_1)$ to $E(k_2)$.

The theoretical description of the phonon-plasmon modes is based on the coupled equations for the plasmon-phonon dynamics outlined in [15], which have been successfully used to describe experimental results related to the coupling of coherent optical

2. THEORETICAL BACKGROUND: ULTRAFAST DYNAMICS OF SOLIDS UNDER INTENSE LASER EXCITATION

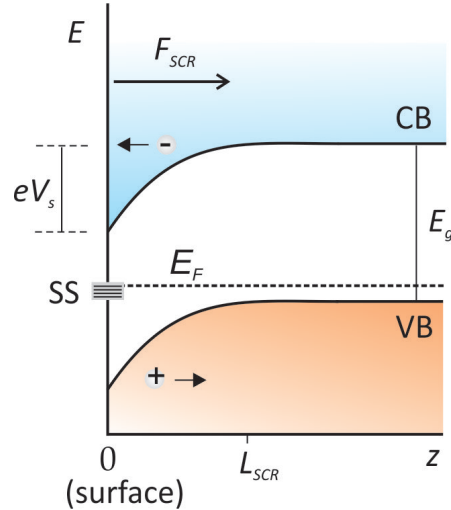


Figure 2.17: Band diagram of a p-doped semiconductor. - The appearance of surface localized states (SS) leads to the band bending (with a maximal value $e \times V_s$, where V_s is the surface potential). The static electric field SCR drives the two kinds of photoexcited carriers in opposite directions, thus screening the built-in electric field.

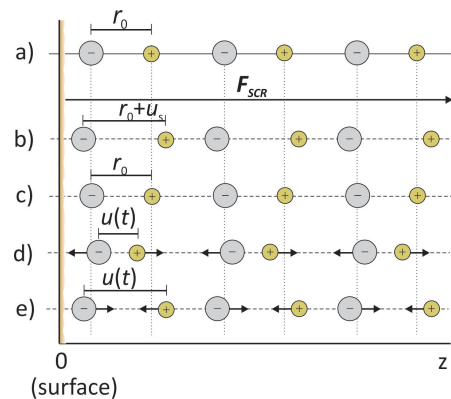


Figure 2.18: The optical phonon generation mechanism in a polar semiconductor. - (a) In the absence of the external surface-induced electric field (unperturbed case) the separation of Cd and Te atoms is equal to nearest neighbor separation $r_0 = 2.776 \text{ \AA}$, (b) When the electric field F_{SCR} is applied, atoms will follow it in accordance with their charge, and the chain will be deformed longitudinally with $r_0 + u_s > r_0$ near the surface, (c) Ultrafast excitation of electron-hole pairs leads to an ultrafast screening of the electric field, (d) and (e), Because the lattice possesses inertia, atoms will overshoot their equilibrium position r_0 and will launch coherent optical phonons.

2.3 Modeling Carrier and Lattice Dynamics

phonons and plasmons in bulk semiconductors:

$$\frac{d^2 P_e}{dt^2} + \gamma_e \frac{dP_e}{dt} + \omega_e^2 P_e = \omega_e^2 (\epsilon_0 F_{SCR} - \gamma_{12} w) \quad (2.45)$$

$$\frac{d^2 w}{dt^2} + \gamma_L \frac{dw}{dt} + \omega_{LO}^2 P_e = \frac{\gamma_{12}}{\kappa_\infty} (F_{SCR} - \frac{p_e}{\epsilon_0}) \quad (2.46)$$

where P_e is the electronic polarization, γ_e is the electron momentum relaxation time, $w = u\sqrt{M/V_0}$ is the normalized lattice displacement (M is the cation-anion effective mass and V_0 is the volume of the primitive unit cell), $\gamma_{12} = \omega_{TO}\sqrt{\epsilon_s - \epsilon_\infty}$ is the coupling parameter (ϵ_s and ϵ_∞ are low frequency and high frequency dielectric constants, respectively), ω_{TO} is the TO phonon frequency, ω_{LO} is the LO phonon frequency and γ_L is the damping constant of the phonon oscillations which is related to the anharmonic decay of LO phonons [15]. The first equation describes the electron-hole plasma modes which in the absence of coupling (i.e. $\gamma_{12} = 0$) oscillate with a plasma frequency ω_e . Similarly, the second equation describes optical phonons which, when $\gamma_{12} = 0$ oscillate with LO phonon frequency ω_{LO} . When $\gamma_{12} \neq 0$, long-range Coulomb coupling of the ultrafast field transient to both the electronic polarization and the polar lattice initiate collective oscillations whose frequencies can be determined by the equation:

$$\omega^4 - i(\omega_e + \omega_L)\omega^3 - (\omega_e^2 + \omega_{LO}^2 + \gamma_e\gamma_L)\omega^2 + i(\gamma_L\omega_e^2 + \gamma_e\omega_{LO}^2)\omega + \omega_e^2 + \omega_{TO}^2 = 0 \quad (2.47)$$

This equation has four solutions. However, only two of them have physical meaning, ω_+ and ω_- , and they represent the LOPC modes. Figure 2.19 shows the carrier density dependence of ω_+ and ω_- . When the electron density is high ($n_{e,h} > 10^{18} \text{cm}^{-3}$) the solution ω_- corresponds to a LOPC mode having the character of an LO optical phonon which, due to the screening by the free carriers, oscillates at a frequency ω_{TO} (i.e. $\omega_- \approx \omega_{TO}$) whereas ω_+ corresponds to a LOPC mode having a plasmon character (i.e. $\omega_+ \approx \omega_e$). For low electron densities ($n_{e,h} < 10^{16} \text{cm}^{-3}$) ω_+ has a phonon character ($\omega_+ \approx \omega_{LO}$), whereas ω_- has a plasmon character ($\omega_- \approx \omega_e$). At intermediate electron densities the LOPC modes exhibit a mixed phonon-plasmon character.

The time evolutions of the electric field in the space-charge region $E(t) = F_{SCR} - \frac{P_e}{\epsilon_0} - \frac{\gamma_{12}w}{\epsilon_0}$ is computed from the numerical solution of equations 2.45 and 2.46 for different electron densities and the Fourier transforms of these curves are shown in figure 2.20. The Fourier transform of the surface space-charge electric field $E(t)$ shows the ω_+ and ω_- modes and their evolution with electron density conforms the LOPC

2. THEORETICAL BACKGROUND: ULTRAFAST DYNAMICS OF SOLIDS UNDER INTENSE LASER EXCITATION

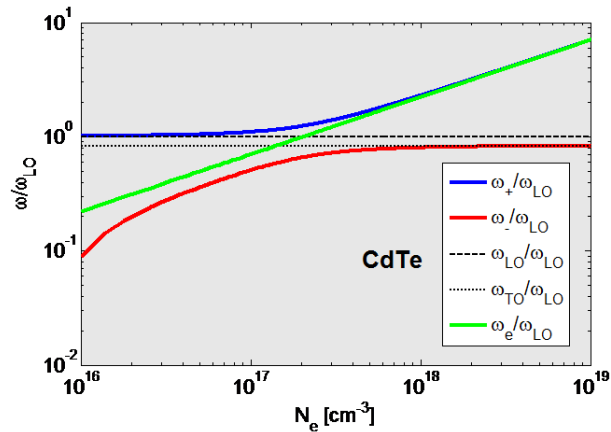


Figure 2.19: Phonon-plasmon coupled-modes in CdTe. - Frequencies in the long-wavelength limit for electrons and LO phonons are computed from the solutions of equation 2.47.

dispersion relation (see the figure 2.47). At high electron densities the high-frequency plasmons are stronger than the phonon-like mode which due to the screening converges into the TO phonon frequency; at intermediate densities both modes can achieve equal magnitudes. At low electron densities the plasmon peak becomes broader while the phonon peak converges to the LO phonon frequency.

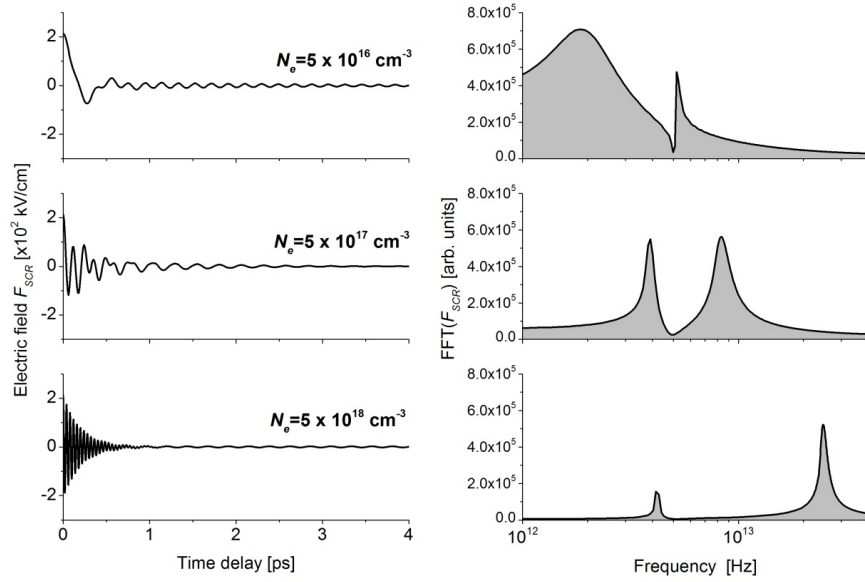


Figure 2.20: Time evolutions of the electric field in the space charge region in CdTe. - $E(t) = F_{SCR} - \frac{P_e}{\epsilon_0} - \frac{\gamma_{12}w}{\epsilon_0}$ is computed from the numerical solution of equations 2.45 and 2.46 for different electron densities and their Fourier transforms.

2. THEORETICAL BACKGROUND: ULTRAFAST DYNAMICS OF SOLIDS UNDER INTENSE LASER EXCITATION

Chapter 3

Ultrafast Dynamics in Highly Excited CdTe: The Time-Resolved Reflectivity Measurement

3.1 Introduction

The study of carrier and lattice dynamics in semiconductors under nonequilibrium conditions has been a rich subject of research in the last few decades [52, 53, 54]. Many techniques have been developed and applied to investigate such dynamics, and an impressive level of insight has been obtained [50], [55], [56], [16], [43]. A popular technique is the pump-probe reflectivity which involves excitation and probing of the sample using conventional light source such as visible or near-visible laser with a photon energy comparable with the energy gap of the semiconductors. This chapter presents the pump-probe time-resolved reflectivity measurements in a doped CdTe crystal carried out within this thesis. The objective was to study the effect of the hot carriers on the time-resolved reflectivity changes of the crystal which was excited at various fluences covering a range from weak to strong Coulomb screening.

CdTe is a II-VI polar semiconductor which has a zinc-blende type lattice structure (figure 3.1). It has a direct band energy gap of ~ 1.5 eV. The band structure of CdTe is shown in figure 3.2.

A 800 nm photon (~ 1.55 eV) can be directly absorbed by CdTe generating one electron near the conduction band minimum and one hole near the valence band max-

3. ULTRAFAST DYNAMICS IN HIGHLY EXCITED CDTE: THE TIME-RESOLVED REFLECTIVITY MEASUREMENT

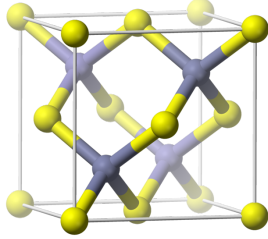


Figure 3.1: The yellow and grey balls indicate the positions of the telluride and cadmium atoms, respectively.

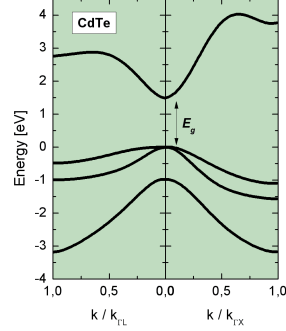


Figure 3.2: The fundamental energy gap E_g is 1.5 eV.

imum. When the pump power is increased, the two-photon absorption (TPA) channel becomes available, exciting carriers to the higher position in the bands. Following photoexcitation, carriers relax their energy mainly by the electron-phonon interactions. In this way, the carrier population is cooled whereas the lattice is heated. Although CdTe is an important material with a wide range of applications (such as solar cells, infrared, X-ray and γ -ray detectors [8, 9, 10]), experimental work on the ultrafast dynamics is rare [11, 12, 13]. Especially, if one compares it with the very well studied polar semiconductor GaAs [14, 15, 16, 17, 18, 19, 20]. In [12] Ishioka et al. reported the time-resolved reflectivity on bulk CdTe. The authors measured coherent longitudinal optical phonons (LO phonons) generated from the ultrafast screening of the surface space-charge region in the depletion layer (see the figure 2.17) by the photoexcited carriers. Limited by available laser power, their measurement was performed in a low-fluence regime from 4.4 to 88 $\mu\text{J}\cdot\text{cm}^{-2}$. They found out that the LOPC mode (see the section 2.3) is not prominent at their photoexcitation fluence regime which they expected to be evident at higher fluence. In this work, the ultrafast carrier and lattice dynamics of CdTe were probed for excitation fluences spanning about three orders of magnitude, from 0.064 $\text{mJ}\cdot\text{cm}^{-2}$ to 6.14 $\text{mJ}\cdot\text{cm}^{-2}$. The LOPC modes were observed as expected (see the section 2.3) and, in addition, diverse ultrafast phenomena appear when the fluence increases. In order to extract the physics behind these measurements, a model which considers carrier-lattice interaction, two-photon absorption and Coulomb screening induced effects has been applied.

This chapter starts with a brief introduction to the experimental set up used to measure the time-resolved reflectivity from the laser-excited CdTe crystal. Section

3.2 Optical Pump-Probe Experimental Setup

3.3 gives a brief summary of the optical response of a sample subject to intense laser excitation: optical properties of the electron-hole plasma and the dynamics of carriers. Experimental results and discussion are presented in section 3.4 and, finally, the concluding remarks are given in section 3.5.

3.2 Optical Pump-Probe Experimental Setup

The laser pulses of about 60 fs duration, a wavelength of 800 nm and a repetition rate of 1 kHz, generated by a commercially available Ti:sapphire laser (KMLabs Dragon), were split by a beam splitter into pump and probe beams. The pump beam excites the sample (i.e. it induces changes in the optical properties) whereas the probe beam interrogates the excited portion. The intensity of both, pump and probe beam was adjusted by a combination of $\lambda/2$ -waveplates and thin film polarizer. While the pump beam fluence could be adjusted from $60 \mu\text{J}\cdot\text{cm}^{-2}$ to $10 \text{mJ}\cdot\text{cm}^{-2}$, the probe fluence was kept very low (below $20 \mu\text{J}\cdot\text{cm}^{-2}$) with a diameter of about three times smaller than the pump in order to probe an homogeneously excited area. After reflection from the sample, the probe beam was detected by an amplified photodetector (Thorlabs DET 10A). The pump beam, on the other hand, was blocked in order to reduce any influence on the detector. In order to suppress the fluctuations of the laser intensity, another amplified photodetector (Thorlabs DET 10A) was installed to monitor a small fraction of the probe beam reflected by a beam sampler. Both detectors are coupled to lock-in amplifier (SR 830) in order to enhance the signal to noise ratio. To be able to measure the pump induced reflectivity changes as a function of time, Newport delay unit (M-IMS) was used.

In a pump-probe reflectivity (PPR) measurement it is necessary to compare the reflectivity of the sample in the condition of pumping and without pumping. To realize these states, an optical chopper was installed in the pump line which alternately blocks and lets pass a pump pulse, as shown in figure 3.4.

In order to enhance the sensitivity of the time-resolved reflectivity measurements, a technique proposed by P.Fauchet [57] was applied. By appropriately choosing the angle of incidence near Brewster's angle θ_{br} and probing with a P -polarized light, the photoinduced reflectivity changes are easily increased by one order of magnitude. This enhancement is due to the enhanced $\frac{\partial R}{\partial n}$ (as shown in figure 3.5) near θ_{br} . Therefore, the same modification on the index of refraction n by the photoexcitation produces larger ΔR near θ_{br} than at other angles.

3. ULTRAFAST DYNAMICS IN HIGHLY EXCITED CDTE: THE TIME-RESOLVED REFLECTIVITY MEASUREMENT

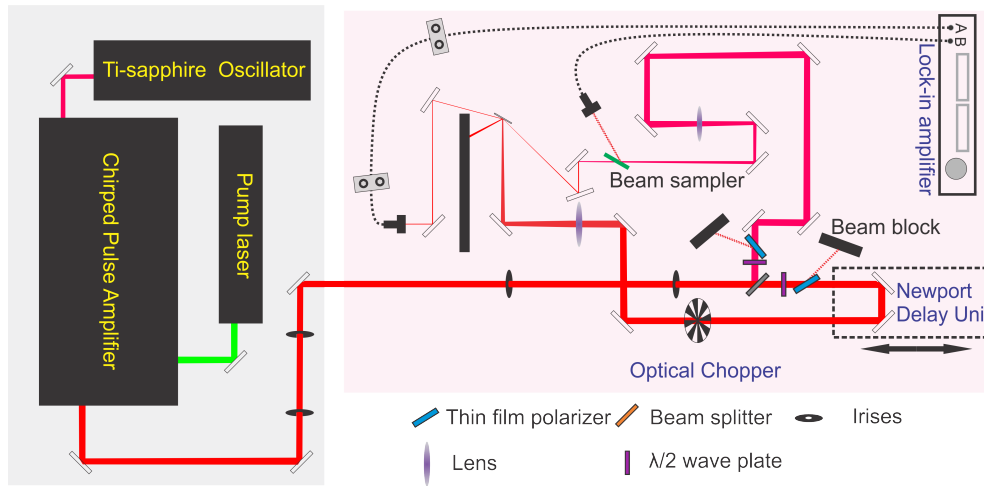


Figure 3.3: Optical pump-probe setup - Laser pathways are indicated in red and green color.

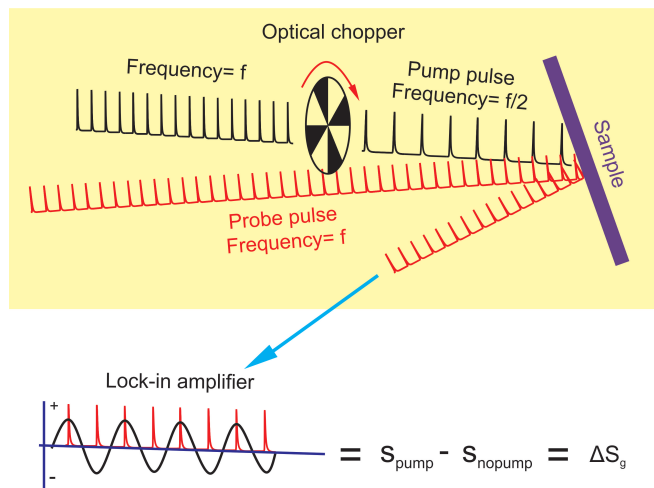


Figure 3.4: The operation principle of the Lock-in amplifier with an optical chopper - The lock-in amplifier is in phase with the chopper, thus the output signal ΔS_g is the reflection difference between two situations: 1. pumped S_{pump} , 2. unpumped S_{nopump} .

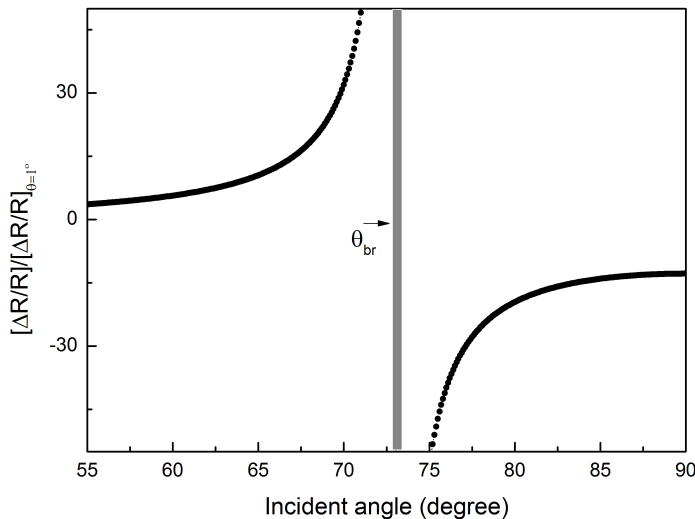


Figure 3.5: The enhancement of P-polarized light probing near the Brewster's angle θ_{br} . - Calculated by using Fresnel's formula as described in section 2.2.

3.3 Calculating the Optical Properties of the Laser-Excited CdTe

The time-resolved reflectivity technique probes the evolution of the optical properties of the material excited by the laser pulses. These properties are governed by the dynamics of the carriers and the lattice of the material. Therefore, to compute the reflectivity one needs to take into account (i) the effect of the carriers on the susceptibility of the material and, (ii) the dynamics of carriers and the lattice, as illustrated in the diagram shown in figure 3.6. In this section, computations of the effects summarized under (i) will be shown.

3.3.1 Optical Properties of a Hot Electron-Hole Plasma

The pump-probe reflectivity technique directly measures the reflectivity changes ΔR of the sample following the photoexcitation by a short laser pulse. The reflectivity is a function of the optical susceptibility $\chi(\omega)$, which represents the material response to the external perturbations and is determined by both, the carriers and the lattice together.

In semiconductors, if the laser-excited carrier density is below the Mott density [49],

3. ULTRAFAST DYNAMICS IN HIGHLY EXCITED CDTE: THE TIME-RESOLVED REFLECTIVITY MEASUREMENT

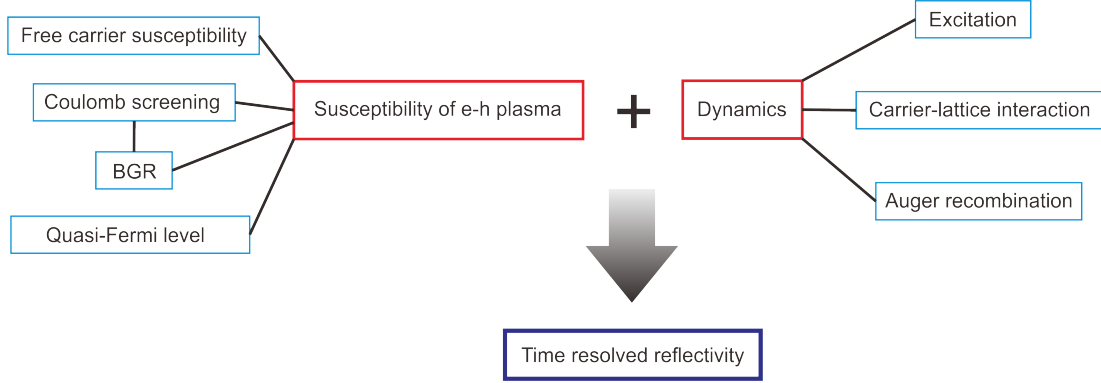


Figure 3.6: Scheme of the applied theoretical approach. - Left: the effect of the carriers on the susceptibility of the material (BGR: band gap renormalization). Right: the dynamics of the carriers and the lattice.

the cold electrons and holes tend to form a system called Wannier-Mott exciton [58]: a system similar to a hydrogen atom but with less binding energy (few tens of meV). Above the Mott density, the electric field screening sufficiently reduces the Coulomb interaction between electrons and holes so that it breaks excitons (the electron-hole pairs), hence forming a new state of matter, the electron-hole plasma. Both the Wannier-Mott exciton and the electron-hole plasma modify the energy band structures, affecting thus the optical properties of the semiconductor directly.

A. Quasi Fermi level

After photoexcitation, electrons and holes are populating at certain energy states (depending on the laser wavelength) in the conduction and valence bands, respectively. In this condition, the electron and hole system is displaced far from equilibrium. And, thus, can not be simply described by the Fermi distribution function. Moreover, the treatment of such a system is very complex, since all carrier momenta have to be considered. However, in situations where electrons and holes have already relaxed their excess energy (thermalized), they can be considered of forming Fermi distributions in their respective bands which are denoted as “quasi-Fermi levels” (the quasi Fermi level of electrons μ_e and the quasi Fermi level of holes μ_h , respectively). Under this special condition, the treatment does not need to consider all carrier momenta as they are in this case known to be Fermi distributions.

Via the quasi-equilibrium distribution, a quasi-Fermi level gives the probability that a particular state in the energy band is available or not. Thus, it describes the response of the bulk on the absorption of light by the carriers. A suppressed absorption

3.3 Calculating the Optical Properties of the Laser-Excited CdTe

is a direct consequence of the Pauli exclusion principle. Burstein [59] observed this for the first time in InSb, and since then it is referred to as Burstein-Moss effect but, more frequently it is called band filling effect (BF). The quasi-Fermi levels which govern the BF can be calculated by means of the well-known Nilsson's formulas [60]:

$$\mu_e(T) = \left\{ \ln \left(\frac{n}{n_e} \right) + \left(\frac{n}{n_e} \right) \left[64 + 0.05524 \left(\frac{n}{n_e} \right) \left(64 + \sqrt{\frac{n}{n_e}} \right) \right]^{-1/4} \right\} k_B T \quad (3.1)$$

$$\mu_h(T) = \left\{ \ln \left(\frac{n}{n_h} \right) + \left(\frac{n}{n_h} \right) \left[64 + 0.05524 \left(\frac{n}{n_h} \right) \left(64 + \sqrt{\frac{n}{n_h}} \right) \right]^{-1/4} \right\} k_B T \quad (3.2)$$

Where k_B is the Boltzmann constant, T is the temperature, $n_{e,h}$ are the effective density of states in the conduction and valence band defined as:

$$n_e = 2 \left(\frac{m_e k_B T}{2\pi \hbar^2} \right)^{3/2} \quad (3.3)$$

$$n_h = 2 \left(\frac{m_h k_B T}{2\pi \hbar^2} \right)^{3/2} \quad (3.4)$$

Figure 3.7 shows the calculated quasi-Fermi levels in the Γ valley of CdTe by using the Nilsson's formulas 3.1 and 3.2 (assuming both the electron and hole temperatures are 300 K).

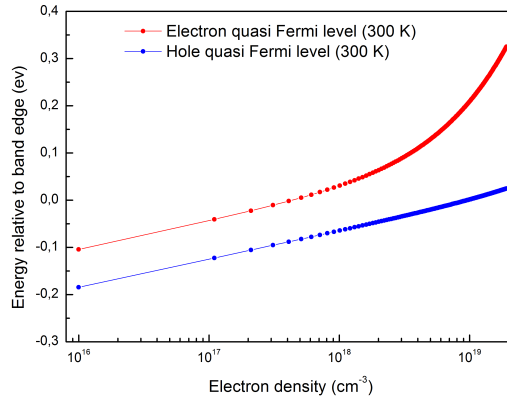


Figure 3.7: The quasi-Fermi level of CdTe in the Γ valley. - Quasi-Fermi levels as a function of the free carrier density at room temperature, computed using the equation 3.1 and 3.2.

The possibility of finding carriers in certain bands is described by the Fermi-Dirac distribution. For both electrons and holes, it can be calculated as:

$$f_{e,h}(\varepsilon) = \frac{1}{e^{(\varepsilon - \mu_{e,h})/k_B T} + 1} \quad (3.5)$$

3. ULTRAFAST DYNAMICS IN HIGHLY EXCITED CDTE: THE TIME-RESOLVED REFLECTIVITY MEASUREMENT

Where ε is the Fermi energy, which value is equal to the quasi-Fermi level at 0 K.

B. Coulomb Screening and Band Gap Renormalization

The high carrier concentration induces strong screening on the Coulomb interactions, which is characterized by the screening length $\lambda_{e,h}$. In this section, the screening length $\lambda_{e,h}$ and the band gap normalization (BGR) in CdTe will be calculated.

The screening length is given by:

$$\lambda_e = \sqrt{\frac{\varepsilon_0 \varepsilon_r}{e^2} \frac{\partial \mu_e}{\partial n}} \quad (3.6)$$

$$\lambda_h = \sqrt{\frac{\varepsilon_0 \varepsilon_r}{e^2} \frac{\partial \mu_h}{\partial n}} \quad (3.7)$$

Where ε_0 is the static dielectric constant and ε_r is the relative dielectric constant. The expression of $\frac{\partial \mu_{e,h}}{\partial n}$ can be obtained from 3.1 and 3.2.

The total screening length is given by:

$$\lambda_s = \sqrt{\frac{\lambda_e^2 \lambda_h^2}{\lambda_e^2 + \lambda_h^2}} \quad (3.8)$$

Based on the calculation of the screening length, one can calculate the band gap renormalization (BGR) by a phenomenological formula proposed by Bańyai and Koch [61]:

$$E_g = E_0 - E_{ex} + E_s \quad (3.9)$$

if the density of carriers is lower than the ‘‘Mott’’ density (N_{mott}), or

$$E_g = E_{g,0} - \frac{E_{ex} a_{ex}}{\lambda_s} \quad (3.10)$$

if the density of carrier is higher than the ‘‘Mott’’ density.

Where $E_{g,0}$ is the the band gap, E_g is the renormalized band gap, a_{ex} is the Bohr radius of the exciton, λ_s is the screening length and E_{ex} is exciton binding energy given by:

$$E_0 = \frac{\hbar^2}{2m_r a_{ex}} \quad (3.11)$$

E_s is the screened exciton binding energy given by:

$$E_s \begin{cases} (1 - a_{ex}/\lambda_s)^2 E_0 & \text{If } \lambda_s > a_{ex}, \\ 0 & \text{if } \lambda_s < a_{ex}. \end{cases}$$

3.3 Calculating the Optical Properties of the Laser-Excited CdTe

The calculated BGR of CdTe by using equations 3.9 and 3.10 are shown in figure 3.8. It is evident that the BGR function is not continuous at the point N_{mott} . This indicates a noncontinuous PPR curve when the density of carriers crosses the Mott density N_{mott} from either above or below. In fact, this discontinuity has never been observed [62]. The continuity of PPR curve can be fulfilled if one takes equation 3.10 as an approximation for both above and below N_{mott} for CdTe at room temperature (red curve in figure 3.8).

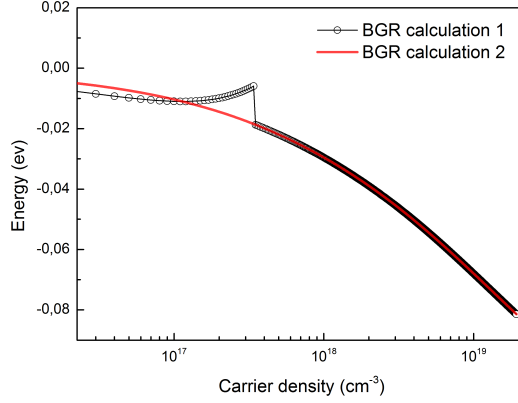


Figure 3.8: Band-gap renormalization in CdTe (Γ valley). - Data indicated by the black balls is calculated using both formulas 3.9 and 3.10, and while the red line is calculated using the formula 3.10 based on the discussion in the text.

C. The Optical Susceptibility

The peculiar difference in the behavior of the PPR measurement can not be understood within the simple Drude model. Moreover, it requires to take multiple physical processes into account. An advanced model for calculating such a reflectivity of the sample under intense laser irradiation was proposed by H.Haug [63].

The susceptibility function is given by:

$$\chi_k(\omega) = \chi_k^0 \left(1 + \frac{1}{d_{cv} L^3} \sum_{k'} V_{s,|k-k'|} \chi_{k'}(\omega) \right) \quad (3.12)$$

Here d_{cv} is the dipole moment of the valence conduction-band transition, L^3 is the volume of the cubic crystal, χ_k^0 is the free carrier susceptibility which is given by:

$$\chi_k^0(\omega) = -d_{cv} \frac{1 - f_{k,e} - f_{k,h}}{\hbar [\omega + i\gamma(\omega)] - \epsilon_{k,e} - \epsilon_{k,h} - E_g} \quad (3.13)$$

3. ULTRAFAST DYNAMICS IN HIGHLY EXCITED CDTE: THE TIME-RESOLVED REFLECTIVITY MEASUREMENT

and $V_{s,|k-k'|}$ is the screened Coulomb potential in momentum space given by:

$$V_{s,|k-k'|} = \frac{e^2}{\epsilon_0 \epsilon_r} \frac{1}{k^2 + k'^2 - 2kk' \cos \varphi + \lambda_s^{-2}} \quad (3.14)$$

The calculation of the screened Coulomb potential requires the knowledge about the angles (φ) between every carrier's momentum, which is unrealistic. However, because of the rotation symmetry, the screened Coulomb potential can be replaced by the angle averaged Coulomb potential as follow:

$$\bar{V}_{s,k,k'} = \frac{e^2}{4\epsilon_0 \epsilon_r k k'} \text{Ln} \frac{(k^2 + k'^2 + 2kk' \lambda_s^2) + 1}{(k^2 + k'^2 - 2kk' \lambda_s^2) + 1} \quad (3.15)$$

The susceptibility integral equation can be solved approximately by inserting a dominate momentum, which could be considered to be the momentum close to the quasi-Fermi level, where the optical properties are strongly affected. The susceptibility integral equation then becomes:

$$\chi_k(\omega) = \chi_k^0(\omega) \left[1 + \frac{1}{d_{cv} L^3} \sum_{k'} \bar{V}_{s,k_f,k'} \chi_{k'}(\omega) \right] \quad (3.16)$$

$$\chi_k(\omega) = \chi_k^0(\omega) [1 + g(\omega)] \quad (3.17)$$

$$g(\omega) = \frac{1}{d_{cv} L^3} \sum_{k'} \chi_k^0 \bar{V}_{s,k_f,k'} [1 + g(\omega)] \quad (3.18)$$

Using k instead of k'

$$g(\omega) = \frac{1}{d_{cv} L^3} \sum_k \chi_k^0 \bar{V}_{s,k_f,k} [1 + g(\omega)] \quad (3.19)$$

This equation yields:

$$1 + g(\omega) = \frac{1}{1 - \frac{1}{d_{cv} L^3} \sum_k \chi_k^0 \bar{V}_{s,k_f,k}} \quad (3.20)$$

Bring equation 3.20 into equation 3.17, one gets:

$$\chi_k(\omega) = \frac{\chi_k^0(\omega)}{1 - \frac{1}{d_{cv} L^3} \sum_k \chi_k^0 \bar{V}_{s,k_f,k}} \quad (3.21)$$

3.3 Calculating the Optical Properties of the Laser-Excited CdTe

Table 3.1: Model parameters

Parameter	value
χ_l	5.4
d_{cv}	$8.82 \times 10^{-29} \text{ C} \cdot \text{m}$
k_{max}	$2.2 \times 10^9 \text{ m}^{-1}$
γ_0	0.3 eV
E_α	0.04 eV

The total susceptibility is:

$$\chi_k(\omega) = \chi_l + \frac{2d_{cv}}{\epsilon_0 L^3} \frac{\chi_k^0(\omega)}{1 - \frac{1}{d_{cv} L^3} \sum \chi_k^0 \bar{V}_{s,k_f,k}} \quad (3.22)$$

with χ_l being some background susceptibility (related to the lattice response).

In calculations of the susceptibility, a frequency dependent damping coefficient $\gamma(\omega)$ is shown to be better than a constant damping rate, i.e., a formula described by H.Haug [63] and V.Marijn [64]:

$$\gamma(\omega) = \frac{\gamma_0}{e^{(E_g - \hbar\omega - E_\alpha)/E_\alpha} + 1} \quad (3.23)$$

Various model parameters involved in equation 3.23 (listed in table 3.1) can be estimated by comparing the $\chi(\omega)$ with published dielectric function data [65].

The simulations of the dielectric functions are shown in figure 3.9, ϵ_1 is equal to the real part of $1 + \chi(\omega)$, and ϵ_2 is equal to the imaginary part of $1 + \chi(\omega)$.

Independently, the response of CdTe to long wavelength radiation (photo energy smaller than the fundamental energy gap) is very well described by a parameterized function [66]. With the parameters listed in table 3.1, the simulation is comparable with the parameterized function, (see the figure 3.10). This is another indication that the simulation is successful.

By utilizing the function $\chi(\omega)$ and taking experimental inputs such as the angle of incidence θ , one can compute the reflectivity by Fresnel's formula described in section 2.2.

D. Electro-Optic Effect

An additional reflectivity change due to the modification of the space-charge field is not included in the above consideration. This contribution can be added in terms of

3. ULTRAFAST DYNAMICS IN HIGHLY EXCITED CDTE: THE TIME-RESOLVED REFLECTIVITY MEASUREMENT

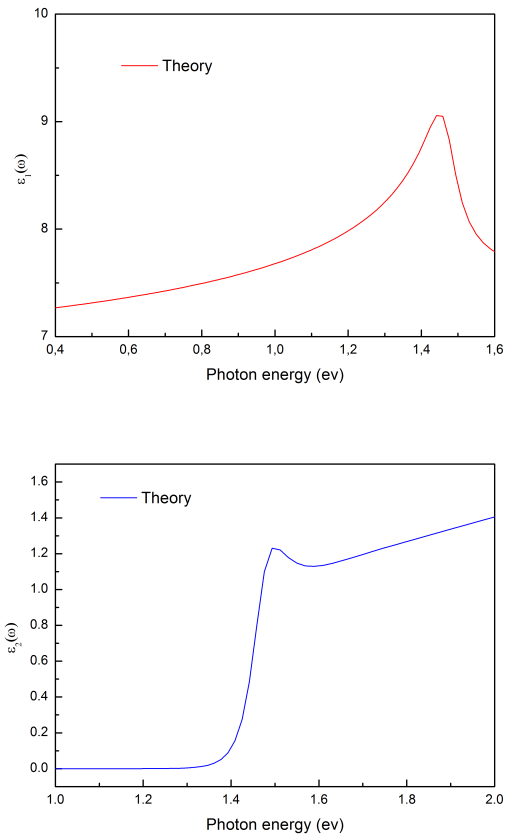


Figure 3.9: ϵ_1 and ϵ_2 are real and imaginary part of the dielectric function, respectively.

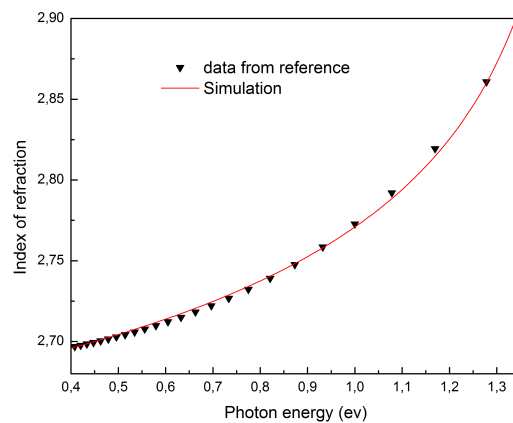


Figure 3.10: The comparison between the simulation and the parameterized function. - The red line is the simulation, and the black triangles are the values calculated from the parameterized function described in [66].

3.4 Time-Resolved Reflectivity Measurement and Discussion

the electro-optical effect. This effect is defined as a linear change in the refractive index caused by an electric field $\Delta n \propto \Delta E$. Since the lattice vibration is consonance with the surface electric field which affects the index ellipsoid, the information about the lattice vibration can be obtained by measuring the reflectivity changes. For a zinc-blende type crystal with surface orientation (111), the effect is given by [67]:

$$\frac{x^2 + y^2 + z^2}{n_0^2} + \frac{2}{\sqrt{3}}\gamma_{41}E(yz + xy + zx) = 1 \quad (3.24)$$

Three new components of refraction index are:

$$n'_x = n_0 + \frac{1}{2\sqrt{3}}n_0^3\gamma_{41}E \quad (3.25)$$

$$n'_y = n_0 + \frac{1}{2\sqrt{3}}n_0^3\gamma_{41}E \quad (3.26)$$

$$n'_z = n_0 - \frac{1}{\sqrt{3}}n_0^3\gamma_{41}E \quad (3.27)$$

3.4 Time-Resolved Reflectivity Measurement and Discussion

3.4.1 Longitudinal-Optical Phonon-Plasmon Coupled Modes

The longitudinal optical phonon generation in polar semiconductors is due to the ultra-fast screening of the surface charge region [12, 68, 69] by the photoexcited free carriers. However, the electric field of the surface charge region is usually weak. Therefore the amplitude of the lattice oscillations are small. In order to enhance the surface electric field [68], a CdTe single crystal doped with 5×10^{16} lithium atoms is used, which subsequently increases the amplitude of lattice oscillations (For a nominal doping density of $5 \times 10^{16} \text{ cm}^{-3}$, a surface space charge field of $\sim 90 \text{ kV}\cdot\text{cm}^{-1}$ is expected).

In the first part of the experiment, the evolution of the sample reflectivity as a function of the pump-probe delay was measured at laser fluences of $0.064 \text{ mJ}\cdot\text{cm}^{-2}$ and $0.57 \text{ mJ}\cdot\text{cm}^{-2}$ (hereafter, low-fluence regime). A typical PPR curve measured at low fluence is shown in figure 3.11. The reflectivity transient is composed of a small oscillation signal superimposed on the large background. The background (i.e. the large exponential-like change of the time dependent reflectivity) is due to the changes of the carrier occupancy in the conduction and valence bands. It is mainly determined by the evolution of the quasi-Fermi level described in the section 3.3.1. The small signal oscillations superimposed on the large-scale transient originate from the electro-optic effect, thus encode the time evolution of the surface electric field (i.e. the dynamics

3. ULTRAFAST DYNAMICS IN HIGHLY EXCITED CDTE: THE TIME-RESOLVED REFLECTIVITY MEASUREMENT

of the longitudinal optical phonon-plasmon coupled modes (LOPC)). In order to extract this oscillation signal, which is about two orders of magnitude smaller than the background, a Savitzky-Golay filtering method is applied. This method is common for these types of measurements and was successfully applied to investigate LOPC modes in GaAs [70]. Here, according to the recipe given in [70], one first filters the measured signal, then, the oscillations are yielded by subtracting the PPR signal from the filtered one. In order to prevent numerical artifacts, the filtering interval was chosen to begin well to the right of the sharp minimum of the recorded PPR signal.

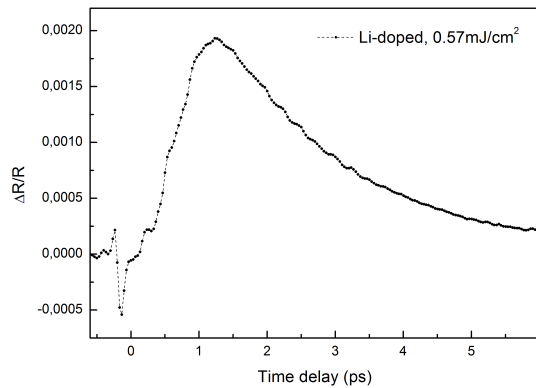


Figure 3.11: A typical low pump fluence PPR curve. - The oscillations are superimposed on the large background. Fluctuations before time zero are due to the interference between the pump and probe beam, even through they are already suppressed by setting the polarization between pump and probe beam to be orthogonal.

Coherent oscillations of the time-resolved PPR signal are shown in figures 3.12, the mode beating and damping which are due to the phonon-plasmon dynamics are clearly visible. In order to identify the modes and compare their lifetimes, a wavelet transform (which can be recognized as a time-resolved Fourier transform [53]) of the oscillations is made.

From the wavelet transform of the oscillations measured at $0.064 \text{ mJ}\cdot\text{cm}^{-2}$ (figure 3.13), one can see clearly a major feature located at $\sim 5\text{THz}$ that can be safely labeled as the LO phonon frequency of the CdTe (the phonon dispersion relation was shown in figure 2.2). In addition to this, one observes the LOPC mode formation within first few hundred femtoseconds following laser excitation and their decay later. The higher branch of the LOPC mode is called L^+ mode. It is of a plasmon character having larger frequency than the LO phonon mode whereas the low branch of LOPC is called L^-

3.4 Time-Resolved Reflectivity Measurement and Discussion

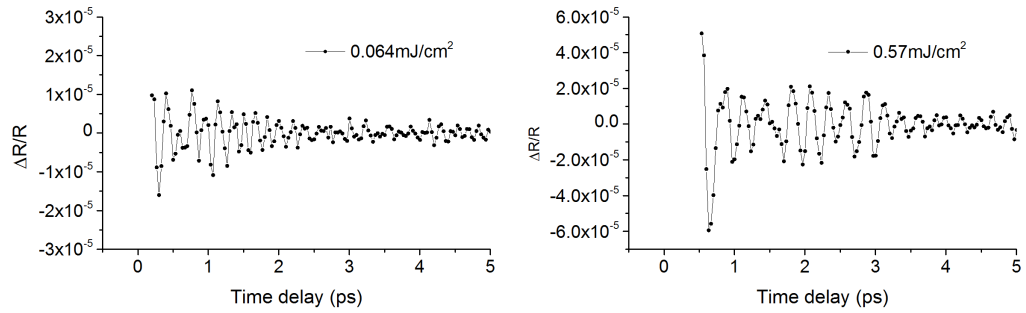


Figure 3.12: The comparison of the coherent oscillations at fluence $0.064 \text{ mJ}\cdot\text{cm}^{-2}$ and at $0.57 \text{ mJ}\cdot\text{cm}^{-2}$. In order to avoid the coherent artifact [1] near to time zero, oscillations are extracted after that.

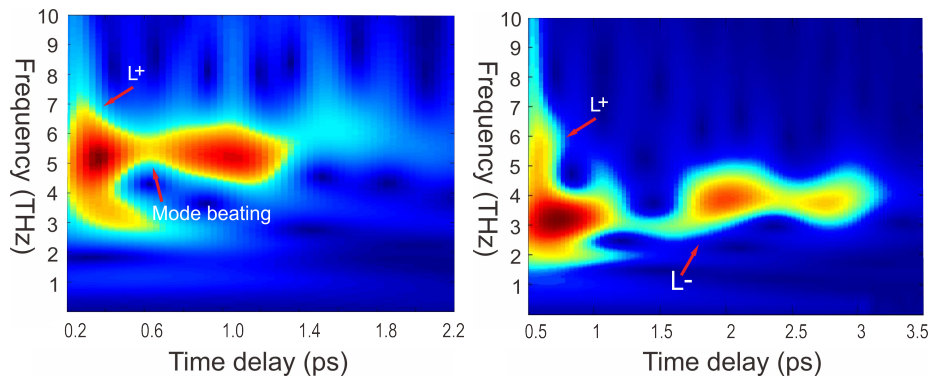


Figure 3.13: The wavelet transforms of the oscillations measured at the pump fluences of 0.064 and $0.57 \text{ mJ}\cdot\text{cm}^{-2}$.

3. ULTRAFAST DYNAMICS IN HIGHLY EXCITED CDTE: THE TIME-RESOLVED REFLECTIVITY MEASUREMENT

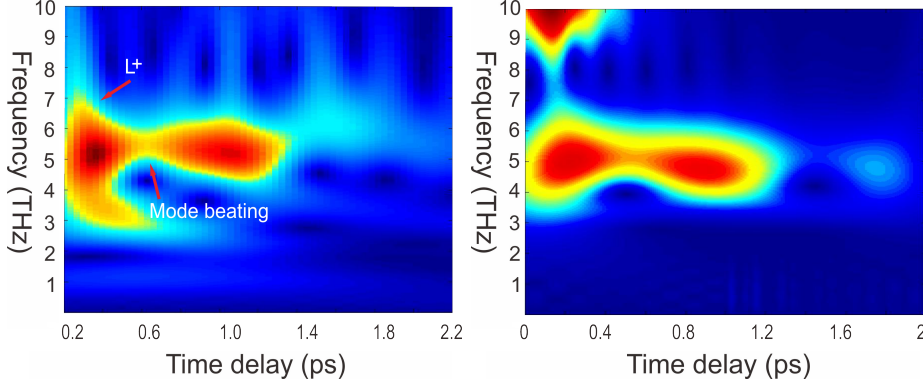


Figure 3.14: The left image shows the experimental measurement, the right image shows the simulation. L^+ is shown in the measurement, mode beating between the L^- and LO mode, decay of the mixed mode is observed.

mode and is of phonon character. However, due to the time resolution limitation in this measurement (mainly limited by the laser pulse duration of ~ 60 fs), only the low frequency tail of the damped L^+ mode is observed (it is shown more clearly at a higher fluence $0.57 \text{ mJ}\cdot\text{cm}^{-2}$ measurement). The L^- mode, on the other hand is red-shifted and reduced (in particular due to the fact that the carrier density is reduced). This is in agreement with the theory presented section 2.3. However, a component at ~ 5 THz which corresponds to the LO phonon mode is observed as well. According to the LOPC framework presented in chapter 2, this mode should not appear. The reason why it is observed can be attributed to the non-uniform carrier density under the probe penetration region. It is known that the carrier density is decaying with the depth and time very fast. In fact, the LOPC is present only in a narrow area close to the surface where the density of carriers is large, whereas the LO phonon mode is present in the bulk region where the carrier density is much lower. Since the penetration depth of the probe beam covers both regions, both modes are observed [15]. By taking this fact into consideration, a simulation with the parameters listed in table 3.2 is compared with the measurement represented as the wavelet transform spectrum, see the figure 3.14. It is obvious that the simulations predict mode beating, damping and the frequency shift with carrier density. The high frequency part of the L^+ mode cannot be captured by the experiment due to the lack of time resolution.

At higher fluence ($0.57 \text{ mJ}\cdot\text{cm}^{-2}$), the single-photon absorption is already saturated, which means the carrier density in the whole probe penetration region stays higher than $1 \times 10^{18} \text{ cm}^{-3}$, as shown in figure 3.15 (left). Under this condition, the lower branch of the LOPC is expected to have a frequency of ~ 4 THz, and the LO mode should

3.4 Time-Resolved Reflectivity Measurement and Discussion

Table 3.2: Simulation parameters

Parameter	Value
Maximum electron density	$10^{18} \cdot \text{cm}^{-3}$
Surface electric field	$20 \text{ kV} \cdot \text{cm}^{-1}$
Electron-hole recombination time	1.5 ps
Electric field of the LO mode	$4 \text{ kV} \cdot \text{cm}^{-1}$
LO phonon decay time	1.2 ps

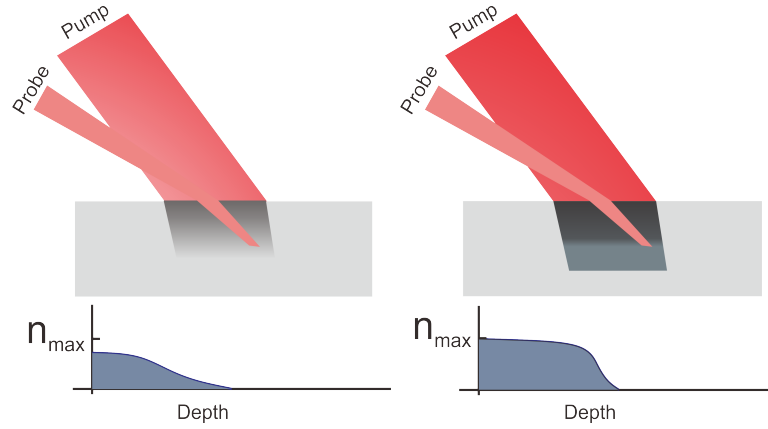


Figure 3.15: Carrier density, left: at lower fluence, carrier generated by SPA, right: at higher fluence, the SPA is already saturated. n_{max} is the maximum carrier density that can be generated by SPA.

disappear. This is exactly the case in the measurement, as depicted in figure 3.12. Apart from the time resolution, there is another effect affecting the measurement of the LOPC modes. Since carriers are excited to different parts of the conduction band (the Γ valley and the L valley), they have different effective masses and densities. As a result, they do not oscillate at the same frequency according to the plasma frequency $f = \sqrt{\frac{n^2 e}{m^* \epsilon_0}}$, but rather at a mixture of these frequencies, which broadens then the frequency profiles of the LOPC mode.

3.4.2 CdTe under High Laser Excitation

In this section, the effects of hot carrier dynamics on the time-resolved reflectivity signal at high fluences ranging from 1.51 to $6.14 \text{ mJ} \cdot \text{cm}^{-2}$ are described. Hereafter, the high-excitation regime is reached with laser pulses above $1 \text{ mJ} \cdot \text{cm}^{-2}$. Excitation with fluence below $1 \text{ mJ} \cdot \text{cm}^{-2}$ is considered as low-excitation regime.

3. ULTRAFAST DYNAMICS IN HIGHLY EXCITED CDTE: THE TIME-RESOLVED REFLECTIVITY MEASUREMENT

Figure 3.16 compares time-resolved reflectivity curves measured at $0.44 \text{ mJ}\cdot\text{cm}^{-2}$ with these measured at high fluences and fluence-dependent effects are evident. First, following photoexcitation the reflectivity increases with time for the low fluence measurement ($0.44 \text{ mJ}\cdot\text{cm}^{-2}$) whereas it decrease with time for the high-fluences measurements (from 1.51 to $6.14 \text{ mJ}\cdot\text{cm}^{-2}$). Additionally, the value of the reflectivity minimum (valley) increase with increasing fluence.

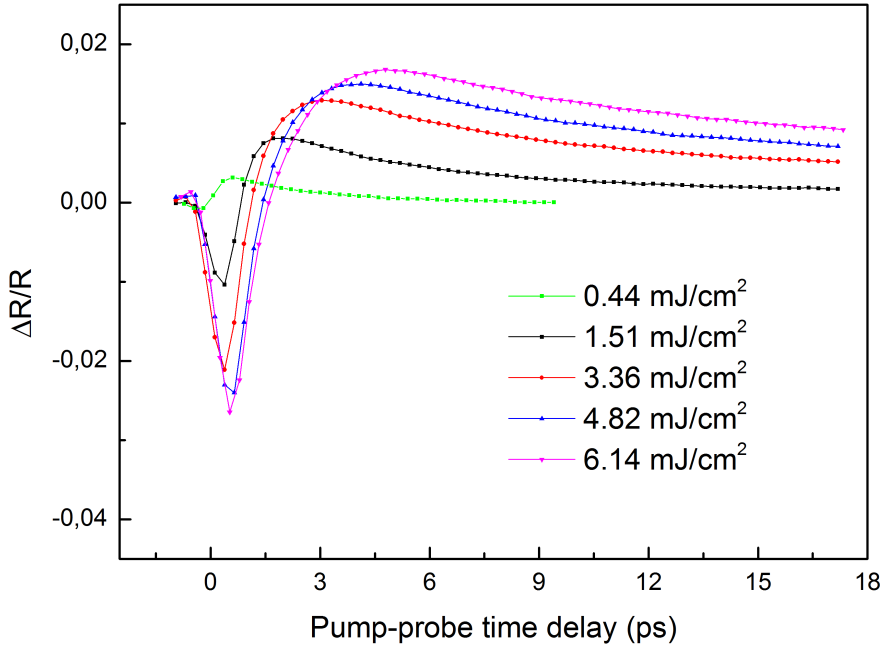


Figure 3.16: The time-resolved reflectivity measurement of the lithium-doped CdTe. - Fluences ranging from $0.44 \text{ mJ}\cdot\text{cm}^{-2}$ until $6.14 \text{ mJ}\cdot\text{cm}^{-2}$ are depicted.

The explanation of the reflectivity reduction following photoexcitation usually involves the band gap renormalization (BGR) effect [62, 71, 72] which is a many-body effect where the band gap decreases monotonically with the electron-hole plasma (EHP) density. The physical origin is the exchange energy of the EHP which originates from the Pauli principle which forbids two electrons with parallel spins being in the same unit cell. This exchange energy increases the average distance between the electrons which, subsequently lowers the energy of the electronic system.

To explain the observed effects one first consider the interplay of the band filling and BGR presented in section 3.3.1., as schematically shown in figure 3.17. At the

3.4 Time-Resolved Reflectivity Measurement and Discussion

lower fluence, the main photon absorption mechanism is single-photon absorption (SPA) which excites electrons near the Γ valley, these carriers redistributed very fast (few tens of fs) and fill the states in the conduction band which blocks the absorption of the probe pulse. As a result, the probe pulse will be reflected. In addition, cooling down of the hot electrons generated by two-photon absorption (TPA) prolongs the increasing of the reflectivity for few hundred fs (green curve in figure 3.16).

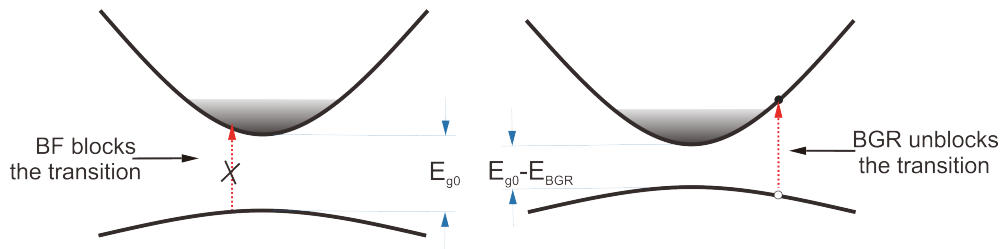


Figure 3.17: Interplay between BF and BGR affecting the probe beam reflectivity. - When BF is dominant, the absorption is suppressed due to the Pauli exclusion principle, when the BGR becomes dominant, the absorption is enhanced, E_{g0} is the band gap in Γ valley in the equilibrium state.

In the higher fluence regime, the electrons will be generated by both SPA and TPA. The TPA will excite electrons with higher excess energies, 1.84 eV, 2.5 eV and 2.9 eV with respect to the valence band minimum, respectively. The BF is affected only by the thermalized carriers near the band gap whereas the BGR depends on the total carrier density in the bands [62, 71]. Under this condition, following the laser excitation, only a fraction of the total carriers cool down to the band edge and affecting the BF, whereas all of them will contribute to BGR. That means, the BGR will be dominant with respect to BF. Since the BGR red shifts the energy band gap, i.e., it reduces the band gap to $E_g - \Delta E_{bgr}$, thus unblocking the probe beam as shown in figure 3.17. The net effect is the decrease of the time-dependent reflectivity.

In order to extract a physical interpretation from the data presented in figure 3.16, one needs to rely on the theoretical foundations presented in section 3.3.1 and extend the Stanton-Bailey model [48] (this model has been successfully applied to investigate the mobility of electrons in GaAs and InSb) to include photoexcitation (both SPA and TPA), recombination and the dynamics of the valence band hole (see the figure 3.18).

Based on this framework, the results are explained along the following key points:

3. ULTRAFAST DYNAMICS IN HIGHLY EXCITED CDTE: THE TIME-RESOLVED REFLECTIVITY MEASUREMENT

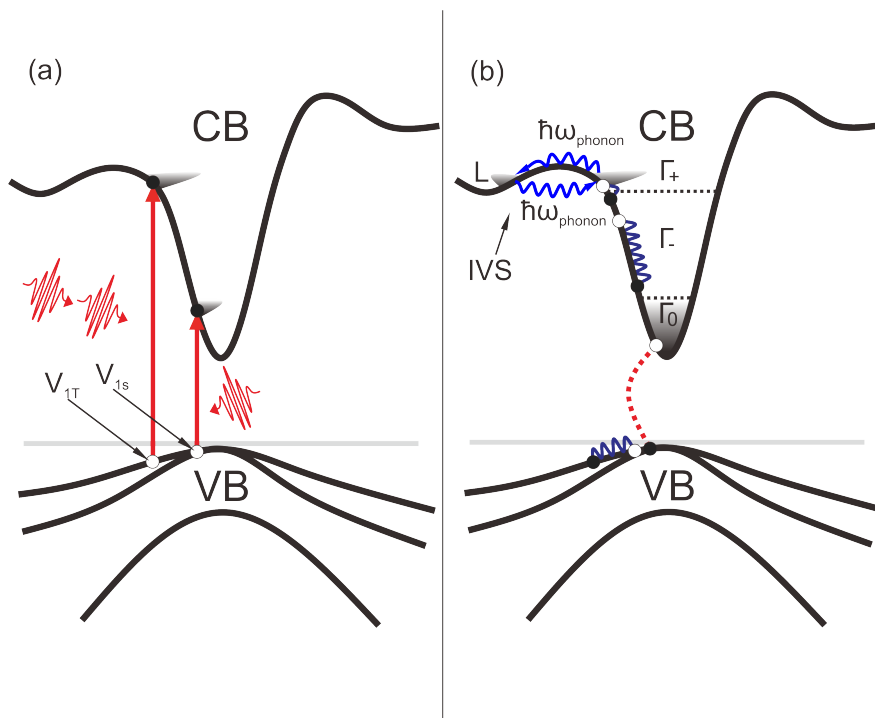


Figure 3.18: The excitation and carrier dynamics in CdTe. - (a) photoexcitation: SPA generates electrons near the edge of the conduction band, whereas TPA generates electrons near the L valley, V_{1s} and V_{1T} are the corresponding hole positions. (b) carrier relaxation and recombination: intervalley phonon scattering (IVS) transfers electrons from one valley to another, carrier-lattice interaction removes the excess energies of hot electrons and holes (i.e. they cool down by relaxing towards the band minimum), finally, the recombination process then reduces carriers in both, the conduction and valence band (dotted red line).

3.4 Time-Resolved Reflectivity Measurement and Discussion

(i) Photonexcitaion:

Single-photon absorption (SPA) excites electrons into the energy band Γ_0 . Within the laser spectra range it contains N_{max}^s available states. Thus, the laser pulse of intensity $I(t)$ can excite no more than N_{max}^s electrons into this band [43]. This fact is described by a term $\alpha \frac{N_{max}^s - N}{N_{max}^s}$ (SPA saturation). TPA on other hand involves large excitation energies and, thus, excites the carriers into the Γ_+ band. To the best of my knowledge, there is no direct measurement of TPA coefficient β carried out at 780 nm. But in general, TPA is intensity dependent. This dependence can be taken into account by using an effective TPA coefficient β_{eff} .

(ii) Carrier Cooling:

Electrons excited at the Γ_+ band will partially scatter to (i) the L valley (intervalley scattering) and (ii) to the Γ_- band. The number of scattered electrons to the L valley or to the Γ_- band depend on the scattering rates $\gamma_{\Gamma L}$ and γ_{rel} . The cooling rate γ_{rel} describes the speed of cooling carriers down to the band edge and, thus, determines the extend to which BF will overcome BGR. In the low excitation regime, γ_{rel} is attributed to the polar optical-phonon emission via the Fröhlich interaction. The typical scattering time is ~ 200 fs. If one takes this value and takes into account the fact that an electron at Γ_+ needs to relax ~ 1.4 eV of energy to reach the bottom of the conduction band, one can estimate the total cooling time: $\frac{1.4eV}{E_{LO}=0.026eV} \times 200fs = \sim 11$ ps. This would subsequently cause a much slower increase of the reflectivity from the valley minimum of the time-dependent reflectivity curve. And, thus, is in contradiction with the experimentally measured time-resolved signal. Therefore, there must be a relaxation channel of hot carriers which is much faster than LO phonon emission. Since CdTe is a polar semiconductor with strong coupling between LO phonon and plasmons (see the section 2.3), the fast channel can be safely attributed to energy relaxation by the LOPC modes. This channel was used to interpret the ultrafast increase of the reflectivity in another polar semiconductor, CdS [73]. Accordingly, by interacting with the hybrid phonon-plasmon modes, hot carriers can relax much more efficiently within a time scale of about 500 fs.

(iii) Carrier Recombination:

When electrons and holes are cooling down towards the band edge, they start to recombine with each other. In CdTe, the radiative recombination coefficient is only $3 \pm 0.5 \times 10^{-9} \text{ cm}^3 \cdot \text{s}^{-1}$ [74]. At a density of 10^{18} cm^{-3} , the recombination continues

3. ULTRAFAST DYNAMICS IN HIGHLY EXCITED CDTE: THE TIME-RESOLVED REFLECTIVITY MEASUREMENT

for several ns. However, in this measurements, the recombination is observed only for few ps to few tens of ps. Therefore, the fast process must be attributed to the much more efficient Auger recombination. A typical Auger recombination process involves three carriers, and is therefore proportional to N^3 , where N is the free carrier density. In degenerated semiconductors, however, an Auger recombination rate with a quadratic dependence on carrier density N^2 has been found to better describe the experimental data [75, 76, 77].

According to the discussion above, the Stanton-Bailey model is extended as:

$$\frac{dN_{\Gamma_+}}{dt} = \frac{\beta_{eff}I(t)^2}{2\hbar\omega} - \gamma_{\Gamma L}N_{\Gamma_+} + \gamma_{L\Gamma}N_{\Gamma_+} - \gamma_{rel}N_{\Gamma_+} \quad (3.28)$$

$$\frac{dN_L}{dt} = \gamma_{\Gamma L}N_{\Gamma_+} - \gamma_{L\Gamma}N_L \quad (3.29)$$

$$\frac{dN_{\Gamma_-}}{dt} = \gamma_{rel}N_{\Gamma_+} - \gamma_{cool}N_{\Gamma_-} \quad (3.30)$$

$$\frac{dN_{\Gamma_0}}{dt} = \alpha\left(\frac{N_{max}^s - N_{\Gamma_0}}{N_{max}^s}\right)\frac{I(t)}{\hbar\omega} + \gamma_{cool}N_{\Gamma_-} - R_{aug}N_{\Gamma_0}^2 \quad (3.31)$$

$$\frac{dN_{V_{1T}}}{dt} = \frac{\beta_{eff}I(t)^2}{2\hbar\omega} - \gamma_{hcool}N_{v_1} \quad (3.32)$$

$$\frac{dN_{V_{1s}}}{dt} = \alpha\left(\frac{N_{max}^s - N_{\Gamma_0}}{N_{max}^s}\right)\frac{I(t)}{\hbar\omega} + \gamma_{hcool}N_{v_1} - R_{aug}N_{\Gamma_0}^2 \quad (3.33)$$

$$I = \frac{f}{\sqrt{2\pi}d}e^{-t^2/2d^2} \quad (3.34)$$

The subscript of the carrier densities N represent their position in bands, which are Γ_+ , Γ_- , Γ_0 , V_{1s} and V_{1T} . They are discussed in section 2.3 in Chapter 2, γ_{cool} and γ_{hcool} are the effective cooling rate of the electrons and holes, respectively. R_{aug} is the degenerate Auger recombination coefficient. v_{1T} and v_{1s} are the positions on the valence band where TPA and SPA happen (see the figure 3.18).

By computing the carrier density using the extended Stanton-Bailey model, combined with the susceptibility calculated in section 3.22, one can simulate the time-dependent reflectivity curves and compare them with the experimental findings. Figure 3.20 shows the comparison between simulation and experiment. The parameters used in the simulation are listed in table 3.3.

From the simulation, one finds that both, the effective cooling rates of electrons and holes are increasing with increasing the pump fluence, whereas the degenerated Auger recombination coefficient is decreasing. Both behaviors are visible in figure 3.19. In fact, these phenomena are caused by the Coulomb screening. In both cases, the increased screening reduces the scattering cross section between carriers, thus slows

3.4 Time-Resolved Reflectivity Measurement and Discussion

Table 3.3: Model parameters

Parameter	Unit				
Fluence (f)	$\text{mJ}\cdot\text{cm}^{-2}$	1.51	3.36	4.82	6.14
α	cm^{-1}	1×10^4	1×10^4	1×10^4	1×10^4
N_{max}^s	cm^{-3}	10^{18}	10^{18}	10^{18}	10^{18}
β_{eff}	$\text{cm} \cdot \text{GW}^{-1}$	55	26	17	11
γ_{gl}	fs^{-1}	300	300	300	300
γ_{lg}	fs^{-1}	2000	2000	2000	2000
γ_{pop}	fs^{-1}	20	20	20	20
γ_{cool}	fs^{-1}	500	520	550	600
γ_{hcool}	fs^{-1}	100	120	150	200
R_{aug}	$\text{cm}^3 \cdot \text{s}^{-1}$	2×10^{-6}	1.5×10^{-6}	1.2×10^{-6}	1×10^{-6}

down the thermalization and the Auger recombination [13].

A slight difference between the simulation and the measured time-dependent reflectivity curve is evident at large pump-probe delays, especially at the lower fluence $1.51 \text{ mJ}\cdot\text{cm}^{-2}$ (see the figure 3.20). One can clearly attribute this to the constant R_{aug} used in the simulation. For example, in time-dependent reflectivity curve measured at fluence of $1.51 \text{ mJ}\cdot\text{cm}^{-2}$, by using a recombination coefficient of $3 \times 10^{-6} \text{ cm}^3 \cdot \text{s}^{-1}$ below a certain critical density ($3.5 \times 10^{17} \text{ cm}^{-3}$) and $2 \times 10^{-6} \text{ cm}^3 \cdot \text{s}^{-1}$ above, the simulation now fits the measurement very well (figure 3.21). This goes along with the Coulomb screening effect which decreases the scattering cross section between the carriers.

Another parameter obtained from the simulation is the effective TPA coefficient at each fluence (see the figure 3.22). An obvious decline of the TPA coefficient is observed, which indicates TPA saturation. Unlike other TPA saturation models mentioned in [73, 78], the measured data is found to fit the TPA saturation model proposed by [79] very well. Here, the effective TPA coefficient is given by:

$$\beta_{effective} = \frac{\beta_0}{1 + I^2/I_{sat}^2} \quad (3.35)$$

In general, based on the simulations presented, one can conclude that the magnitude and signature of the PPR signal at different delays is governed by an interplay between the BGR and BF effects. The BGR and BF effects are further determined by the distribution, cooling, scattering, and recombination of the carriers.

3. ULTRAFAST DYNAMICS IN HIGHLY EXCITED CDTE: THE TIME-RESOLVED REFLECTIVITY MEASUREMENT

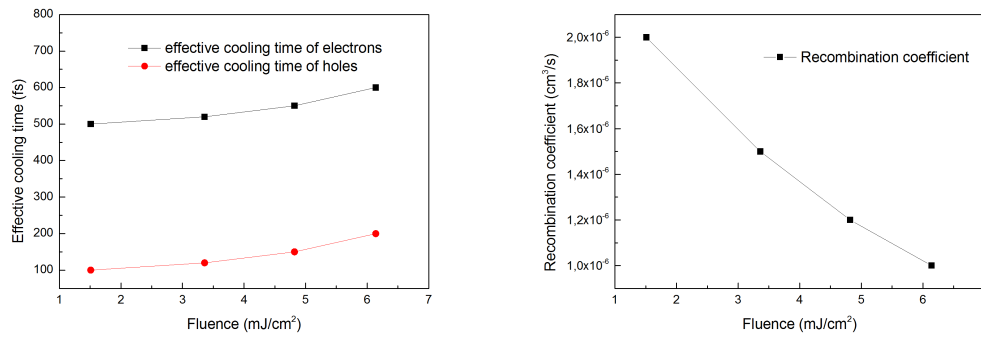


Figure 3.19: The effective cooling time and recombination coefficient versus fluence. - The effective cooling time increases with the excitation fluence whereas the recombination decreases.

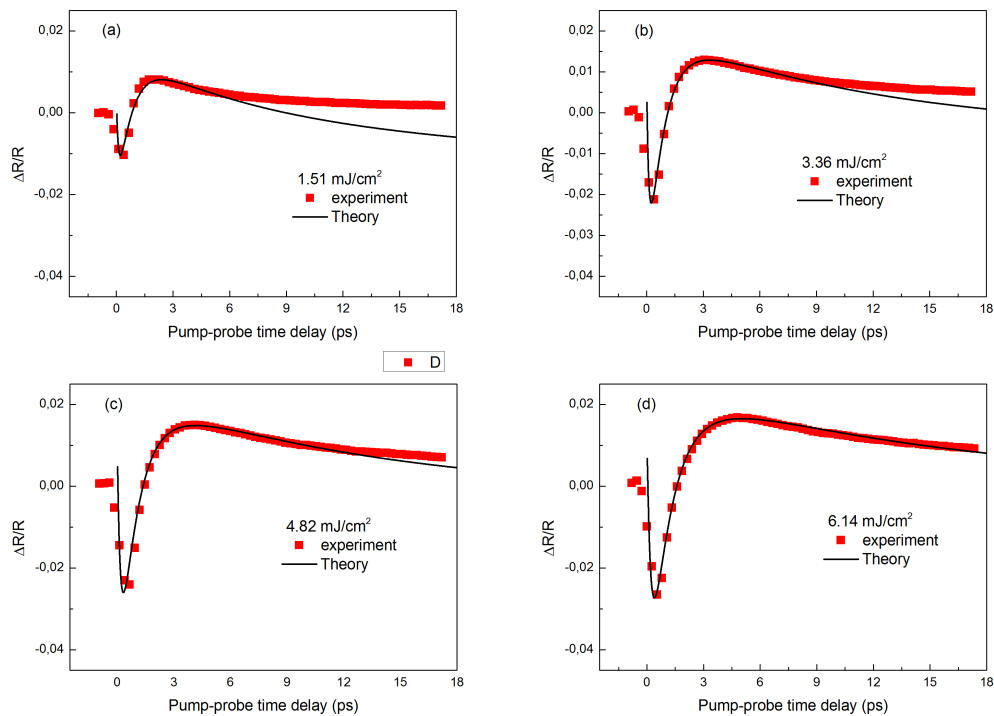


Figure 3.20: Comparison of the high fluence measurements with the simulations. - The red squares represent the measured data, the black line shows the simulation with the parameters listed in table 3.3.

3.4 Time-Resolved Reflectivity Measurement and Discussion

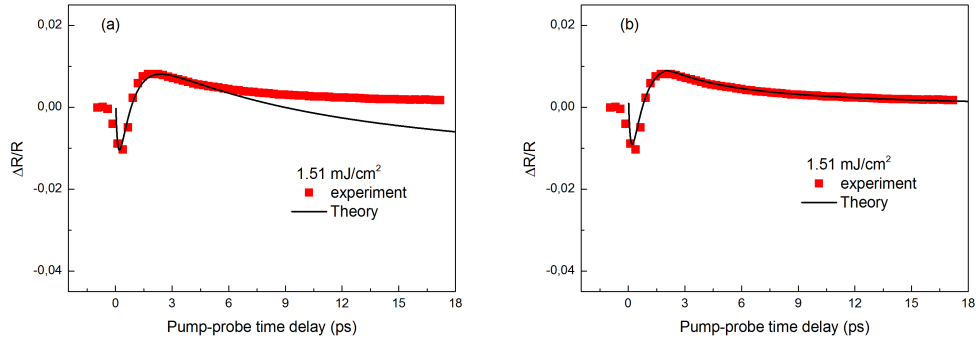


Figure 3.21: Comparison of the experimentally measured data and simulations. - Left: simulations with a constant recombination coefficient listed in table 3.3. Right: using two recombination coefficients below and above a certain carrier density (see text).

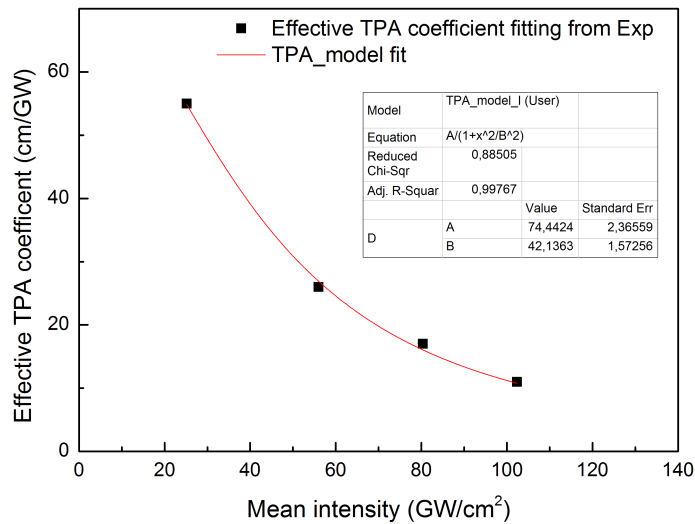


Figure 3.22: The effective TPA coefficient. - The black squares are the value used in the simulations, the red line is a data fit according to the TPA model proposed by [79].

3. ULTRAFAST DYNAMICS IN HIGHLY EXCITED CDTE: THE TIME-RESOLVED REFLECTIVITY MEASUREMENT

3.5 Conclusion

The time-resolved reflectivity technique was applied to investigate the ultrafast dynamics in CdTe. At laser fluences below $0.6 \text{ mJ}\cdot\text{cm}^{-2}$, the coherent LO phonons and their coupling with the plasmons were measured. At higher fluence ($> 0.6 \text{ mJ}\cdot\text{cm}^{-2}$), the time-dependent reflectivity curves show a complex interplay between photoexcitation, carrier relaxation and recombination. The experimental results were analyzed in terms of the susceptibility model proposed by H. Haug [63] and the carrier rate equations from the extended Stanton-Bailey model. In the high-excitation regime, the Coulomb screening and polar character of CdTe affects strongly the ultrafast cooling and recombination of hot carriers. In case of recombination, the screening reduces the Coulomb interaction between electrons in the conduction band and holes in the valence band making thus the recombination coefficient a density-dependent quantity. One outcome of Coulomb screening and the polar character of the CdTe is, that at high fluences the hot carriers lose their excess energy mainly by interacting with the lattice via the plasmon-phonon coupling mechanism. The dominant energy loss channel is the L^+ mode [19], which has a much higher frequency and energy than a bare LO mode, and, hence, reduces the carrier's excess energy more efficiently than emitting a pure LO phonon. Moreover, it was found that the two-photon absorption coefficient used in the simulation agrees very well with a TPA saturation model proposed in [79].

Chapter 4

Ultrafast Dynamics in Laser-Excited Diluted Magnetic Semiconductors

4.1 Introduction

The interaction of phonons with the magnetic atoms in diluted magnetic semiconductors (DMSs) is a topic which has attracted widespread attention [80, 81, 82]. Apart from the fundamental interest, acoustic phonons could also be considered as an effective tool to manipulate magnetization on ultrashort time scales. Pumping this magnetic system with ultrashort laser pulses can strongly alter the thermodynamic equilibrium among the constituents, the carriers, spins, and the lattice, triggering a variety of dynamical processes. Investigating these processes shed new light on how to optimize an ordered phase for innovative applications that combine both, the semiconductor transport (which requires suppression of phonons) and magnetic storage (which requires increasing of spin coherence time).

Time-domain information about magnetic properties of DMSs have, typically, employed time-resolved magneto-optical spectroscopy (giant Faraday rotation or magneto-optic Kerr effect). This method has provided essential contributions to understanding of exchange interactions, spin relaxation, spin coherent effects and dephasing phenomena [23, 24, 25, 26, 28, 29]. X-ray diffraction, on the other hand, can directly observe the small shifts in interatomic distance associated with coherent phonons [30, 31, 32, 33, 34, 35, 36]. Complemented with the resonant X-ray emission spectroscopy which is capable of probing the dynamics of holes in the valence band (which

4. ULTRAFAST DYNAMICS IN LASER-EXCITED DILUTED MAGNETIC SEMICONDUCTORS

mediate the ferromagnetism), X-ray diffraction provides vital information about the correlation of lattice, spins and charge.

This chapter presents (i) probing of coherent acoustic phonons in ferromagnetic $\text{Ga}_{1-x}\text{Mn}_x\text{As}$ by means of time-resolved X-ray diffraction and (ii) redistribution of holes in the valence band by using time-dependent resonant X-ray emission. These measurements were performed at the Linac Coherent Light Source (LCLS) which generates sub picosecond, energy-tunable X-ray pulses that provide the spatial and temporal resolution required for investigating basic carrier scattering mechanisms and their coupling to structural evolution of the material.

This chapter starts with a brief introduction of the free-electron laser (section 4.2). Section 2, presents a brief overview of (a) ferromagnetism in DMSs, (b) coherent acoustic phonons, (c) X-ray diffraction from the acoustic phonons and (d) resonant X-ray emission. In section 3, the experimental configuration and set up is described. Experimental results and discussion on the X-ray diffraction and resonant X-ray emission of laser excited $\text{Ga}_{1-x}\text{Mn}_x\text{As}$ are presented in Sections 4 and 5, respectively. Finally, concluding remarks are given in Section 6.

4.2 The Free Electron Laser

The free-electron laser (FEL) is a laser source which takes a beam of free electrons as the active medium instead of atoms or molecules in a conventional laser. When the free electrons propagate through a spatially periodic magnet field at relativistic velocities, the Lorentz force compels them to oscillate perpendicular to the traveling direction. This motion leads to synchrotron radiation in the propagating direction. Usually, most of this radiation is incoherent, as shown in figure 4.1 (left). The collective interaction between electrons and their emitted radiation field enhances a small fraction of coherent fluctuations in the radiation field, and simultaneously the electrons begin to bunch at the resonant wavelength. As long as this collective process continues, the electrons are continually bunched until the end of the undulator, and therefore emit coherent radiation [83], as illustrated in figure 4.1 (right).

One advantage of using FELs comes from its peak brightness which is up to one billion times higher than that of an ordinary synchrotron radiation source. It thus can excite a large fraction of core level electrons and, as a result, even minimal physical effects can be observed much easier, due to an enhancement of the signal-to-noise ratio. Another use advantage for ultrafast science lies in the time resolution. A typical pulse duration of a FEL pulse is in the sub picosecond region even reach a few femtosecond,

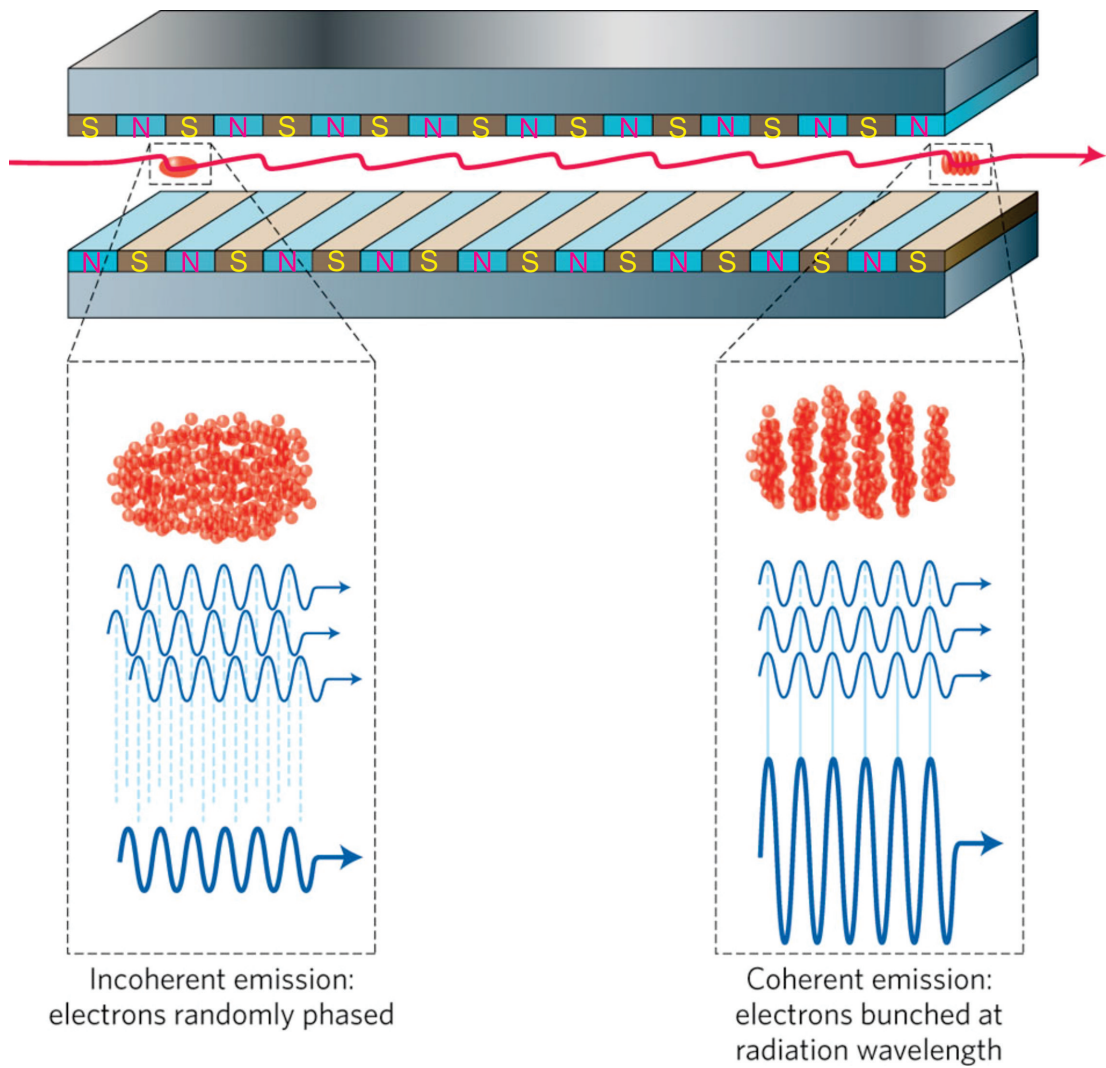


Figure 4.1: The operation principle of an FEL. - S and N are the poles of the magnet of the undulator, red particles are electrons (picture took from [83]).

4. ULTRAFAST DYNAMICS IN LASER-EXCITED DILUTED MAGNETIC SEMICONDUCTORS

which gives us the potential to investigate the most interesting dynamics which happen on a picosecond time scale.

The experiment was performed at the FEL facility, the Linac Coherent Light Source (LCLS) at Stanford, which is the first FEL in the hard X-ray regime. Table 4.1 lists typical FEL parameters at the X-ray pump-probe station (XPP), where this experiment was carried out.

Table 4.1: LCLS FEL parameters

Parameter	Value
Energy Range	4-10 keV (fundamental)
	10 - 25 keV (harmonics)
Energy Resolution ($\Delta E/E$)	Silicon (111): 1.4×10^{-4}
Repetition Rate	Single pulse, 0.5, 1, 5, 10, 30, 60, 120 Hz
Pulse Duration	80 fs (nominal)
	100-200 fs in chirped beam mode
	< 20 fs in short pulse mode
Pulse Energy	2 mJ nominal
	~ 0.5 mJ in chirped beam mode
	0.2 mJ in short pulse mode

4.3 General Considerations: Mechanisms, Dynamics and Probe

4.3.1 Ferromagnetism in DMSs

In $\text{Ga}_{1-x}\text{Mn}_x\text{As}$ the Mn ions act both as a source of localized spins ($S = 5/2$) and effective mass acceptors. When the Mn concentration is increased and reaches a value high enough to realize the degenerate condition in the valence band ($> 10^{20} \cdot \text{cm}^{-3}$) and the crystal temperature is low enough (for $\text{Ga}_{0.91}\text{Mn}_{0.09}\text{As}$, depending on the crystal quality, below 173 K), the itinerant hole carriers mediate the ferromagnetic alignment of the magnetic ions. In the framework of the Zener kinetic exchange model [3] (which in the case of semiconductors is equivalent to the RKKY model) the hole-induced ferromagnetism can be described as mutual polarization of the holes by the localized spins and of the localized spins by the holes. This interaction is described by a Hamiltonian

4.3 General Considerations: Mechanisms, Dynamics and Probe

of the form

$$H_{pd} = -\beta N_0 \mathbf{s} \cdot \mathbf{S} \quad (4.1)$$

where β is the p-d exchange constant, N_0 is the concentration of Mn atoms, \mathbf{s} is the spin of holes, and \mathbf{S} is the spin of Mn ions.

The Curie temperature predicted by this model is proportional to the square of the p-d exchange constant β (for $\text{Ga}_{1-x}\text{Mn}_x\text{As}$ the p-d exchange constant β is about a factor of 6 larger than the s-d constant α), and through the Pauli susceptibility to the density of states at the quasi-Fermi level (therefore holes are much more efficient than electrons in mediating ferromagnetism in DMSs because both, the exchange coupling constant β and the effective mass are larger); with respect to hole concentration N_h , the Curie temperature can be approximately expressed as $T_C \propto N_0^{1/3}$. Pumping this magnetic system with ultrashort laser pulses will increase the hole density (up to $\sim 10^{20} \cdot \text{cm}^{-3}$) and thus, in principle, the magnetization of $\text{Ga}_{1-x}\text{Mn}_x\text{As}$ is expected to increase. However at the same time the photoexcited holes will transfer their excess kinetic energy to spins via carrier-spin coupling thus heating the spin system (i.e. demagnetizing the crystal).

Lattice: Strain-Magnetic Interaction

In addition to the holes, the strain also affects ferromagnetism in $\text{Ga}_{1-x}\text{Mn}_x\text{As}$. It is predicted that both, the tensile and compressive strains diminish T_C by a few percent at a hole concentration $\sim 2 \times 10^{20} \text{ cm}^{-3}$ [84]. Strains lead to uniaxial anisotropy, as first pointed out by H. Ohno [21] who found that in $\text{Ga}_{1-x}\text{Mn}_x\text{As}$, the magnetic anisotropy is strongly sensitive to the epitaxial strain (the physical origin of this feature is due to the spin-orbit coupling [85]). In principle, the strain modifies the deformation potential and, therefore affects the valence band dispersion directly. The deformation potential Hamiltonian is given by [85, 86] (details can be found in chapter 2):

$$H_\epsilon = \sum_{i,j} D^{i,j} \epsilon_{i,j} \quad (4.2)$$

$D^{i,j}$ is the deformation potential operator, ϵ is the strain.

On the other hand, the induced deformation would modify the overlap of the hole cloud and the Mn ion d-shell electron cloud, thus perturbing the hybridization [82, 87]. Within the Heisenberg model framework, the strain modifies the exchange integral J , so that the interaction Hamiltonian can be written as:

4. ULTRAFAST DYNAMICS IN LASER-EXCITED DILUTED MAGNETIC SEMICONDUCTORS

$$H = -\frac{1}{2} \sum_{i,j} J(\delta + u_{i+\delta} - u_i) S_i \cdot S_{j+\delta} \quad (4.3)$$

where the u_i 's are the displacements of the lattice sites, and δ is the distance between neighbors.

Propagating strains in the sample will tilt the direction of the magnetization M . The collective magnetization dynamics is described by the Landau-Lifshitz-Gilbert equation [81, 88, 89]:

$$\frac{\partial M}{\partial t} = -\gamma M \times H_{eff} + \frac{\alpha}{M_s} M \times \frac{\partial M}{\partial t} + T \quad (4.4)$$

Here, γ is the gyromagnetic ratio, H_{eff} is some effective magnetic field, and α is the Gilbert damping parameter.

When a strain propagates in the sample the energy is transferred from phonons to the spin system. By studying the acoustic phonons above and below T_C , one could obtain information of the spin dynamics.

4.3.2 Probe Lattice Dynamics: X-ray diffraction

4.3.2.1 Lattice Dynamics: Strain Generation

The transfer of energy from the laser pulse puts the lattice into a highly stressed state. Stress is relieved by thermal expansion of the lattice which, when moving to the new equilibrium state, overshoots (because of the inertia) and coherently oscillates, giving rise to the coherent acoustic phonons.

The generation and propagation of the laser-induced coherent strain waves was presented by Thomsen et al. [90]. In this model the thermal stress σ_{th} is proportional to the lattice temperature increase ΔT , due to the photoexcitation.

$$\sigma_{th} = -3B\beta\Delta T(z) \quad (4.5)$$

$$\Delta T(z) = (1 - R) \frac{Q}{A\zeta C} e^{-z/\zeta} \quad (4.6)$$

where R is the reflectivity, Q is the thermal energy, C is the specific heat per unit volume, B is the bulk modulus and β is the linear expansion coefficient, ν is the Poisson's ratio.

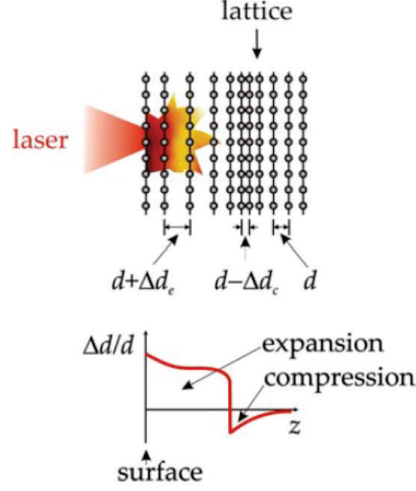


Figure 4.2: The strain generation mechanism. - d is the lattice spacing, the strain wave is $\eta(t) = \Delta d(t)/d(t)$.

By using the equations of motions for the lattice, the strain wave can be written as [90]:

$$\eta_{33}(z, t) = [\Delta T(0)] \left(\frac{1 - \nu}{1 + \nu} \right) \left[e^{-z/\zeta} \left(1 - \frac{1}{2} e^{-vt/\zeta} \right) - \frac{1}{2} e^{-|z-vt|/\zeta} \text{sgn}(z - vt) \right] \quad (4.7)$$

where v is the longitudinal sound velocity given by:

$$v^2 = 3 \left(\frac{1 - \nu}{1 + \nu} \right) \frac{B}{\rho} \quad (4.8)$$

The Thomsen model assumes that the excited carriers transfer energy instantaneously to the lattice, which is reasonable in many cases due to the ultra-short energy delivery time. A more realistic model should take into account the electron-phonon coupling which mediates the energy transfers from carriers to the lattice. Such models have been presented in references [32] and [77]. An example where the strain is generated by taking the analytic expression described in [77] is shown in figure 4.3.

4.3.2.2 Takagi-Taupin equations

In order to compute the X-ray diffraction changes from the photoexcited sample, one needs to use the dynamical theory of X-ray diffraction which takes into account the interaction of wavefields in the crystal.

4. ULTRAFAST DYNAMICS IN LASER-EXCITED DILUTED MAGNETIC SEMICONDUCTORS

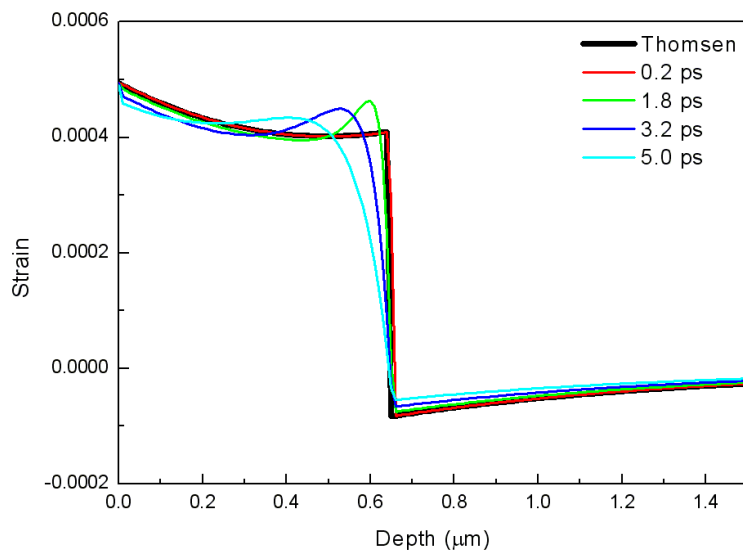


Figure 4.3: Comparison of the standard Thomsen model with the modified one.

- The strain is propagated for 120 ps after laser excitation, an electron-phonon coupling time of 5 ps cause obvious changes as compared to the standard Thomsen model.

4.3 General Considerations: Mechanisms, Dynamics and Probe

A widely used approach is that of Takagi and Taupin [33, 34, 91] which models the X-ray diffraction from coherent acoustic phonons. The formula of the equations is described in [35, 36, 77]. An analytical solution of the Takagi-Taupin equation can be found in [36, 77, 92]. The rocking curve of the perturbed crystal $R(\Delta\theta) = |D_h/D_0|^2$, where D_0 and D_h are the incident and the reflected wavefields, can be calculated as:

$$\xi(z) = \frac{s\xi_0 + (B\xi_0 + C)\tan[(s(z - z_0))]}{s - (A\xi_0 + B)\tan[(s(z - z_0))]} \quad (4.9)$$

$$\sqrt{\frac{|\gamma_h|}{\gamma_0}} \frac{D_h}{D_0} = \xi / \left(\text{sgn}^{-1}(P_o) \frac{\chi_h^-}{\sqrt{\chi_h \chi_h^-}} \right) \quad (4.10)$$

Where

$$A = \frac{\pi i}{\Gamma} \quad (4.11)$$

$$B = -\frac{\pi i}{\Gamma} \text{sgn}(\gamma_h) \beta_{\Delta\theta} \quad (4.12)$$

$$C = -\frac{\pi i}{\Gamma} \frac{\gamma_h}{|\gamma_h|} \quad (4.13)$$

$$\beta_{\Delta\theta} = \sqrt{\frac{\gamma_0}{|\gamma_h|}} \left[\kappa \sin 2\theta_B - \frac{1}{2} \chi_0 \left(\frac{\gamma_h}{\gamma_0} - 1 \right) \right] / (|P_o| \sqrt{\chi_h \chi_h^-}) \quad (4.14)$$

$$\kappa = \Delta\theta + \eta [\cos^2 \alpha \tan \theta_B + \sin \alpha \cos \alpha] \quad (4.15)$$

$$s = \sqrt{AC - B^2} \quad (4.16)$$

$$\Gamma = \frac{\lambda \sqrt{\gamma_0 |\gamma_h|}}{|P_o| \sqrt{\chi_h |\chi_h^-|}} \quad (4.17)$$

$$\chi_h = \frac{r_0 \lambda^2 F_h}{\pi V_u} \quad (4.18)$$

$\chi_h^- = \chi_{-h}$, ξ_0 is ξ at zero depth, the $\gamma_{0,h}$ are the direction cosines of the incident or diffracted beam, λ is the X-ray wavelength, r_0 is the classical electron radius. V_u is the volume of the unit cell, F_h is the structure factor. P_o is the polarization factor.

The rocking curve at different time delay therefore can be computed by combining equation 4.9 to 4.18 take into account the strain simulated in section 4.3.2.1 by the equation 4.15. One example for a single GaAs crystal is shown in figure 4.4.

4.3.3 Probe Hole's Nonequilibrium Distribution: Resonant X-ray Emission

Free-electron laser (FEL) radiation can be used to probe the dynamics of carriers in the energy bands by means of resonant X-ray emission (RXE). One can tune the X-ray

4. ULTRAFAST DYNAMICS IN LASER-EXCITED DILUTED MAGNETIC SEMICONDUCTORS

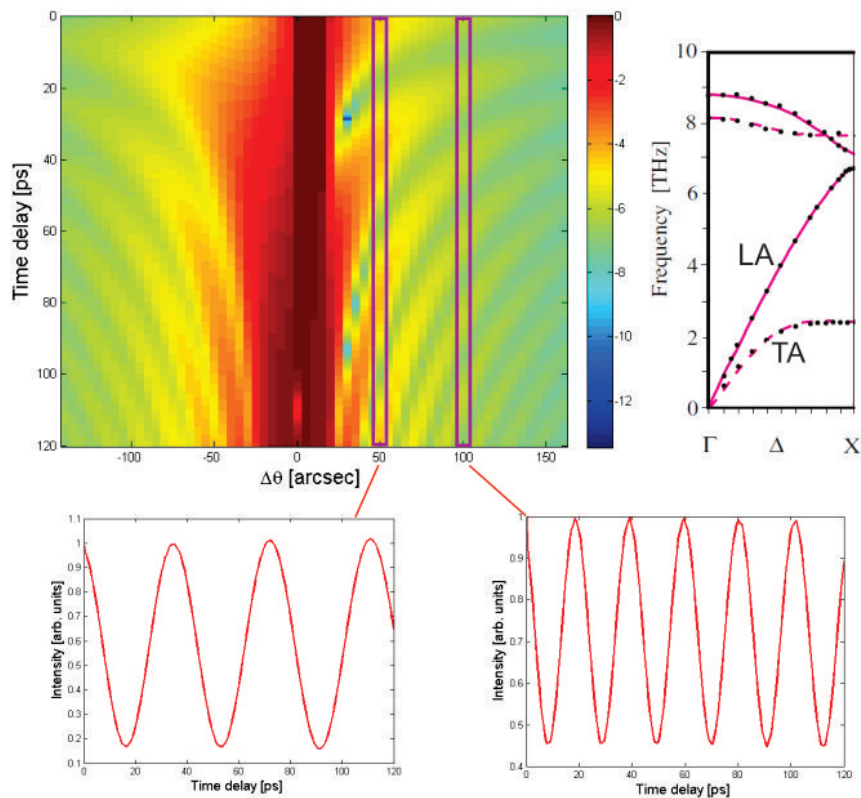


Figure 4.4: The rocking curve and the phonon dispersion relation. - The simulation is based on assuming that the strain is propagating along the (001) direction (equal to Γ to X in reciprocal space). The phonon dispersion at the right side shows that by increasing Δq , the acoustic phonon frequency is increasing as well. In real space this is corresponding to changes in θ , therefore, oscillations at $\Delta\theta = 100$ arcsecond have a higher frequency than at 50 arcsecond.

4.3 General Considerations: Mechanisms, Dynamics and Probe

energy to drive a transition from an inner shell (core level of Ga) to the valence band (dotted line) (see the figure 4.5). Depending on the hole density N_h and temperature T_h the phase space in the valence band (VB) where the transition takes place will be filled or empty. If the phase space in the VB is filled the transition from the core level is blocked (i.e. X-ray absorption is suppressed) and no fluorescence photons are emitted. If the phase space is cleared out by the intra- and interband relaxation processes which redistribute carriers in their respective bands, the transition from the core level is allowed and X-ray absorption followed by the fluorescence is increased. The RXE can be quantized by the Kramers-Heisenberg cross section (see Appendix 5 for details).

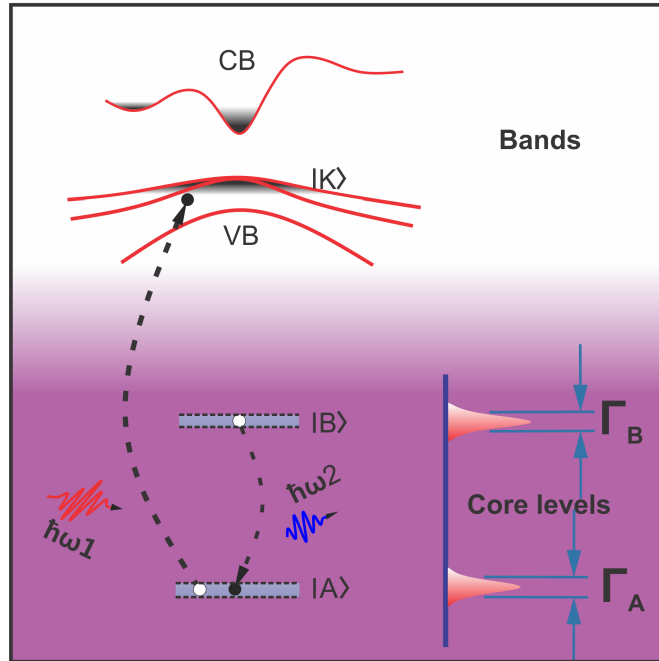


Figure 4.5: The FEL resonant X-ray emission probe principle. - When the band is occupied, the transition is forbidden, otherwise, it can happen.

$$\frac{\partial^2 \sigma}{\partial \Omega \partial \omega_2} = |M|^2 \times \delta(\hbar\omega_1 - \hbar\omega_2 - E_b - E_k) \quad (4.19)$$

where M is:

$$M = \frac{2c}{m} \int \frac{dk}{2\pi^3} (1 - f_k) \frac{\langle B | (e_2 \cdot \mathbf{p}) e^{-ik_2 \cdot r} | A \rangle \langle k | (e_1 \cdot \mathbf{p}) e^{-ik_1 \cdot r} | A \rangle}{E_k - E_a - \hbar\omega_1 - i\Gamma/2}$$

Here $|A\rangle$ is the initial state, $|K\rangle$ is the final state in the valence band, $|B\rangle$ is the upper core level, f_k (equation) is the distribution function of holes in the valence band,

4. ULTRAFAST DYNAMICS IN LASER-EXCITED DILUTED MAGNETIC SEMICONDUCTORS

Γ is the core level width, and e_1 and e_2 are the polarization vectors of the incident and scattered photons, respectively.

$$f_k = \frac{1}{e^{[\varepsilon(k)-\mu]/k_B T}-1} \quad (4.20)$$

The μ is the quasi-Fermi level of holes in valence band.

4.4 The X-ray Diffraction and Emission Spectroscopy Experimental Setup

The operation principle of the experimental setup is shown in figure 4.6. Here, a 800 nm wavelength, 50 fs pulselength laser is used to pump the sample. The power of the laser can be adjusted from a few 100 $\mu\text{J}\cdot\text{cm}^{-2}$ to $\sim 10 \text{ mJ}\cdot\text{cm}^{-2}$ linearly and allows for a power-dependent generation of strain waves and nonequilibrium distributed holes in the valence band. The strain waves and the nonequilibrium distributions of holes are expected to be probed by the FEL via measuring the modifications of the X-ray diffraction and the resonant X-ray photon emission yield. The FEL and the pump laser beam are entering the interaction chamber in collinear configuration in order to ensure a sufficient overlap of both beams at the interaction point on the sample. The crystal is mounted on a multidimensional stepper motorized travel stage. With the adjustable Bragg angle measured with respect to the FEL beam axis, the diffraction intensities are measured by a silicon X-ray diode. Simultaneously, the X-ray emission is monitored by a pn-junction charge coupled device (pnCCD) with 1024×1024 pixels on an area of $76.8 \times 76.8 \text{ mm}^2$. The $\text{Ga}_{1-x}\text{Mn}_x\text{As}$ samples are grown on the GaAs (001) substrate with thin $\text{Al}_{0.2}\text{Ga}_{0.8}\text{As}$ and GaAs buffer layers. Thus, the surface is naturally normal to the (001) direction. The Bragg angle θ_B at a FEL photon energy of about 10.363 keV is roughly $\sim 25^\circ$. The pnCCD is installed at an angle of 90° relative to the FEL beam in order to suppress contributions from the Thomson and Compton scattering processes, which have a maximum at 180° relative to the incident beam and diminish theoretically to zero at 90° . A more detailed theoretical description is given by equation 24 in Appendix 5.

The installation of the setup is shown in figure 4.7. In order to mount the pnCCD on the XPP interaction chamber, an auxiliary chamber was designed and manufactured, see the figure 4.8. The XPP interaction chamber needs to be pumped to a high vacuum level $< 10^{-6}$ torr in order to avoid the air absorption of radiation. The operation of the pnCCD requires a higher vacuum level of 10^{-5} torr and a cooling down to a temperature

4.4 The X-ray Diffraction and Emission Spectroscopy Experimental Setup

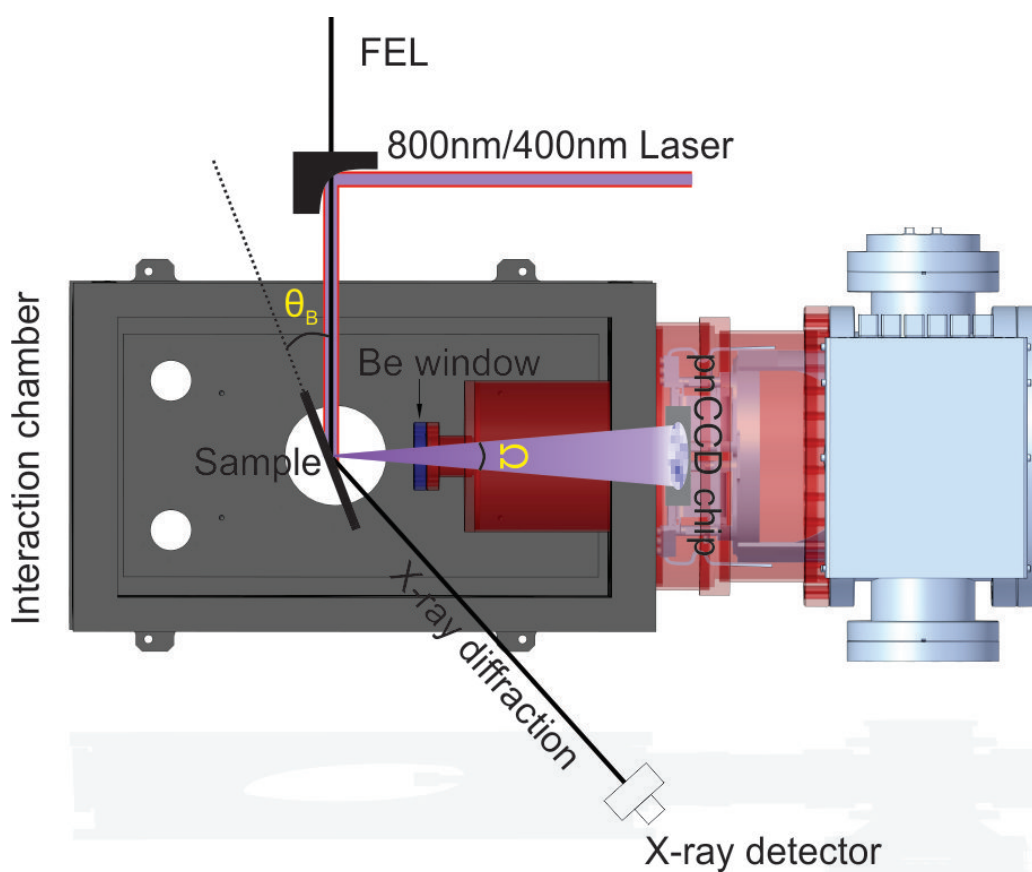


Figure 4.6: The experimental geometry - The dark line is the FEL beam, the red line is the 800 nm femtosecond laser beam and, the violet line is the 400 nm laser beam. Resonant X-ray emission is plotted with transparent violet. θ_B is the Bragg angle, Ω is the solid angle of the fluorescence collected by the pnCCD. The transparent red part is a vacuum chamber designed to connect the XPP chamber and pnCCD chamber.

4. ULTRAFAST DYNAMICS IN LASER-EXCITED DILUTED MAGNETIC SEMICONDUCTORS

of about $-60\text{ }^{\circ}\text{C}$ in order to enhance the signal-to-noise ratio. However, based on considerations of convenience, the two chambers should not share the same vacuum. Because during the experiment, one may need to open the XPP interaction chamber for a couple of times. In a connected vacuum this would require to warm up the pnCCD detector from cryogenic temperatures which takes hours including the then mandatory subsequent cool down process. Therefore, the XPP interaction chamber and the pnCCD chamber are separated by a beryllium window, which can sustain the pressure difference between both sides, and is transparent to the X-ray fluorescence photons. At the same time, blocks the scattered pump laser photons in order to avoid any background on the pnCCDs. The window is realized as a CF-40 flange with a beryllium foil welded in. In order to collect the RXE photons efficiently through the small aperture (37 mm) of the auxiliary chamber (neck dimension), the beryllium window has to be placed at a distance of 15 cm to the interaction point. At this distance, the 37 cm aperture does not block any fluorescence light going to the pnCCD detector (as shown in figure 4.6). This is achieved by the extension part of the auxiliary chamber, as shown in figure 4.8. The design of the extension part is such that it avoids conflicts with other devices in the XPP interaction chamber.

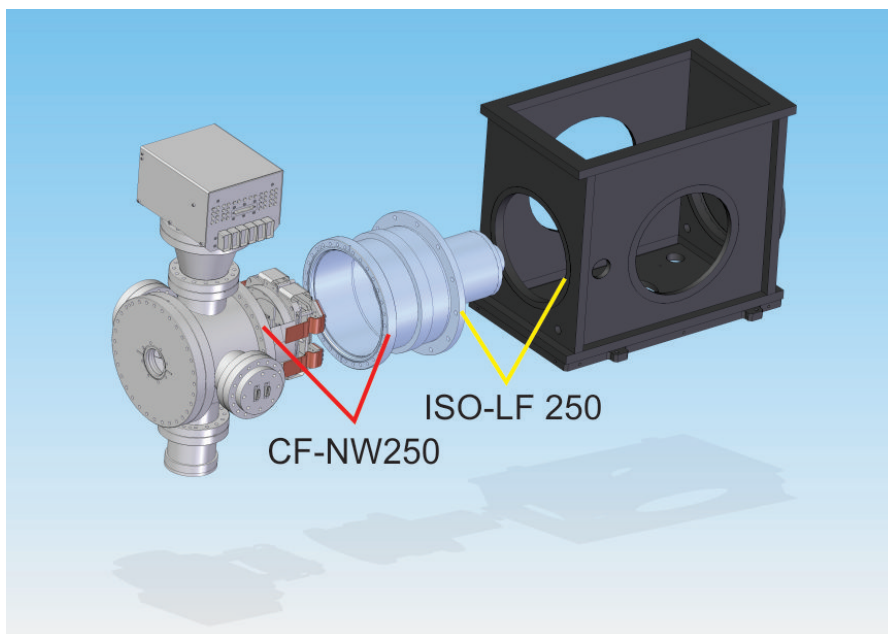


Figure 4.7: Explosion view of the set up. - The vacuum chamber in the middle is designed to connect the pnCCD chamber (on the left) with the XPP interaction chamber.

The window is made of a thin beryllium foil as shown in figure 4.9. In order

4.4 The X-ray Diffraction and Emission Spectroscopy Experimental Setup

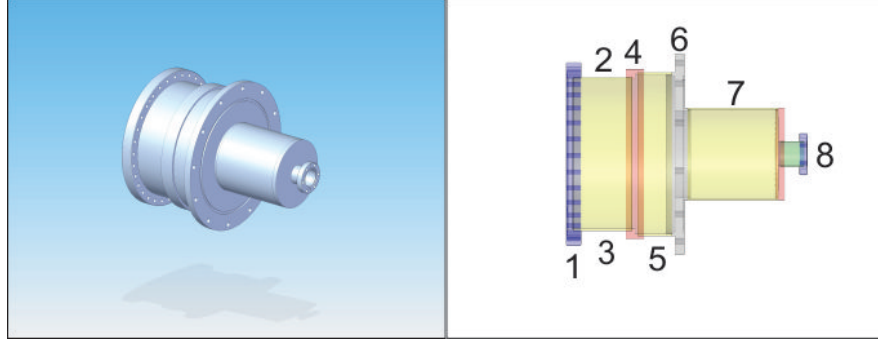


Figure 4.8: View of the auxiliary chamber. - (Left) Isometric projection. (Right) Side view. Different parts of the chamber are plotted with different color and labeled with numbers, 1 is a standard CF-NW 250 flange, 6 is a ISO-LF 250 flange designed according to the MDC Vacuum Products LLC's standard [93], 7 is a extension part, 8 is a CF 40 flange and connects the beryllium window flange.

to minimize the absorption of the fluorescence photons, one needs to choose the foil as thin as possible, but strong enough that it holds the pressure difference between the two chambers which can be the equivalent of one atmosphere. In order to get a balance between thickness and the aperture size, one needs to solve the system of stress and strain equations [94], which are equations connecting thickness, radius and the maximum pressure on the foil:

$$\frac{qr^4}{t^4} = K_1 \frac{y}{t} + K_2 \left(\frac{y}{t}\right)^3 \quad (4.21)$$

$$\frac{\sigma r^2}{Et^2} = K_3 \frac{y}{t} + K_4 \left(\frac{y}{t}\right)^3 \quad (4.22)$$

where t is the foil thickness, r is the radius of aperture, y is the maximum deflection and σ the maximum stress due to bending and tension. K_1 to K_4 are parameters shown in [94]. By solving these equations, one obtains a minimum thickness of roughly 0.2 mm with a standard CF 40 flange aperture (typically 37 mm). A standard beryllium window (from Materion Corporation) is shown in figure 4.9, it can withstand atmosphere pressure in the direction shown in the figure, but would break if used the other way around.

The pnCCD is a detector ideally suited for X-ray spectroscopy experiments and has been heavily used for experiments at the LCLS facility [95]. In contrast to the conventional metal-oxide-silicon (MOS) based CCDs, the pnCCDs are based on high-resistivity n-type silicon. By a special manufacturing process it is possible to make use of the full depth of the bulk material as a sensitive volume for the conversion of

4. ULTRAFAST DYNAMICS IN LASER-EXCITED DILUTED MAGNETIC SEMICONDUCTORS

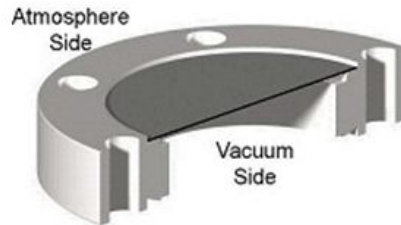


Figure 4.9: Cut-view of the beryllium window flange. - The thin layer is the beryllium foil.

the incident X-rays into electron-hole pairs. Since all pixels of the sensor are built up with pn-junctions instead of MOS structures, the device is denoted pnCCD. The pnCCD used in this experiment is manufactured by the Max Planck Semiconductor Laboratory. The setup is shown in figure 4.10, the pnCCD sensors are indicated in yellow color. The cooling of the chip is realized by a helium cryogenic cooler.

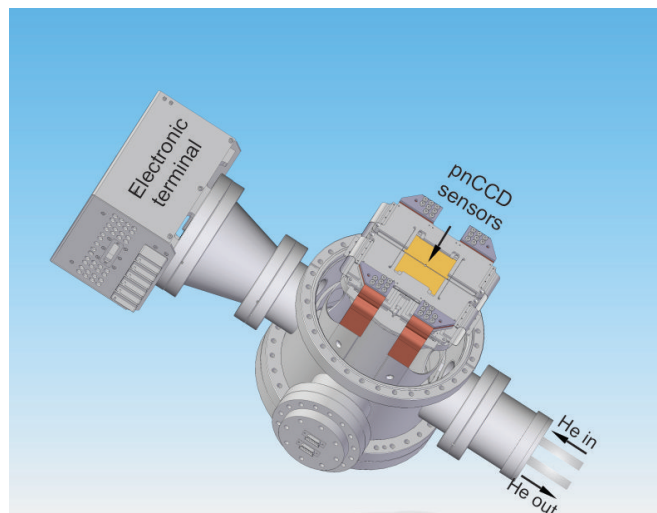


Figure 4.10: Isometric view of the pnCCD assembly. - The pnCCDs are mounted on top of a support stand sticking 200 mm out of a CF250-cross, which houses further infrastructure to operate the device, e.g., the cold head for cooling. The square one is the electronic terminal box. Helium is pumped into the chamber in order to cool the chip.

The pnCCD is calibrated by linking its energy scale to the known radiation of a standard X-ray source. For this experiment, a F_e^{55} radiation source was used, which had to be fixed in front of the pnCCD sensor by an appropriate adapter, see the figure 4.11.

4.4 The X-ray Diffraction and Emission Spectroscopy Experimental Setup

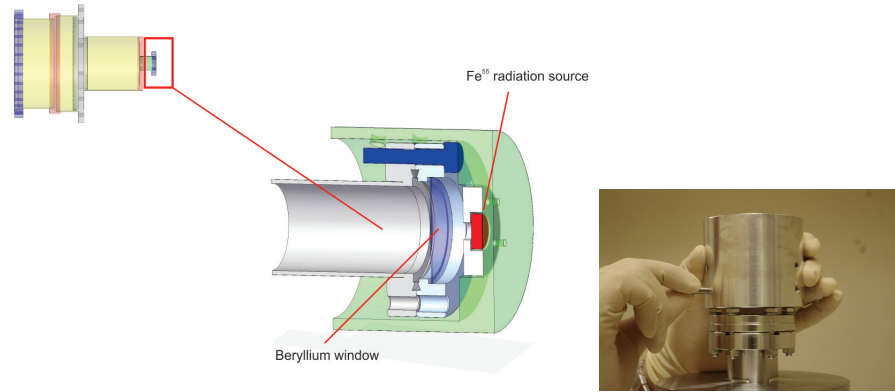


Figure 4.11: The Fe^{55} radiation source is fixed by a ring into the green transparent adapter and then installed on the top of the auxiliary chamber with the beryllium window in between.

For the investigation of the $Ga_{1-x}Mn_xAs$ in ferromagnetic phase, the sample needs to be cooled down. The cooling system is depicted in figure 4.12. In order to rotate the sample freely and reduce the vibration from the pump system of the closed-cycle helium cryocooler, the sample is not directly mounted on the cold finger, but attached to a flexible sample holder from which the heat is transferred by a copper hemp rope to the cold finger. The efficiency of cooling is sufficiently high even if the sample is not directly attached on the cold finger, and a minimum of 40 K at the crystal could be reached during the experiment.

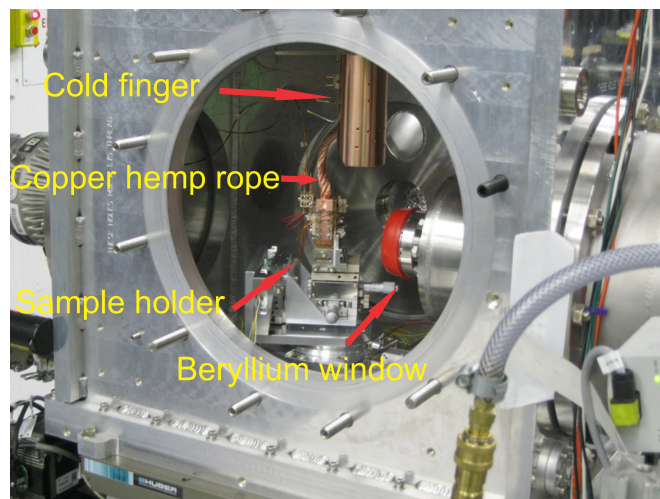


Figure 4.12: The sample cooling system. - The cold finger is connected with a closed-cycle Helium cryo-cooler.

4. ULTRAFAST DYNAMICS IN LASER-EXCITED DILUTED MAGNETIC SEMICONDUCTORS

4.5 Results of Time Resolved X-ray Diffraction

In this section, the influence of the magnetic ordering on the coherent acoustic phonons is shown. In the experiment, the evolution of the X-ray diffraction intensity was measured at different angular positions from the unperturbed rocking curve peak, see the figure 4.13.

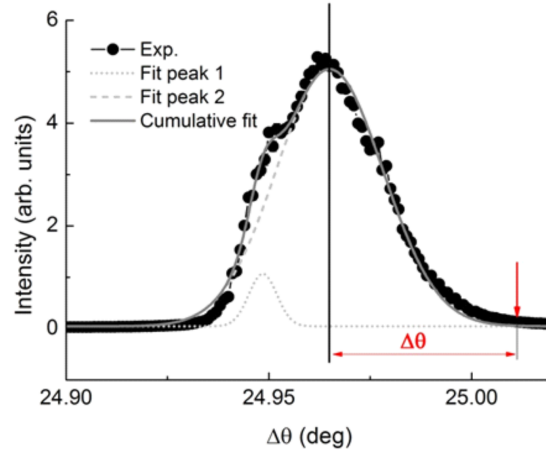


Figure 4.13: The $\Delta\theta$ defined from the unperturbed rocking curve. - $\Delta\theta$ is measured from the center of gravity of the rocking curve.

From the framework present in Appendix 5 (equation 2 and 3) one knows that time resolved X-ray diffraction measured at $\Delta\theta$ will probe acoustic phonons with a wavevector $q(\Delta\theta)$:

$$q(\Delta\theta) = \frac{\Delta\theta |G_{hkl}|}{\tan\theta_B} \quad (4.23)$$

(I). Room Temperature Measurements

Coherent acoustic phonons with a wavevector q modulate the d-spacing of a crystal and, as a result, the time-resolved X-ray diffraction intensity will oscillate with an angular frequency $\omega_q = v_s \cdot q$. In Figures 4.14 and 4.15 the measured time-dependent X-ray diffraction intensity (normalized to the average intensity before time zero) at two different fluences, 4 and 6.5 $\text{mJ}\cdot\text{cm}^{-2}$ are shown. The time scans were measured at three different positions from the unperturbed peak, $\Delta\theta_1 = (0.034 \pm 0.03)$ deg, $\Delta\theta_2 = (0.039 \pm 0.03)$ deg and $\Delta\theta_3 = (0.049 \pm 0.03)$ deg, which according to equation

4.5 Results of Time Resolved X-ray Diffraction

4.23 probe the coherent acoustic phonons with q-vectors $q_1 = (0.010 \pm 0.001)\frac{\pi}{a}$, $q_2 = (0.012 \pm 0.001)\frac{\pi}{a}$ and $q_3 = (0.015 \pm 0.001)\frac{\pi}{a}$, respectively.

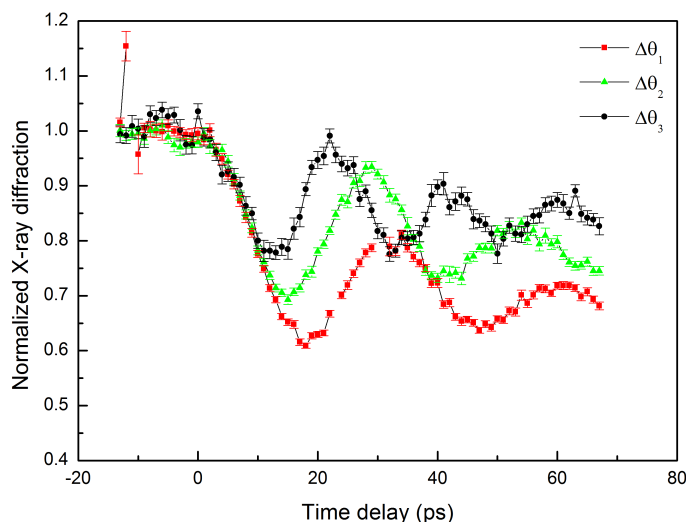


Figure 4.14: The XRD intensity modified by the acoustic-phonons at the pump fluence $4 \text{ mJ}\cdot\text{cm}^{-2}$. - The oscillations are observed at three different angles at the larger (compressive) side of the rocking curve.

Near the center of the Brillouin zone, the acoustic phonon dispersion is linear, therefore the sound velocity V_s can be extracted from the measured phonon-dispersion in figure 4.16 by the formula [34]:

$$V_s = \frac{\omega}{|G| \Delta\theta \cot(\theta)} \quad (4.24)$$

$|G|$ is the absolute value of the reciprocal lattice vector G . The sound velocity extracted from these data is $V_s \approx 4705 \text{ m} \cdot \text{s}^{-1}$ which is in excellent agreement with the longitudinal sound velocity measured in $\text{Ga}_{1-x}\text{Mn}_x\text{As}$ ($4830 \pm 70 \text{ m} \cdot \text{s}^{-1}$) [96] and, $4770 \text{ m} \cdot \text{s}^{-1}$ in GaAs (at (001) direction) [97]. This indicates that pure longitudinal acoustic phonon modes are probed.

Apart from that, the measured oscillations are damped. The damping arises (i) due to the attenuation of the phonon mode and, (ii) due to the width of the rocking curve. Lindenberg, et al. [34] measured the acoustic phonons in InSb by X-ray diffraction and, observed similar damping behavior; they attributed the damping to the angular resolution of the measurement.

4. ULTRAFAST DYNAMICS IN LASER-EXCITED DILUTED MAGNETIC SEMICONDUCTORS

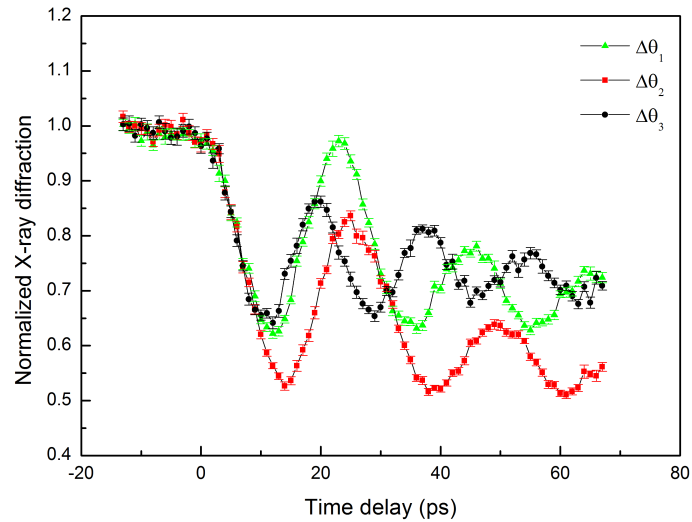


Figure 4.15: The XRD intensity modified by the acoustic-phonons at the pump fluence $6.5 \text{ mJ}\cdot\text{cm}^{-2}$. - The oscillations are observed at three different angles at the larger angle (compressive) side of the rocking curve.

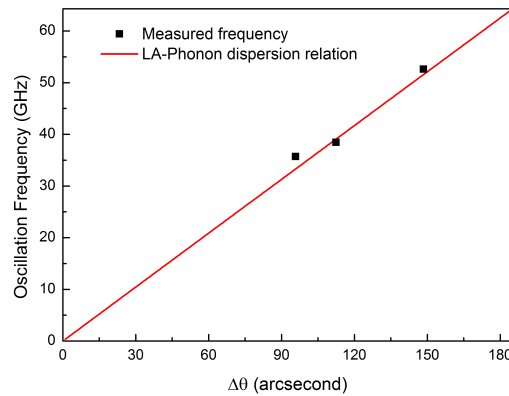


Figure 4.16: The measured phonon-dispersion relation. - The sound velocity is extracted as $4705 \text{ m}\cdot\text{s}^{-1}$, which is exactly the longitudinal acoustic phonon propagation speed.

4.5 Results of Time Resolved X-ray Diffraction

Here, one could follow the way as described in [34]. First one has to find out the experimental uncertainty in the measurements, which has two major sources: (i) the width of the FEL spectrum and, (ii) the spatial divergence of the beam. In this experiment, the silicon monochromator at the XPP beam line defines the X-ray spectrum and, according to the table 4.1 in section 4.2, the monochromator has an energy resolution of 1.4×10^{-4} . At an incident X-ray photon energy E of about 10.363 keV, the spectral width of the beam is ~ 1.45 eV. Differentiating the Bragg's equation one obtains:

$$\frac{\Delta\theta}{\Delta E} = \left| \frac{\Delta E}{E} \right| \tan\theta_B \quad (4.25)$$

The result is ~ 6 arcsecond, together with the ~ 1 arcsecond FEL beam divergence in the XPP beamline, the overall instrument angle resolution is less than 7 arcsecond. By inserting this number in the simulation, one immediately finds out that the instrument resolution cannot account for the damping. The other source would be the defects, mismatches of the lattice spacing, and residual stresses in the crystal. Figure 4.17 shows the rocking curve measured at room temperature. It is evident that the rocking curve is broader and asymmetric than that of an ideal GaAs crystal. By comparing the measured rocking curve with a Gaussian function of FWHM of 26 arcsecond, one can see that the shoulder on the larger angle side of the rocking curve indicates the existence of the residual strain. In fact, the $\text{Ga}_{1-x}\text{Mn}_x\text{As}$ samples investigated in the experiment are grown on (001) $\text{Al}_x\text{Ga}_{1-x}\text{As}$ substrate and, since the lattice constant of $\text{Al}_x\text{Ga}_{1-x}\text{As}$ is similar to that of GaAs which is smaller than $\text{Ga}_{1-x}\text{Mn}_x\text{As}$, the sample is compressively strained. Thus the diffraction is tending to emerge at the larger angle side of the rocking curve.

To compare the measured time-dependent X-ray diffraction intensity with the theory, the framework presented in section 4.3.2 is applied. First, one computes the rocking curve at different time delays using equations in section 4.3.2.2, and then convolves them with a Gaussian function of 26 arcsecond FWHM to account for the overall experimental resolution.

Theory and experiment are compared in figure 4.18 for two excitation fluences ~ 4 $\text{mJ}\cdot\text{cm}^{-2}$ and ~ 6.5 $\text{mJ}\cdot\text{cm}^{-2}$, respectively (parameters are listed in table 4.2). Here, an electron-phonon coupling time of ~ 10 ps was assumed, which does not differ too much from those of other standard polar semiconductors [30, 31].

In conclusion, the acoustic phonon modes in $\text{Ga}_{1-x}\text{Mn}_x\text{As}$ at room temperature were measured by time-dependent X-ray diffraction. The extracted sound velocity

4. ULTRAFAST DYNAMICS IN LASER-EXCITED DILUTED MAGNETIC SEMICONDUCTORS

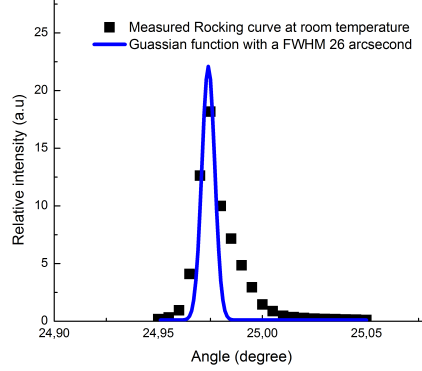


Figure 4.17: The rocking curve at room temperature. - The blue line is a fitting with a gaussian function, the FWHM is 26 arcsecond, the disagreement with the measured rocking curve indicated the localized compressively strains in the sample.

Table 4.2: Simulation parameters

Parameter	Value
FEL Energy	10.363 keV (3rd Harmonic)
Lattice constant	5.655×10^{-10} m
Heat capacity	$1.7024 \times 10^6 J \cdot m^{-3} \cdot K^{-1}$
Linear (thermal) expansion coefficient	$5.97 \times 10^{-6} K^{-1}$
Sound velocity (001)	$4705 m \cdot s^{-1}$
Bulk modulus	65 Gpa
Electron-phonon coupling time	10 ps

agrees well with those reported in the literature and, the simulations based on the extended Thomsen model and Takagi-Taupin equations are in excellent agreement with the measured data (reproducing both, the oscillation periods and amplitude). The extracted lattice heating time of ~ 10 ps suggests that at room temperature, $Ga_{1-x}Mn_xAs$ behaves as a “standard” polar semiconductor. The coupling time is important since it characterizes the time scale of the energy transfer from the carrier system to the lattice. The slight disagreement on the oscillation amplitude at the small angles may be due to the nonuniform response from the residual strain as shown in the right shoulder of the rocking curve.

4.5 Results of Time Resolved X-ray Diffraction

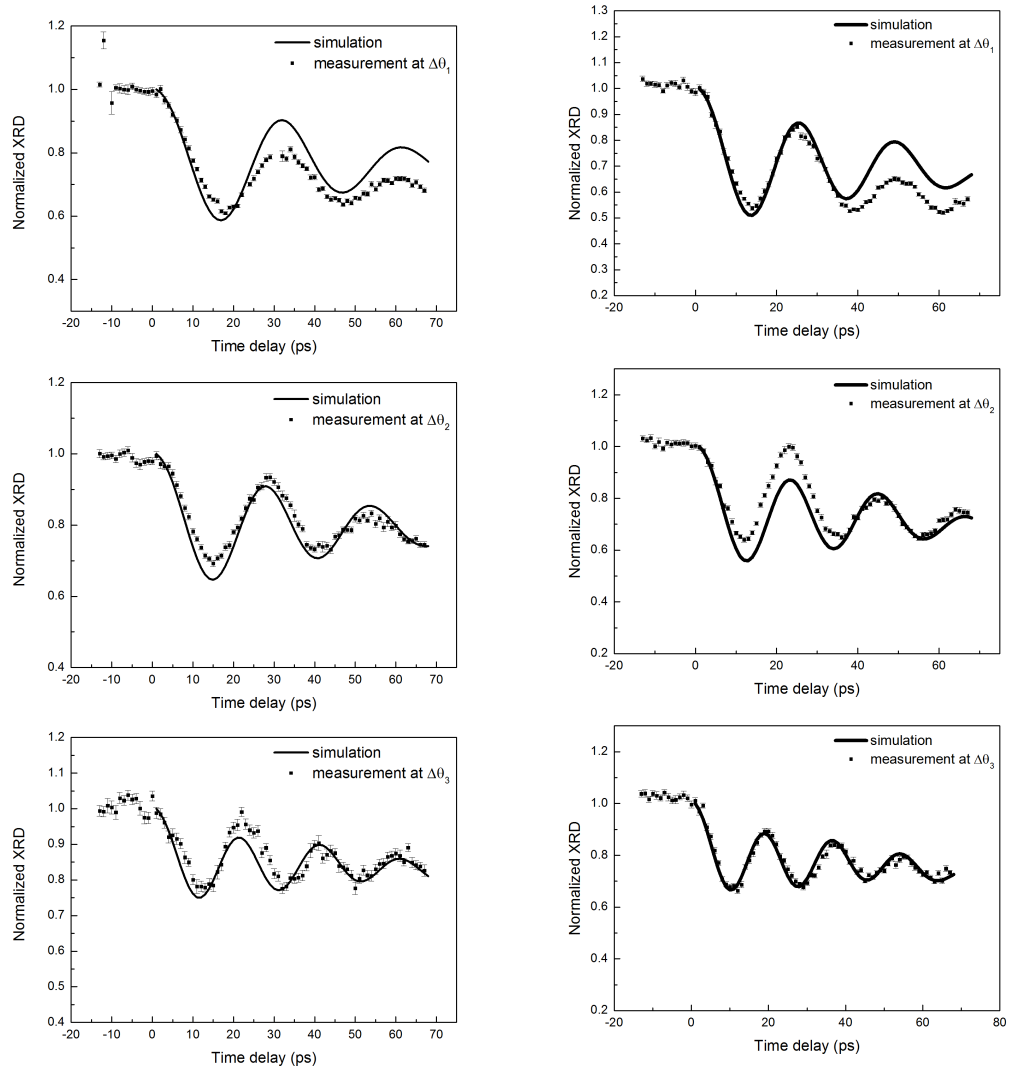


Figure 4.18: The simulations of the XRDs at fluence of 4 $\text{mJ}\cdot\text{cm}^{-2}$ and 6.5 $\text{mJ}\cdot\text{cm}^{-2}$. The agreement at higher angles is perfect, however at relatively lower angles, there are small amplitude disagreements.

4. ULTRAFAST DYNAMICS IN LASER-EXCITED DILUTED MAGNETIC SEMICONDUCTORS

(i). Low-Temperature Measurements

Time-dependent X-ray diffraction intensities measured at low temperatures (140 K, 100 K, 80 K, 60 K and 40 K) show quite different features as compared to those measured at room temperature. In order to understand the dynamics behind, one can take the room temperature data which have already been understood quite well as a basis for the comparison; in other words, one can start comparing, for instance, the room temperature data with those measured at 140 K at an angular position $\Delta\theta_3 = (0.049 \pm 0.03)$ deg, (or, $q_3 = (0.015 \pm 0.001)\frac{\pi}{a}$), see the figure 4.19. It is obvious that the first intensity minimum (the first half-period of the oscillation) has the same magnitude for both temperatures. Since the rate of the intensity decrease in this time regime is governed by the electron-phonon coupling that transfers the energy from the photoexcited carriers to the lattice, one can conclude that a strain with the same amplitude is generated at both temperatures. However, unlike at room temperature, the oscillations following the first intensity minimum are strongly damped. A fit with a damped-oscillator function of the form $I_q(t) = I_0 e^{-t/\tau} \cos(\omega_q t + \varphi)$ (see the figure 4.19), yields damping times of 35 ps and 11 ps for room temperature and 140 K, respectively.

These observations on the time-dependent X-ray diffracted intensity encountered at 140 K can not be explained in the framework of the Thomsen model. Thus, one needs to consider other interactions which are related to magnetic ordering and account for the absorption of the acoustic phonon energy. In $\text{Ga}_{1-x}\text{Mn}_x\text{As}$, when approaching the Curie temperature (T_C) from above, short-range magnetic order is built between nearby spin moments [98]. In equilibrium, these interactions are stored as potential energies which are related to the magnetic anisotropy. When acoustic phonons modulate the distance between the ions (no matter whether the strain is compressive or tensile), they transfer the energy to these localized spins which process around some local effective magnetic field related to the anisotropy field.

The derivative of the magnetization curve is shown in figure 4.20 (right), which clearly shows that below ~ 100 K, $\frac{\partial M}{\partial T}$ significantly increases, which is the sign that the sample starts to evolve into magnetic phase at this temperature.

The measured time scans at 100 K, 80 K, 60 K and 40 K are compared in figure 4.21. It is obvious that the measurement at 100 K, which is around Curie temperature, is substantially different from that of the others. The intensity minimum occurs latter by about 30 ps and the oscillations disappear. While at other temperatures, both above and below T_c (i.e. 140, 80, 60 and 40 K) the oscillations are damped due to the energy exchange between the phonons and localized magnetic moments (i.e. Mn moments), the evolution of the X-ray diffracted intensity at around T_C is related mainly to the energy

4.5 Results of Time Resolved X-ray Diffraction

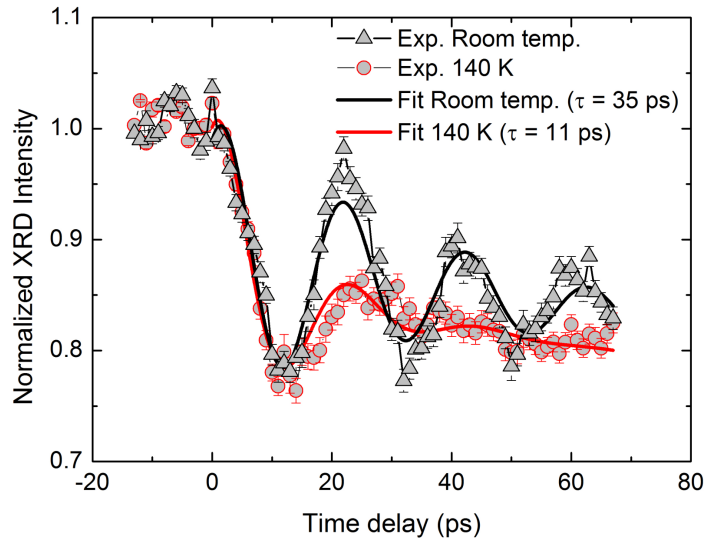


Figure 4.19: Comparison of the XRDs measured at 300 K and 140 K. - The pump fluence is $\sim 4 \text{ mJ}\cdot\text{cm}^{-2}$. The first drop of the XRD intensity has same amplitude.

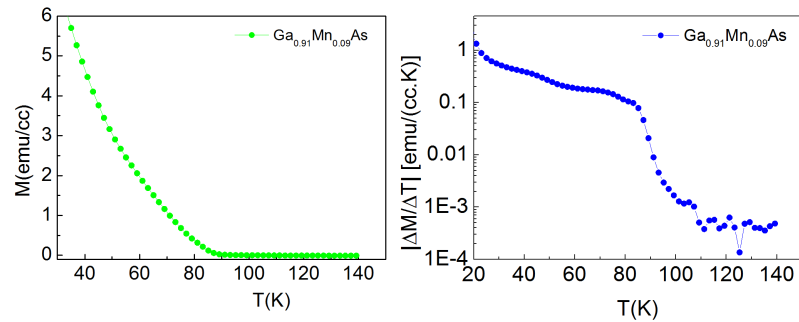


Figure 4.20: The magnetization-temperature curve of $\text{Ga}_{0.91}\text{Mn}_{0.09}\text{As}$ and its derivation. - The magnetic phase transition starts around at ~ 100 K.

4. ULTRAFAST DYNAMICS IN LASER-EXCITED DILUTED MAGNETIC SEMICONDUCTORS

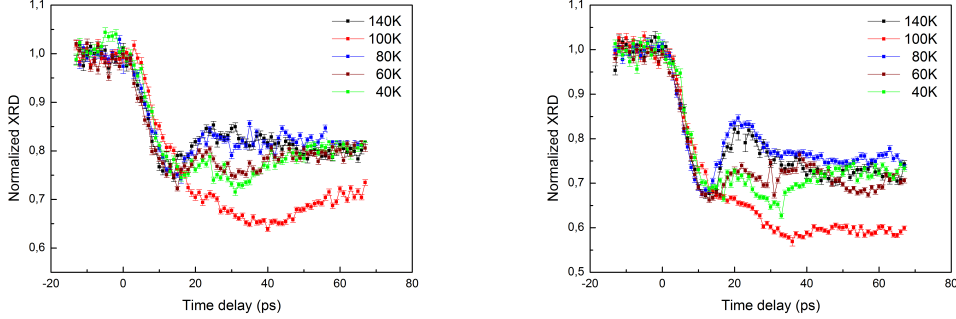


Figure 4.21: At certain angle $\Delta\theta_3$ (defined in the discussion of room temperature data). The curve measured at 100 K is obviously different with others.

exchange between the photoexcited carriers and the fluctuations of localized magnetic moments. It is already known that the temperature derivative of the resistivity $d\rho/dT$ of $\text{Ga}_{1-x}\text{Mn}_x\text{As}$ has a singularity at T_C [99, 100], which was attributed to the scattering of carriers from the localized-spin fluctuations. Since carriers play the main role in the generation of the coherent phonons, based on this observation, one can conclude that at around T_C , carriers exchange the energy with the spin fluctuations instead of only populating the acoustic phonon modes. This would explain the absence of the oscillations in the time-resolved intensity. However, this statement can not explain why the intensity minimum at around T_C is much lower than those at other temperatures. This anomaly can be explained by assuming that localized spins transfer their energies to the lattice not in terms of coherent phonons but in the form of heat (incoherent phonons), which expands the lattice further yielding thus a deeper minimum.

In summary, the time-resolved XRD was measured at different low temperatures 140 K, 100 K, 80 K, 60 K and 40 K. The deviation from the room-temperature measurements indicated the presence of new interactions at low temperatures. Especially, the unique lattice response at 100 K may be related to the critical behavior at around T_C , where the short-range spin correlation affects to a large extent the magnetic order (e.g. spin fluctuations).

4.6 Results of Time-Resolved Resonant X-ray Emission Measurements

The multidetection scheme applied in the experiment allows one to measure simultaneously both, X-ray diffraction and fluorescence. Here, the FEL photon energy needs to be tuned such that it drives a transition from the Ga K-level into the valence band. In order to choose the right energy, the first step is to measure the fluorescence Ga K edge spectrum.

The measured Ga K-edge X-ray emission as a function of incident X-ray photon energy is shown in figure 4.22. The spectrum is a convolution of the conduction band density of states of $\text{Ga}_{1-x}\text{Mn}_x\text{As}$, a Lorentzian profile of FWHM of 1.8 eV representing the core hole finite lifetime, and the energy width of the FEL radiation.

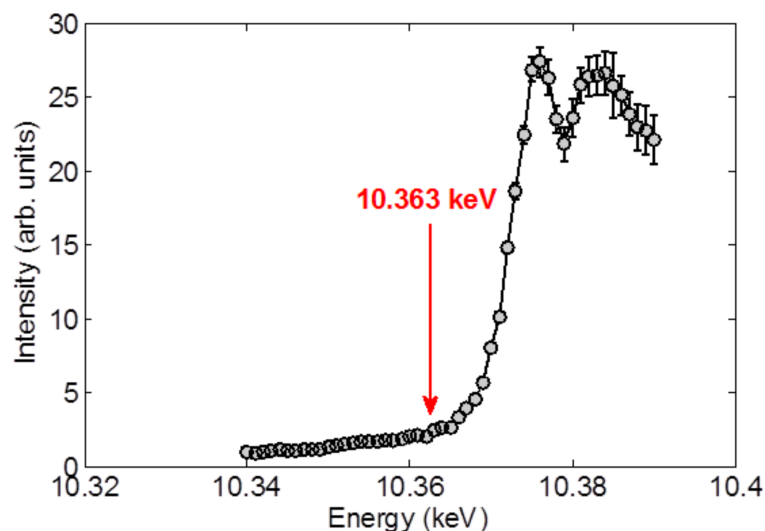


Figure 4.22: The measured Ga K-edge fluorescence spectrum. - The photon energy used to probe the valence band is labeled with red.

The increase of the emission intensity indicates that transitions from the core level 'see' the conduction band states (only the p-type states since the transition to the s-type states is forbidden by selection rules). Therefore, by choosing the LCLS photon energy just at the low energy shoulder (when the intensity just starts to increase, see the red arrow in figure 4.22), $E_{LCLS} = 10.363$ keV, one probes the top of the valence band (due to the finite lifetime of the core hole, the threshold energy separating the conduction band and valence band states has a jitter of ~ 1.8 eV).

4. ULTRAFAST DYNAMICS IN LASER-EXCITED DILUTED MAGNETIC SEMICONDUCTORS

From the Kramers-Heisenberg formula 4.19 presented in section 4.3.3 one can see that the emission intensity increases with increasing hole density (because when increasing the hole density, the probability of finding a hole in a particular valence band state, $1 - f(\varepsilon_k)$, gets larger). This property can be used to explain the data shown in figure 4.23

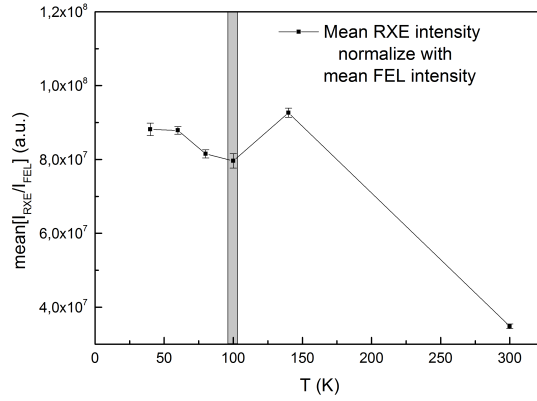


Figure 4.23: Integrated RXE intensity from $\text{Ga}_{1-x}\text{Mn}_x\text{As}$ (unperturbed) at different temperatures. - The RXE intensity increased by a factor of four; in addition, a small dip emerges at around T_C .

One can see that at room temperature the resonant X-ray emission (RXE) intensity is lower by more than a factor of four than that measured at lower temperatures. In addition, a small dip emerges at around T_C . Based on the Kramers-Heisenberg formula, this observations indicates that at lower temperatures the number of holes is larger than that at room temperature. This implies that the impurity band (i.e. the acceptor band introduced by the Mn doping) merges with the valence band of the host GaAs semiconductor (see the figure 4.24); when this happens, more electrons from the valence band populate the impurity level giving rise to more holes. A number of transport and optical measurements [101] support this conclusion.

Figure 4.25 shows the time-dependent RXE intensity measured at laser fluence of $6.5 \text{ mJ}\cdot\text{cm}^{-2}$. At room temperature, just after time zero, one observes an increase by $\sim 15\%$ in the intensity relative to the unperturbed part. This is due to the fact that $\sim 7 \times 10^{19} \text{ holes/cm}^3$ are generated in the valence band. It also indicates that the number of photoexcited holes is larger than that of the thermally activated holes, otherwise one would not see changes before and after the time zero. The structure of the time scan following laser excitation can be described in terms of recombination

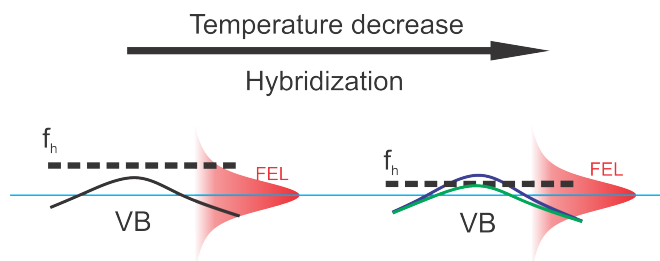


Figure 4.24: Schematic illustration of the Mn impurity band and the host GaAs valence band. - It is widely accepted that for low-doped insulating samples the Fermi energy lies in a narrow impurity band. When the doping increases ($x > 2\%$), the impurity band merges with the host semiconductor valence band. The valence band splitting (green and blue curve) is due to the p-d hybridization.

with the conduction band electrons and the valence band-to-impurity band transitions: since the RXE intensity is proportional to the hole occupation probability, its decrease indicates that the number of holes is reduced (recombination); a sudden increase of the intensity after ~ 15 and 30 ps indicates that hole population increases. This increase can not be related to the transition to the conduction band since the electrons can not cross the band gap without photoexcitation; the only plausible explanation is to assume that electrons in the valence band have been trapped in impurity band states increasing thus the number of holes, since they have similar energy levels.

At lower temperatures, on the other hand, the time-resolved RXE intensity is almost flat (the structures in the time scans cannot be resolved unambiguously due to the large statistical errors). This observation can be explained along the following lines: When the temperature decreases, the impurity band merges with the valence band and the number of holes generated by this process (i.e. without any laser excitation) is estimated to be $\sim 5 \times 10^{20} \text{cm}^{-3}$ (for an annealed sample, it can be estimated from an empirical relationship $T_C \sim p^{1/3}$ [102, 103]). This number, however, is much larger than the number of holes generated via optical excitation; therefore, enhancements on the RXE intensity are only a few percent, almost as the statistical error bars.

4.7 Summary

By applying the optical pump X-ray free-electron laser probe method, the interplay between lattice, carrier, and spin orders, which is strongly affected by temperature were measured in $\text{Ga}_{1-x}\text{Mn}_x\text{As}$. In this system, a complete knowledge of the spin interactions and dynamics as a function of temperature, especially around the Curie

4. ULTRAFAST DYNAMICS IN LASER-EXCITED DILUTED MAGNETIC SEMICONDUCTORS

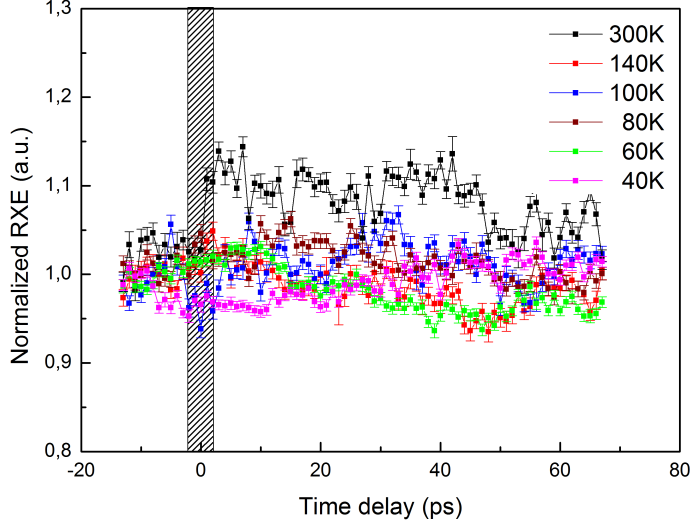


Figure 4.25: Time dependent resonant X-ray emission intensity at various temperatures. - The data were measured at the laser fluence of about $6.5 \text{ mJ}\cdot\text{cm}^{-2}$.

temperature (T_C) is still lacking [98]. In our measurements, the time-resolved X-ray diffraction and resonant X-ray emission were recorded at temperature ranging from 300 K down to 40 K, that means above and below T_C of $\text{Ga}_{1-x}\text{Mn}_x\text{As}$. The damping of lattice vibrations by the lattice-spin coupling [104] was directly observed, especially at around T_C , where, it is much more pronounced [98] due to the spin fluctuations. The reduction of the electron-phonon coupling time and extra expansion of the lattice spacing at around T_C were observed and attributed to the relaxation of spins in terms of energy-transfer to the lattice. In resonant X-ray emission (RXE) measurements, an increase of RXE intensity at low temperature was observed and explained by the merging of the hole Fermi level with decreasing temperature. Further, sudden enhancement of the RXE intensity following the photoexcitation was observed at room temperature as a results of increasing hole density by the photoexcitation. However, at low temperatures the density of holes produced by the impurities ($\sim 5 \times 10^{20} \text{ cm}^{-3}$) is larger than that due to the photoexcitation and the enhancement on the RXE intensity, in this case, is negligible.

Chapter 5

Summary and Outlook

In this thesis, the ultrafast dynamics in the polar semiconductor CdTe and the ferromagnetic semiconductor $\text{Ga}_{1-x}\text{Mn}_x\text{As}$ are investigated based on experiments with an optical laser as pump and an optical laser or X-ray free-electron laser, respectively, as probe.

In chapter 2, the basic ultrafast processes in carrier and lattice dynamics related to this work are described.

In chapter 3, the ultrafast carrier and lattice dynamics in CdTe after optical excitation with a femtosecond laser pulse centred at 780 nm has been investigated. In contrast to previous pump-probe reflectivity work on the coherent optical phonon measurement [12] and electron-phonon dynamics [13] carried out at low fluences only, the complex transient reflectivity changes in CdTe at the excitation fluences across a low fluence of $0.06 \text{ mJ}\cdot\text{cm}^{-2}$ to a high fluence $6.14 \text{ mJ}\cdot\text{cm}^{-2}$ were investigated. At low fluence, the phonon-plasmon coupling which is not observed in a previous study [12] is measured and discussed. At high fluence, the Stanton-Bailey model was extended to simulate the carrier dynamics. Together with the susceptibility computation framework proposed by H. Haug [63], the time-dependent reflectivity changes were simulated. Based on the simulation, ultrafast carrier and lattice dynamics which are strongly affected by the Coulomb screening and polar character of CdTe are understood very well. The transient reflectivity changes measured in the experiments explained as follows: pump-enhanced absorption is related to the band gap renormalization, and the ultrafast rise of reflectivity is related to the ultrafast excess-energy relaxation of hot carriers by phonon-plasmon coupling. Further, the Auger recombination of the intermediate polar semiconductor CdTe shows a N^2 (N is the carrier density) dependence rather than the normal N^3 dependence widely reported in the weakly polar semiconductor GaAs. This

5. SUMMARY AND OUTLOOK

is due to a Coulomb screening effect initially predicted by H. Haug, then widely applied to treat these kind of recombination processes. Moreover, the Auger recombination coefficient was observed to decline with increasing carrier density, which indicates the degeneration of carrier scattering cross sections by the Coulomb screening.

In chapter 4, by applying the optical-pump X-ray free-electron laser probe method, the interplay between lattice, carrier, and spin orders, which is strongly affected by temperature were measured in $\text{Ga}_{1-x}\text{Mn}_x\text{As}$. In this system, a complete knowledge of the spin interactions and dynamics as a function of temperature, especially around the Curie temperature (T_C) is still lacking [98]. In this work, the time-resolved X-ray diffraction and resonant X-ray emission were recorded at temperatures ranging from 300 K down to 40 K, that means above and below the T_C of $\text{Ga}_{1-x}\text{Mn}_x\text{As}$. The damping of lattice vibrations by the lattice-spin coupling [104] was directly observed, especially at around T_C , where, due to the spin fluctuations, it is much more pronounced [98]. The reduction of the electron-phonon coupling time and extra expansion of the lattice spacing at around T_C were observed and attributed to the relaxation of spins in terms of energy-transfer to the lattice. In resonant X-ray emission (RXE) measurements, an increase of RXE intensity at low temperature was observed and explained by the merging of the hole Fermi level with decreasing temperature. Further, sudden enhancement of the RXE intensity following photoexcitation was observed at room temperature as a result of increasing hole density by photoexcitation. However, at low temperatures, a large density of holes is produced due to the impurity band merges with the valence band (estimated to be $\sim 5 \times 10^{20} \text{ cm}^{-3}$). In this case, the enhancement on the RXE intensity by photoexcitation is negligible.

In the present optical pump-probe reflectivity measurements on CdTe, the carrier generation and detection are limited essentially to the pump and probe wavelength (at high fluence, on one hand, both the single and two-photon excitation channels have to be considered. On the other hand, the probe beam can only interact with those carriers already cooled down to the band edge). In future experiments, one could populate carriers at more specific positions on the bands and watch their dynamics in different band positions by using X-ray laser pulses of appropriate wavelengths.

In this thesis, time-resolved X-ray free-electron laser diffraction is proved to be a powerful tool to investigate the interaction between the acoustic phonon mode and the spin order in $\text{Ga}_{1-x}\text{Mn}_x\text{As}$. In future measurements, the observation of the interplay between the acoustic phonons and spins without the presence of carriers could be done. In order to achieve this, one can use a $\text{Ga}_{1-x}\text{Mn}_x\text{As}$ sample as the one in reference [80]. Here, the optical laser initially generates acoustic waves in a metal film which then

propagate through a GaAs substrate and enter the $\text{Ga}_{1-x}\text{Mn}_x\text{As}$ layer. Additionally, it might be interesting to study the interplay between optical phonon modes and the spin order. In this case, the jitter between optical laser and the free-electron laser needs to be reduced to less than the half period of the optical phonon. Another challenge is to further enhance the energy resolution of the resonant X-ray emission. With a much narrower energy width, the dynamics of the hole Fermi level may be measured accurately.

5. SUMMARY AND OUTLOOK

Appendix

Interaction of X-rays with matter

Generally speaking, X-rays interact with matter in two different ways, one is absorption (see the figure 1) and the another one is scattering. The absorption of X-rays is described by linear absorption coefficient μ . The relation between incident x-ray intensity and intensity at depth z is:

$$I(z) = I_0 e^{-\mu z} \quad (1)$$

The mechanism of X-ray absorption is shown in the figure 1.

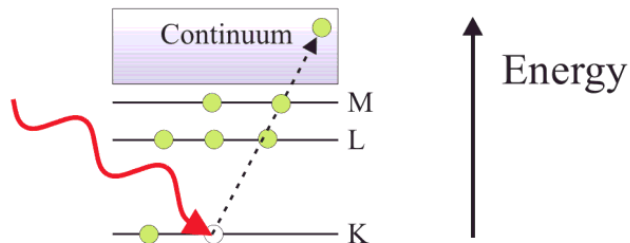


Figure 1: X-ray absorption mechanism. - Electron is excited from inner shell to the continuum states after absorbing a X-ray photon. This process is also called photoelectric absorption.

After absorption of X-ray photon, the matter relax via the fluorescence emission or Auger decay: absorption of X-ray photon leads to the inner shell vacancies, which can be filled by the higher energy level electrons via fluorescence emission (see the figure 2) or Auger decay (see the figure 3).

The scattering of the X-ray can be divided into two categories, the elastic scattering (Thomsen scattering), and the inelastic scattering (Compton scattering), depends on

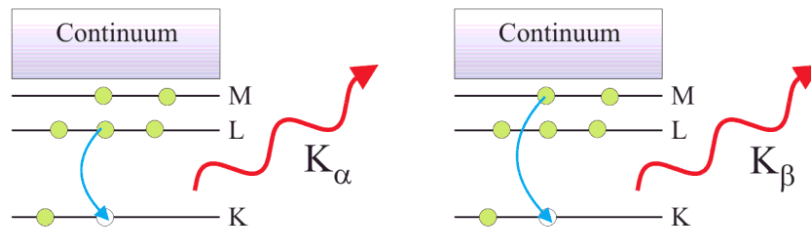


Figure 2: X-ray fluorescence generation. - The K_{α} and K_{β} fluorescence are induced by electron transition from L-shell to K-shell and M-shell to K-shell, respectively [105].

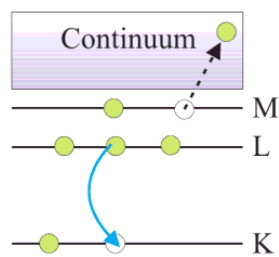


Figure 3: X-ray Auger decay. - The electron filling the K-shell vacancy transfers excess binding energy to another electron, which is then excited [105].

whether the X-ray phonon energy is conserved or not after scattering.

The inelastic scattering (Compton scattering) mechanism is shown in the figure 4.

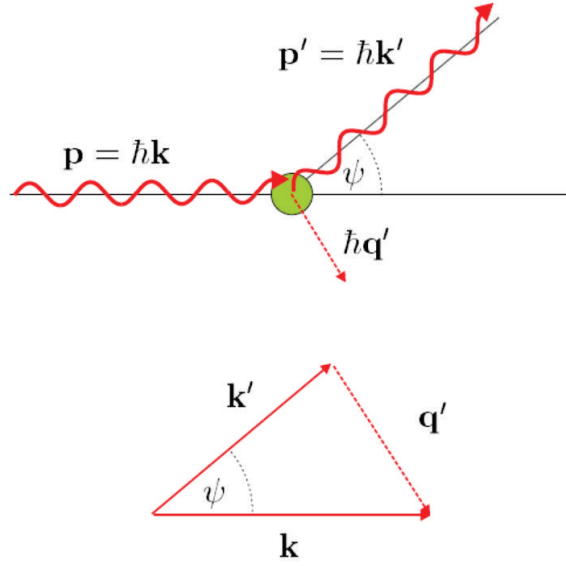


Figure 4: Principle of the inelastic scattering (Compton scattering). - Lower graph shows the momentum conservation requirement [105].

In the measurement described in Chapter 4, both X-ray diffraction and resonant X-ray emission technique are applied.

X-ray diffraction is one kind of coherent elastic scattering. It is usually expressed by Bragg's law or Laue's condition, which are physically equal. However, Bragg's law is described in real space, and Laue's condition is described in the reciprocal space, see the figure 5 left and right, respectively. In analysis of rocking curve, Laue's condition is more convenient. According to Laue condition $Q = G$, detune the crystal away from the Bragg angle of a angle $\Delta\theta$ then $Q \neq G$. The change in diffraction plane is given by [32]:

$$\begin{aligned}
 Q &= 2k \sin(\theta_B + \Delta\theta) \\
 &\approx 2k[\sin\theta_B + \cos\theta_B \Delta\theta] \\
 &= G + 2k \cos\theta_B \Delta\theta
 \end{aligned}
 \tag{2}$$

Thus the momentum mismatch q is:

$$\begin{aligned}
 q &= 2k\cos\theta_B\Delta\theta \\
 &= 2k\sin\theta_B\frac{\cos\theta_B}{\sin\theta_B}\Delta\theta \\
 &= \frac{G_{hkl}}{\tan\theta_B}\Delta\theta
 \end{aligned} \tag{3}$$

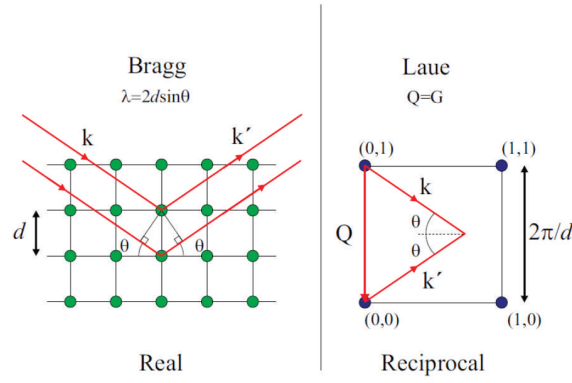


Figure 5: Diffraction: Bragg and Laue. - Bragg's law and Laue's condition [105].

The descriptions of X-ray fluorescence emission in figure 2 is rather qualitatively, to understand them in quantity, one needs to start from the basic Hamiltonian of X-ray interaction with matter.

(i). The interaction Hamiltonian of X-ray interaction with matter

The Hamiltonian of X-ray interacting with matter can be written in three components, the Hamiltonian of the X-ray electromagnetic field, the Hamiltonian of the atom in the matter, and the Hamiltonian of interactions.

$$H_{total} = H_{EM} + H_{atom} + H_{interaction} \tag{4}$$

A electromagnetic field can be represented by a set of plane waves. The electromagnetic field of a plane wave has a well known classical expression:

$$A(\mathbf{r}, t) = \frac{1}{2\sqrt{V}} \sum_k \left[A_{k,\lambda} e^{i(kx - \omega_k t)} \cdot \vec{y} + A_{k,\lambda}^* e^{i(kx - \omega_k t)} \cdot \vec{y} \right] \tag{5}$$

The vector \vec{y} means that the direction of $A(\mathbf{r}, t)$ is perpendicular to the propagation direction \vec{x} . The electric field $E(x, t)$ and the magnetic field $B(x, t)$ are:

$$E(x, t) = -\frac{\partial}{\partial t}A(\mathbf{r}, t) \quad (6)$$

$$B(x, t) = \nabla \times A(\mathbf{r}, t) \quad (7)$$

The Hamiltonian of the the electromagnetic field can be derived by energy quantization of the electromagnetic field. And it is required to fulfill the eigenvalue equations as follows:

$$H_{EM}\psi = \varepsilon\psi = \sum_{k,\lambda} \hbar\omega_k\psi \quad (8)$$

with ε the energy of the electromagnetic field given by:

$$\varepsilon = \frac{1}{8\pi} \int_v [|E(x, t)|^2 + |B(x, t)|^2] \quad (9)$$

By solving equations 5 to 8, we get:

$$\varepsilon = \frac{1}{4\pi} V \sum_{k,\lambda} \frac{\omega_k^2}{c^2} [A_{k,\lambda}A_{k,\lambda}^* + A_{k,\lambda}^*A_{k,\lambda}] \quad (10)$$

We can express $A_{k,\lambda}$ by the variable $a_\lambda(k)$:

$$A_{k,\lambda} = \frac{\sqrt{4\pi\hbar c^2}}{\sqrt{V}} \frac{1}{\sqrt{2\omega_k}} a_\lambda(k) \quad (11)$$

thus equation 10 became:

$$\varepsilon = \sum_{k,\lambda} \frac{1}{2} \hbar\omega_k [a_\lambda^*(k)a_\lambda(k) + a_\lambda^*(k)a_\lambda(k)] \quad (12)$$

insert this into 8, we get:

$$H_{EM}\psi = \sum_{k,\lambda} \frac{1}{2} \hbar\omega_k [a_\lambda^*(k)a_\lambda(k) + a_\lambda^*(k)a_\lambda(k)] \psi \quad (13)$$

By using the creation and annihilation operators $b_\lambda^+(k)$ and $b_\lambda(k)$ [106] instead of the variable $a_\lambda^*(k)$ and $a_\lambda(k)$, finally we get the Hamiltonian:

$$H_{EM} = \sum_{k,\lambda} \hbar\omega_k b_\lambda^\dagger(k) b_\lambda(k) \quad (14)$$

And the electromagnetic operator:

$$A_{k,\lambda} = \frac{\sqrt{4\pi\hbar c^2}}{\sqrt{V}} \frac{1}{\sqrt{2\omega_k}} b_\lambda(k) \quad (15)$$

Since the X-ray actually interact with the electrons in the atom, the Hamiltonian can be written as the combination of the kinetic energy and the Coulomb potential of the electron:

$$H_{atom} = \sum_i \left[\frac{P_i}{2m} + V(r_i) \right] \quad (16)$$

The Hamiltonian describes the interaction between atoms and the electromagnetic field is treated as a small perturbation, the first order perturbation is:

$$H' = \frac{e}{m} \sum_i P_i \cdot A(\mathbf{r}) + \frac{e\hbar}{m} \sum_i S_i \cdot (\nabla \times A(\mathbf{r})) \quad (17)$$

The first term describes the electron momentum interacting with the electric field, and the second term describes the electron spin interacting with the magnetic field. The second term usually can be neglected, because the amplitude ratio of magnetic to charge scattering for a single electron is [105]:

$$\frac{A_{magnetic}}{A_{charge}} = \left(\frac{\hbar\omega}{mc^2} \right) \quad (18)$$

In our experiment, by using the FEL with a photon energy of 10.363 keV, we get this ratio ≈ 0.011 . Therefore we can neglect the magnetic scattering contribution in the later description.

In the second order perturbation, a new term is raising:

$$H'' = \frac{e^2}{2m} \sum_i A^2(\mathbf{r}_i) \quad (19)$$

$A(\mathbf{r})$ is linear in the creation and annihilation operators $b_\lambda^\dagger(k)$ and $b_\lambda(k)$, see equation 15. It follows that it can either create a photon or annihilate a photon, thus the

quadratic power in $A(\mathbf{r})$ means first annihilate a photon then create a photon with out changing the photon energy. This term therefore describes the elastic Thomson scattering when the final state and initial states are equal and inelastic Compton scattering when these states are not equal [107].

Finally, the interaction Hamiltonian can be written as:

$$H_{interaction} = \frac{e}{m} \sum_i P_i \cdot A(\mathbf{r}) + \frac{e^2}{2m} \sum_i A^2(\mathbf{r}_i) \quad (20)$$

Thus the overall Hamiltonian is:

$$H_{total} = \sum_i \left[\frac{P_i}{2m} + V(r_i) \right] + \sum_{k,\lambda} \hbar\omega_k b_\lambda^+(k) b_\lambda(k) + H_{interaction} \quad (21)$$

(ii). From the Fermi's Golden Rule to the Kramers-Heisenberg Equation

The Fermi's Golden rule states that the transition probability W_{fermi} between a system in its initial state B and final state A:

$$W_{fermi} = \frac{2\pi}{\hbar} |\langle \phi_a | T | \phi_b \rangle|^2 \delta(E_a - E_b - \hbar\omega) \quad (22)$$

T is the transition operator, which relates to the overall and interaction Hamiltonian with the Lippmann-Schwinger equation:

$$T = H_{interaction} + \left(\frac{H_{interaction}}{E_b - H_{total} + i\Gamma/2} \right) T \quad (23)$$

Where Γ is the life time of the mediate state.

The resonant X-ray emission process involves two photons (absorb one photon and emit one), therefore it has to relate to the $A^2(\mathbf{r})$ term, which is a second order optical process according to equation 20.

The differential scattering cross section can be obtained by calculating equation 22 for a specific solid angle and integrate over all the final states:

$$\frac{\partial^2 \sigma}{\partial \Omega \partial \omega_2} = r_0^2 \left(\frac{\omega_2}{\omega_1} \right) |C_1 + C_2 + C_3|^2 \times \delta(E_a - E_b - \hbar\omega) \quad (24)$$

$$C_1 = (e_1 \cdot e_2) \langle b | e^{-ik \cdot r} | a \rangle$$

$$C_2 = \frac{1}{m} \sum_i \frac{\langle b | (e_2 \cdot \mathbf{p}) e^{-ik_2 \cdot r} | i \rangle \langle i | (e_1 \cdot \mathbf{p}) e^{-ik_1 \cdot r} | a \rangle}{E_a - E_i + \hbar\omega_1 + i\Gamma/2}$$

$$C_3 = \frac{1}{m} \sum_i \frac{\langle b | (e_1 \cdot \mathbf{p}) e^{-ik_1 \cdot r} | i \rangle \langle i | (e_2 \cdot \mathbf{p}) e^{-ik_2 \cdot r} | a \rangle}{E_a - E_i + \hbar\omega_2 + i\Gamma/2}$$

This formula was first derived by Kramers and Heisenberg, thus is called Kramers-Heisenberg formula. r_0 is the Thomson scattering length, e_1 and e_2 are unit polarization vectors for the incoming and emitted photons. The first term C_1 of formula 24 relates to the A^2 term thus gives both elastic Thomson scattering and inelastic Compton scattering as mentioned above (equation 20). In the horizontal plane at 90° respect to the incident X-ray, $|e_1 \cdot e_2|$ is zero, thus these two scattering processes are suppressed. The second term C_2 involves the $P \cdot A$ contribution excited via the intermediate state $|i\rangle$. It is a resonant component when the incident X-ray photon energy is equal to $E_a - E_i$. The third term C_3 requires that the energy of the initial state is lower than the final state, which is only possible in excited atoms. Therefore C_3 describes the stimulated emission.

References

- [1] M.V. LEBEDEV, O.V. MISOCHKO, T. DEKORSY, AND N. GEORGIEV. **On the nature of “coherent artifact”**. *Journal of Experimental and Theoretical Physics*, **100**:272–282, 2005. x, 49
- [2] S.J. PEARTON, C.R. ABERNATHY, D.P. NORTON, A.F. HEBARD, Y.D. PARK, L.A. BOATNER, AND J.D. BUDAI. **Advances in wide bandgap materials for semiconductor spintronics**. *Materials Science and Engineering: R: Reports*, **40**(4):137 – 168, 2003. 1
- [3] T. DIETL, H. OHNO, F. MATSUKURA, J. CIBERT, AND D. FERRAND. **Zener Model Description of Ferromagnetism in Zinc-Blende Magnetic Semiconductors**. *Science*, **287**:1019–1022, 2000. 1, 3, 64
- [4] EDITORIAL. **More than just room temperature**. *Nature Materials*, **9**:951, 2010. 1, 3
- [5] D. CHIBA, Y. SATO, T. KITA, F. MATSUKURA, AND H. OHNO. **Current-Driven Magnetization Reversal in a Ferromagnetic Semiconductor (Ga, Mn)As/GaAs/(Ga, Mn)As Tunnel Junction**. *Phys. Rev. Lett.*, **93**:216602, Nov 2004. 1
- [6] S. MARK, P. DÜRRENFELD, K. PAPPERT, L. EBEL, K. BRUNNER, C. GOULD, AND L. W. MOLENKAMP. **Fully Electrical Read-Write Device Out of a Ferromagnetic Semiconductor**. *Phys. Rev. Lett.*, **106**:057204, Jan 2011. 1
- [7] C ERTLER, A MATOS-ABIAGUE, M GMITRA, M TUREK, AND J FABIAN. **Perspectives in spintronics: magnetic resonant tunneling, spin-orbit coupling, and GaMnAs**. *Journal of Physics: Conference Series*, **129**(1):012021, 2008. 1

REFERENCES

- [8] D.A. CUSANO. **CdTe solar cells and photovoltaic heterojunctions in II-VI compounds.** *Solid-State Electronics*, **6**(3):217 – 218, 1963. 2, 36
- [9] C.S. FERKIDES, U. BALASUBRAMANIAN, R. MAMAZZA, V. VISWANATHAN, H. ZHAO, AND D.L. MOREL. **CdTe thin film solar cells: device and technology issues.** *Solar Energy*, **77**(6):823 – 830, 2004. `je:itlejThin Film PVj/ce:itlej`. 2, 36
- [10] ADRIANO COLA AND ISABELLA FARELLA. **The polarization mechanism in CdTe Schottky detectors.** *Applied Physics Letters*, **94**(10):102113, 2009. 2, 36
- [11] M. SCHALL AND P.U. JEPSEN. **Ultrafast dynamics of extremely hot carriers in ZnTe and CdTe probed in the far infrared.** In *Quantum Electronics and Laser Science Conference, 2001. QELS '01. Technical Digest. Summaries of Papers Presented at the*, page 255, 2001. 2, 36
- [12] KUNIE ISHIOKA, MASAHIRO KITAJIMA, JUN IRISAWA, YOICHIRO HIRONAKA, KIMINORI USHIDA, AND KAZUTAKA G. NAKAMURA. **Amplitude Saturation of Coherent Phonon Excited by Field Screening in CdTe.** *Japanese Journal of Applied Physics*, **45**(12):9111–9114, 2006. 2, 29, 36, 47, 91
- [13] K.T. TSEN. *Ultrafast Physical Processes in Semiconductors*. Number Bd. 67 in *Semiconductors and Semimetals*. Academic Press, 2001. 2, 36, 57, 91
- [14] FAUSTO ROSSI AND TILMANN KUHN. **Theory of ultrafast phenomena in photoexcited semiconductors.** *Rev. Mod. Phys.*, **74**:895–950, Aug 2002. 2, 36
- [15] A. V. KUZNETSOV AND C. J. STANTON. **Coherent phonon oscillations in GaAs.** *Phys. Rev. B*, **51**:7555–7565, Mar 1995. 2, 29, 31, 36, 50
- [16] U. HOHENESTER, P. SUPANCIC, P. KOCEVAR, X. Q. ZHOU, W. KÜTT, AND H. KURZ. **Subpicosecond thermalization and relaxation of highly photoexcited electrons and holes in intrinsic and *p*-type GaAs and InP.** *Phys. Rev. B*, **47**:13233–13245, May 1993. 2, 35, 36
- [17] C. V. SHANK, R. L. FORK, R. F. LEHENY, AND JAGDEEP SHAH. **Dynamics of Photoexcited GaAs Band-Edge Absorption with Subpicosecond Resolution.** *Phys. Rev. Lett.*, **42**:112–115, Jan 1979. 2, 36

-
- [18] R. ULBRICH. **Energy Relaxation of Photoexcited Hot Electrons in GaAs.** *Phys. Rev. B*, **8**:5719–5727, Dec 1973. 2, 36
- [19] C. L. PETERSEN AND S. A. LYON. **Observation of hot-electron energy loss through the emission of phonon-plasmon coupled modes in GaAs.** *Phys. Rev. Lett.*, **65**:760–763, Aug 1990. 2, 36, 60
- [20] THOMAS ELSAESSER, JAGDEEP SHAH, LUCIO ROTA, AND PAOLO LUGLI. **Initial thermalization of photoexcited carriers in GaAs studied by femtosecond luminescence spectroscopy.** *Phys. Rev. Lett.*, **66**:1757–1760, Apr 1991. 2, 16, 36
- [21] H. OHNO, A. SHEN, F. MATSUKURA, A. OIWA, A. ENDO, S. KATSUMOTO, AND Y. IYE. **(Ga,Mn)As: A new diluted magnetic semiconductor based on GaAs.** *Applied Physics Letters*, **69**(3):363–365, 1996. 3, 65
- [22] H. OHNO. **Making Nonmagnetic Semiconductors Ferromagnetic.** *Science*, **281**(5379):951–956, 1998. 3
- [23] J. P. ZAHN, A. GAMOURAS, S. MARCH, X. LIU, J. K. FURDYNA, AND K. C. HALL. **Ultrafast studies of carrier and magnetization dynamics in GaMnAs.** *Journal of Applied Physics*, **107**(3):033908, 2010. 3, 61
- [24] A. V. KIMEL, G. V. ASTAKHOV, G. M. SCHOTT, A. KIRILYUK, D. R. YAKOVLEV, G. KARCZEWSKI, W. OSSAU, G. SCHMIDT, L. W. MOLENKAMP, AND TH. RASING. **Picosecond Dynamics of the Photoinduced Spin Polarization in Epitaxial (Ga,Mn)As Films.** *Phys. Rev. Lett.*, **92**:237203, Jun 2004. 3, 61
- [25] J. WANG, I. COTOROS, K. M. DANI, X. LIU, J. K. FURDYNA, AND D. S. CHEMLA. **Ultrafast Enhancement of Ferromagnetism via Photoexcited Holes in GaMnAs.** *Phys. Rev. Lett.*, **98**:217401, May 2007. 3, 61
- [26] Y. HASHIMOTO, S. KOBAYASHI, AND H. MUNEKATA. **Photoinduced Precession of Magnetization in Ferromagnetic (Ga,Mn)As.** *Phys. Rev. Lett.*, **100**:067202, Feb 2008. 3, 61
- [27] C. S. KING, J. ZEMEN, K. OLEJN L. HORÁK, J. A. HAIGH, V. NOVÁK, A. IRVINE, J. KUČERA, V. HOLÝ, R. P. CAMPION, B. L. GALLAGHER, AND T. JUNGWIRTH. **Strain control of magnetic anisotropy in (Ga,Mn)As microbars.** *Phys. Rev. B*, **83**:115312, Mar 2011. 3

REFERENCES

- [28] D. M. WANG, Y. H. REN, X. LIU, J. K. FURDYNA, M. GRIMSDITCH, AND R. MERLIN. **Light-induced magnetic precession in (Ga,Mn)As slabs: Hybrid standing-wave Damon-Eshbach modes.** *Phys. Rev. B*, **75**:233308, Jun 2007. 3, 61
- [29] Y. MITSUMORI, A. OIWA, T. ŚLUPINSKI, H. MARUKI, Y. KASHIMURA, F. MINAMI, AND H. MUNEKATA. **Dynamics of photoinduced magnetization rotation in ferromagnetic semiconductor p -(Ga,Mn)As.** *Phys. Rev. B*, **69**:033203, Jan 2004. 3, 61
- [30] CHRISTOPH ROSE-PETRUCK, RALPH JIMENEZ, TING GUO, ANDREA CAVALLERI, CRAIG W. SIDERS, FERENC RKSİ, JEFF A. SQUIER, BARRY C. WALKER, KENT R. WILSON, AND BARTY CHRISTOPHER P. J. **Picosecond-milliångstrom lattice dynamics measured by ultrafast X-ray diffraction.** *Nature*, **398**:310–312, 1999/03/25/print. 3, 61, 81
- [31] MATTHEW F. DECAMP, DAVID A. REIS, DAVID M. FRITZ, PHILIP H. BUCKSBAUM, ERIC M. DUFRESNE, AND ROY CLARKE. **X-ray synchrotron studies of ultrafast crystalline dynamics.** *Journal of Synchrotron Radiation*, **12**(2):177–192, Mar 2005. 3, 61, 81
- [32] A. M. LINDENBERG. *Ultrafast Lattice Dynamics in Solids Probed by Time-resolved X-ray Diffraction.* PhD thesis, University of California, 2001. 3, 61, 67, 97
- [33] D. A. REIS, M. F. DECAMP, P. H. BUCKSBAUM, R. CLARKE, E. DUFRESNE, M. HERTLEIN, R. MERLIN, R. FALCONE, H. KAPTEYN, M. M. MURNANE, J. LARSSON, TH. MISSALLA, AND J. S. WARK. **Probing Impulsive Strain Propagation with X-Ray Pulses.** *Phys. Rev. Lett.*, **86**:3072–3075, Apr 2001. 3, 61, 69
- [34] A. M. LINDENBERG, I. KANG, S. L. JOHNSON, T. MISSALLA, P. A. HEIMANN, Z. CHANG, J. LARSSON, P. H. BUCKSBAUM, H. C. KAPTEYN, H. A. PADMORE, R. W. LEE, J. S. WARK, AND R. W. FALCONE. **Time-Resolved X-Ray Diffraction from Coherent Phonons during a Laser-Induced Phase Transition.** *Phys. Rev. Lett.*, **84**:111–114, Jan 2000. 3, 61, 69, 79, 81
- [35] HANFEI YAN, JÖRG MASER, ALBERT MACRANDER, QUN SHEN, STEFAN VOGT, G. BRIAN STEPHENSON, AND HYON CHOL KANG. **Takagi-Taupin descrip-**

- tion of x-ray dynamical diffraction from diffractive optics with large numerical aperture.** *Phys. Rev. B*, **76**:115438, Sep 2007. 3, 61, 69
- [36] SOO HEYONG LEE. *Time-Resolved X-ray Measurements of Energy Relaxation in Ultrafast Laser Excited Semiconductors*. PhD thesis, University of Michigan, 2006. 3, 61, 69
- [37] B.K. RIDLEY. *Quantum Processes in Semiconductors*. Oxford Science Publications. Oxford University Press, USA, 2000. 9, 16, 17, 21, 29
- [38] P.Y. YU AND M. CARDONA. *Fundamentals of Semiconductors: Physics and Materials Properties*. Graduate Texts in Physics. Springer, 2010. 9, 10, 11, 17, 21
- [39] N.W. ASHCROFT AND N.D. MERMIN. *Solid state physics*. Science: Physics. Saunders College, 1976. 9
- [40] J.D. JACKSON. *Classical Electrodynamics*. John Wiley & Sons, 1998. 11
- [41] C. J. STANTON, D. W. BAILEY, AND K. HESS. **Femtosecond-pump, continuum-probe nonlinear absorption in GaAs.** *Phys. Rev. Lett.*, **65**:231–234, Jul 1990. 16
- [42] F. X. CAMESCASSE, A. ALEXANDROU, AND D. HULIN. **Ultrafast Electron Relaxation through Coulomb Collisions in GaAs.** *physica status solidi (b)*, **204**(1):293–299, 1997. 16
- [43] F. KADLEC, H. NĚMEC, AND P. KUŽEL. **Optical two-photon absorption in GaAs measured by optical-pump terahertz-probe spectroscopy.** *Phys. Rev. B*, **70**:125205, Sep 2004. 16, 35, 55
- [44] J. SINGH. *Electronic and Optoelectronic Properties of Semiconductor Structures*. Cambridge University Press, 2003. 17, 26
- [45] D. BIMBERG, I. EISELE, W. FUHS, H. KAHLERT, N. KARL, O. MADELUNG, AND H. WEISS. *Special Systems and Topics. Comprehensive Index for III/17 a...i / Spezielle Systeme und Themen. Gesamtregister für III/17 a...i*. Number Bd. 1 in Landolt-Börnstein: Numerical Data and Functional Relationships in Science and Technology - New Series / Condensed Matter. Springer, 1985. 19
- [46] J. SHAH. *Ultrafast Spectroscopy of Semiconductors and Semiconductor Nanostructures*. Springer Series in Solid-State Sciences. Springer, 1999. 23

REFERENCES

- [47] JAGDEEP SHAH, BENOIT DEVEAUD, T. C. DAMEN, W. T. TSANG, A. C. GOSSARD, AND P. LUGLI. **Determination of intervalley scattering rates in GaAs by subpicosecond luminescence spectroscopy.** *Phys. Rev. Lett.*, **59**:2222–2225, Nov 1987. 23
- [48] C. J. STANTON AND D. W. BAILEY. **Rate equations for the study of femtosecond intervalley scattering in compound semiconductors.** *Phys. Rev. B*, **45**:8369–8377, Apr 1992. 26, 53
- [49] N. F. MOTT. **Metal-Insulator Transition.** *Rev. Mod. Phys.*, **40**:677–683, Oct 1968. 29, 39
- [50] G. C. CHO, W. KÜTT, AND H. KURZ. **Subpicosecond time-resolved coherent-phonon oscillations in GaAs.** *Phys. Rev. Lett.*, **65**:764–766, Aug 1990. 29, 35
- [51] LEEOR KRONIK AND YORAM SHAPIRA. **Surface photovoltage phenomena: theory, experiment, and applications.** *Surface Science Reports*, **37**(1-5):1 – 206, 1999. 29
- [52] A. FORCHEL, H. SCHWEIZER, AND G. MAHLER. **Optical Properties of Fast-Diffusing Solid-State Plasmas.** *Phys. Rev. Lett.*, **51**:501–504, Aug 1983. 35
- [53] MUNEAKI. HASE, MASAHIRO. KITAJIMA, ANCA MONIA. CONSTANTINESCU, AND HRVOJE. PETEK. **The birth of a quasiparticle in silicon observed in time-frequency space.** *Nature*, **426**:51–54, 2003. 35, 48
- [54] J. D. LEE AND MUNEAKI HASE. **Coherent Optical Control of the Ultrafast Dephasing of Phonon-Plasmon Coupling in a Polar Semiconductor Using a Pulse Train of Below-Band-Gap Excitation.** *Phys. Rev. Lett.*, **101**:235501, Dec 2008. 35
- [55] A. LEITENSTORFER, S. HUNSCHE, J. SHAH, M. C. NUSS, AND W. H. KNOX. **Femtosecond Charge Transport in Polar Semiconductors.** *Phys. Rev. Lett.*, **82**:5140–5143, Jun 1999. 35
- [56] T. DEKORSY, H. AUER, C. WASCHKE, H. J. BAKKER, H. G. ROSKOS, H. KURZ, V. WAGNER, AND P. GROSSE. **Emission of Submillimeter Electromagnetic Waves by Coherent Phonons.** *Phys. Rev. Lett.*, **74**:738–741, Jan 1995. 35

-
- [57] P.M. FAUCHET. **Enhanced sensitivity of time-resolved reflectivity measurements near Brewster's angle.** *Quantum Electronics, IEEE Journal of*, **25**(5):1072–1078, may 1989. 37
- [58] GREGORY H. WANNIER. **The Structure of Electronic Excitation Levels in Insulating Crystals.** *Phys. Rev.*, **52**:191–197, Aug 1937. 40
- [59] ELIAS BURSTEIN. **Anomalous Optical Absorption Limit in InSb.** *Phys. Rev.*, **93**:632–633, Feb 1954. 41
- [60] N. G. NILSSON. **Empirical approximations for the Fermi energy in a semiconductor with parabolic bands.** *Applied Physics Letters*, **33**(7):653–654, 1978. 41
- [61] L. BAÑYAI AND S. W. KOCH. **A simple theory for the effects of plasma screening on the optical spectra of highly excited semiconductors.** *Zeitschrift fr Physik B Condensed Matter*, **63**:283–291, 1986. 10.1007/BF01303807. 42
- [62] S. S. PRABHU AND A. S. VENGURLEKAR. **Dynamics of the pump-probe reflectivity spectra in GaAs and GaN.** *Journal of Applied Physics*, **95**(12):7803–7812, 2004. 43, 52, 53
- [63] H. HAUG AND S.W. KOCH. *Quantum Theory of the Optical and Electronic Properties of Semiconductors.* World Scientific, 2009. 43, 45, 60, 91
- [64] MARIJN A. M. VERSTEEGH, TIM KUIS, H. T. C. STOOF, AND JAAP I. DIJKHUIS. **Ultrafast screening and carrier dynamics in ZnO: Theory and experiment.** *Phys. Rev. B*, **84**:035207, Jul 2011. 45
- [65] CHARLES C. KIM AND S. SIVANANTHAN. **Modeling the optical dielectric function of II-VI compound CdTe.** *Journal of Applied Physics*, **78**(6):4003–4010, 1995. 45
- [66] SADA O ADACHI, TOSHIFUMI KIMURA, AND NORIHIRO SUZUKI. **Optical properties of CdTe: Experiment and modeling.** *Journal of Applied Physics*, **74**(5):3435–3441, 1993. 45, 46
- [67] SUSUMU NAMBA. **Electro-Optical Effect of Zincblende.** *J. Opt. Soc. Am.*, **51**(1):76–79, Jan 1961. 47

REFERENCES

- [68] T. PFEIFER, T. DEKORSY, W. KTT, AND H. KURZ. **Generation mechanism for coherent LO phonons in surface-space-charge fields of III-V-compounds.** *Applied Physics A: Materials Science and Processing*, **55**:482–488, 1992. 10.1007/BF00348337. 47
- [69] KAZUTAKA G. NAKAMURA, SATOSHI ISHII, SHUSEI ISHITSU, MASATO SHIOKAWA, HIROSHI TAKAHASHI, KURUNTHU DHARMALINGAM, JUN IRISAWA, YOICHIRO HIRONAKA, KUNIE ISHIOKA, AND MASAHIRO KITAJIMA. **Femtosecond time-resolved x-ray diffraction from optical coherent phonons in CdTe(111) crystal.** *Applied Physics Letters*, **93**(6):061905, 2008. 47
- [70] W FISCHLER, R BRATSCHITSCH, R A HPFEL, G ZANDLER, G STRASSER, AND K UNTERRAINER. **The lower branch of plasmon-phonon coupled modes.** *Semiconductor Science and Technology*, **15**(8):813, 2000. 48
- [71] P. LANGOT, R. TOMMASI, AND F. VALLÉE. **Nonequilibrium hole relaxation dynamics in an intrinsic semiconductor.** *Phys. Rev. B*, **54**:1775–1784, Jul 1996. 52, 53
- [72] LAI TIAN-SHU TENG LI-HUA, WANG XIA. **Competition between band filling effect and band-gap renormalization effect in GaAs.** *Acta Physica Sinica*, **60**(4):47201, 2011. 52
- [73] J.-F. LAMI, P. GILLIOT, AND C. HIRLIMANN. **Observation of Interband Two-Photon Absorption Saturation in CdS.** *Phys. Rev. Lett.*, **77**:1632–1635, Aug 1996. 55, 57
- [74] R. COHEN, V. LYAHOVITSKAYA, E. POLES, A. LIU, AND Y. ROSENWAKS. **Unusually low surface recombination and long bulk lifetime in n-CdTe single crystals.** *Applied Physics Letters*, **73**(10):1400–1402, 1998. 55
- [75] ALBERT HAUG. **Carrier density dependence of Auger recombination.** *Solid-State Electronics*, **21**(11 - 12):1281 – 1284, 1978. 56
- [76] V. CHAZAPIS, H. A. BLOM, K. L. VODOPYANOV, A. G. NORMAN, AND C. C. PHILLIPS. **Midinfrared picosecond spectroscopy studies of Auger recombination in InSb.** *Phys. Rev. B*, **52**:2516–2521, Jul 1995. 56
- [77] F. S. KRASNIQI, S. L. JOHNSON, P. BEAUD, M. KAISER, D. GROLIMUND, AND G. INGOLD. **Influence of lattice heating time on femtosecond laser-**

- induced strain waves in InSb.** *Phys. Rev. B*, **78**:174302, Nov 2008. 56, 67, 69
- [78] J.-F. LAMI AND C. HIRLIMANN. **Two-photon excited room-temperature luminescence of CdS in the femtosecond regime.** *Phys. Rev. B*, **60**:4763–4770, Aug 1999. 57
- [79] R. SCHROEDER AND B. ULLRICH. **Absorption and subsequent emission saturation of two-photon excited materials: theory and experiment.** *Opt. Lett.*, **27**(15):1285–1287, Aug 2002. 57, 59, 60
- [80] M. BOMBECK, A. S. SALASYUK, B. A. GLAVIN, A. V. SCHERBAKOV, C. BRÜGGEMANN, D. R. YAKOVLEV, V. F. SAPEGA, X. LIU, J. K. FURDYNA, A. V. AKIMOV, AND M. BAYER. **Excitation of spin waves in ferromagnetic (Ga,Mn)As layers by picosecond strain pulses.** *Phys. Rev. B*, **85**:195324, May 2012. 61, 92
- [81] T. L. LINNIK, A. V. SCHERBAKOV, D. R. YAKOVLEV, X. LIU, J. K. FURDYNA, AND M. BAYER. **Theory of magnetization precession induced by a picosecond strain pulse in ferromagnetic semiconductor (Ga,Mn)As.** *Phys. Rev. B*, **84**:214432, Dec 2011. 61, 66
- [82] B. LÜTHI. *Physical Acoustics in the Solid State*. Number Bd. 15 in Springer Series in Solid-State Sciences. Springer, 2007. 61, 65
- [83] BRIAN W. J. MCNEIL AND NEIL R. THOMPSON. **X-ray free-electron lasers.** *Nat Photon*, **4**:814 – 821, 2010/12//print. 62, 63
- [84] T. DIETL, H. OHNO, AND F. MATSUKURA. **Hole-mediated ferromagnetism in tetrahedrally coordinated semiconductors.** *Phys. Rev. B*, **63**:195205, Apr 2001. 65
- [85] W. LIMMER, J. DAEUBLER, L. DREHER, M. GLUNK, W. SCHOCH, S. SCHWAIGER, AND R. SAUER. **Advanced resistivity model for arbitrary magnetization orientation applied to a series of compressive- to tensile-strained (Ga,Mn)As layers.** *Phys. Rev. B*, **77**:205210, May 2008. 65
- [86] M. GLUNK, J. DAEUBLER, L. DREHER, S. SCHWAIGER, W. SCHOCH, R. SAUER, W. LIMMER, A. BRANDLMAIER, S. T. B. GOENNENWEIN, C. BIHLER, AND M. S. BRANDT. **Magnetic anisotropy in (Ga,Mn)As: Influence**

REFERENCES

- of epitaxial strain and hole concentration. *Phys. Rev. B*, **79**:195206, May 2009. 65
- [87] H. STERN. **Thermal conductivity at the magnetic transition.** *Journal of Physics and Chemistry of Solids*, **26**(1):153 – 161, 1965. 65
- [88] T.L. GILBERT. **A phenomenological theory of damping in ferromagnetic materials.** *Magnetics, IEEE Transactions on*, **40**(6):3443 – 3449, nov. 2004. 66
- [89] SHUFENG ZHANG AND STEVEN S.-L. ZHANG. **Generalization of the Landau-Lifshitz-Gilbert Equation for Conducting Ferromagnets.** *Phys. Rev. Lett.*, **102**:086601, Feb 2009. 66
- [90] C. THOMSEN, H. T. GRAHN, H. J. MARIS, AND J. TAUC. **Surface generation and detection of phonons by picosecond light pulses.** *Phys. Rev. B*, **34**:4129–4138, Sep 1986. 66, 67
- [91] A. H. CHIN, R. W. SCHOENLEIN, T. E. GLOVER, P. BALLING, W. P. LEE-MANS, AND C. V. SHANK. **Ultrafast Structural Dynamics in InSb Probed by Time-Resolved X-Ray Diffraction.** *Phys. Rev. Lett.*, **83**:336–339, Jul 1999. 69
- [92] JERZY GRONKOWSKI. **Propagation of X-rays in distorted crystals under dynamical diffraction.** *Physics Reports*, **206**(1):1 – 41, 1991. 69
- [93] MDC VACUUM LTD. **Flanges and Fittings: Large-Flange ISO LF - NW250**, 2011. 75
- [94] MATERION CORPORATION. **Materion Electrofusion Beryllium Window Thickness Guidelines**, 2011. 75
- [95] ALI ABBOUD, SEBASTIAN SEND, ROBERT HARTMANN, LOTHAR STRDER, ALAN SAVAN, ALFRED LUDWIG, NIKOLAY ZOTOV, AND ULLRICH PIETSCH. **Applications of an energy-dispersive pnCCD for X-ray reflectivity: Investigation of interdiffusion in FePt multilayers.** *physica status solidi (a)*, **208**(11):2601–2607, 2011. 75
- [96] FRANK HOFFMANN. *Magnetic anisotropies of (Ga,Mn)As films and nanostructures.* PhD thesis, University Regensburg, 2010. 79

-
- [97] H.-Y. HAO AND H. J. MARIS. **Dispersion of the long-wavelength phonons in Ge, Si, GaAs, quartz, and sapphire.** *Phys. Rev. B*, **63**:224301, May 2001. 79
- [98] R. ZHOU, B. Q. SUN, X. Z. RUAN, H. H. LUO, Y. JI, W. Z. WANG, F. ZHANG, AND J. H. ZHAO. **Temperature dependence of effective g factor in diluted magnetic semiconductor (Ga,Mn)As.** *Journal of Applied Physics*, **103**(5):053901, 2008. 84, 90, 92
- [99] V. NOVÁK, K. OLEJNÍK, J. WUNDERLICH, M. ČUKR, K. VÝBORNÝ, A. W. RUSHFORTH, K. W. EDMONDS, R. P. CAMPION, B. L. GALLAGHER, JAIRO SINOVA, AND T. JUNGWIRTH. **Curie Point Singularity in the Temperature Derivative of Resistivity in (Ga,Mn)As.** *Phys. Rev. Lett.*, **101**:077201, Aug 2008. 86
- [100] F. V. KYRYCHENKO AND C. A. ULLRICH. **Temperature-dependent resistivity of ferromagnetic $\text{Ga}_{1-x}\text{Mn}_x\text{As}$: Interplay between impurity scattering and many-body effects.** *Phys. Rev. B*, **80**:205202, Nov 2009. 86
- [101] T. JUNGWIRTH, JAIRO SINOVA, A. H. MACDONALD, B. L. GALLAGHER, V. NOVÁK, K. W. EDMONDS, A. W. RUSHFORTH, R. P. CAMPION, C. T. FOXON, L. EAVES, E. OLEJNÍK, J. MAŠEK, S.-R. ERIC YANG, J. WUNDERLICH, C. GOULD, L. W. MOLENKAMP, T. DIETL, AND H. OHNO. **Character of states near the Fermi level in (Ga,Mn)As: Impurity to valence band crossover.** *Phys. Rev. B*, **76**:125206, Sep 2007. 88
- [102] K. C. KU, S. J. POTASHNIK, R. F. WANG, S. H. CHUN, P. SCHIFFER, N. SAMARTH, M. J. SEONG, A. MASCARENHAS, E. JOHNSTON-HALPERIN, R. C. MYERS, A. C. GOSSARD, AND D. D. AWSCHALOM. **Highly enhanced Curie temperature in low-temperature annealed [Ga,Mn]As epilayers.** *Applied Physics Letters*, **82**(14):2302–2304, 2003. 89
- [103] A. H. MACDONALD AND N. SCHIFFER, P. AND SAMARTH. **Ferromagnetic semiconductors: moving beyond (Ga,Mn)As.** *Nat Mater*, **4**:195–202, 2005. 89
- [104] J M WESSELINOWA. **Effects of magnetic ordering on the phonon damping in ferromagnetic semiconductors.** *Journal of Physics: Condensed Matter*, **3**(27):5231, 1991. 90, 92

REFERENCES

- [105] J. ALS-NIELSEN AND D. MCMORROW. *Elements of Modern X-Ray Physics*. John Wiley, 2011. 96, 97, 98, 100
- [106] J.J. SAKURAI AND S.F. TUAN. *Modern Quantum Mechanics*. Addison-Wesley Publishing Company, 1994. 99
- [107] S. MANNINEN. **Resonant raman scattering and fluorescence spectroscopy**. *Radiation Physics and Chemistry*, **50**(1):77 – 89, 1997. 101